Master's thesis

Development of a range counter for nuclide identification in hypernuclear triple coincidence experiments

ハイパー核三重同時測定実験のための

核種同定用飛程検出器の開発

Fumiya OURA
大浦 文也

Department of Physics
Graduate School of Science
Tohoku University

2022

Abstract of master's thesis 2022

Development of a range counter for nuclide identification in hypernuclear triple coincidence experiments

Department of Physics, Graduate School of Science, Tohoku University
Fumiya OURA

1. Introduction

We still have a lot of problems to solve even in the simplest few-body systems of hypernuclei such as ${}^{3}_{\Lambda}$H, ${}^{4}_{\Lambda}$He, and ${}^{4}_{\Lambda}$H.

Measurements to date revealed the existence of a large effect of charge symmetry breaking (CSB) in the four-body system of ${}^{4}_{\Lambda}$He and ${}^{4}_{\Lambda}$H. Our group measured the gamma-ray of the ${}^{4}_{\Lambda}\mathrm{He}(1^{+} \to 0^{+})$ transition with good statistics and high resolution[1]. In contrast, the data of ${}^{4}_{\Lambda}$H measured in the 1970s and 1990s are poor in statistics and resolution. Thus, we plan to precisely measure the gamma-ray energy of the ${}^{4}_{\Lambda}\mathrm{H}(1^{+} \to 0^{+})$ transition using a high-resolution Ge detector array, Hyperball-J (J-PARC E63 experiment). Any theoretical calculation cannot reproduce the large CSB effect. The mechanism is still unclear and the next measurement will provide a clue to a deeper understanding of the origin of the CSB which might be related with ΛN-ΣN coupling interaction.

Excited states of ${}^{3}_{\Lambda}$H are probably unbound, but there is a possibility to observe gamma-rays from them. The energy of the ${}^{3}_{\Lambda}$H excited states with spin (isospin) of $1/2^{+}(\mathrm{T}=1)$ and $3/2^{+}(\mathrm{T}=0)$ can be close to their particle emission thresholds. In such cases, these states are expected to deexcite partly with gamma emission. The gamma-rays give us helpful information on the ${}^{3}_{\Lambda}\mathrm{H}(\mathrm{T}=1)$ and nnΛ states and consequently the ΛNN (T=1) three-body force as well as the ΛN-ΣN coupling interaction.

With these motivations in mind, we plan to measure the gamma-rays from these lightest hypernuclei of ${}^{3}_{\Lambda}$H and ${}^{4}_{\Lambda}$H in the E63 experiment to be performed at the J-PARC K1.1 beamline.

2. J-PARC E63

We cannot produce ${}^{4}_{\Lambda}$H and ${}^{3}_{\Lambda}$H directly from the (K^{-}, π^{-}) and (π^{+}, K^{+}) reactions, and therefore, we adopt the ${}^{7}\mathrm{Li}\,(K^{-}, \pi^{-})$ reaction for the production of ${}^{4}_{\Lambda}$H and ${}^{3}_{\Lambda}$H as hyperfragments. The beam K^{-} and scattered π^{-} are identified and momentum-measured by the K1.1 spectrometer and the SKS spectrometer, respectively. The gamma-ray from ${}^{4}_{\Lambda}$H or ${}^{3}_{\Lambda}$H are measured by a germanium (Ge) detector array, Hyperball-J, installed around the target, which can be operated under high-intensity high-energy hadron beam conditions.

3. Triple Coincidence Method using Range Counters and Position Detectors

The ${}^{7}\mathrm{Li}\,(K^{-}, \pi^{-})$ reaction produces many kinds of hypernuclei including ${}^{4}_{\Lambda}$H and ${}^{3}_{\Lambda}$H. Therefore, it might not be possible to identify the hypernuclear nuclide, from which the gamma-rays are measured by Hyperball-J. For identification of the hypernucleus, we will perform a triple coincidence measurement between the reaction, gamma-ray, and weak decay for the first time (Fig. 1). We measure the kinetic energies of pions from two-body weak decays of hypernuclei ${}^{4}_{\Lambda}$H (53 MeV) and ${}^{3}_{\Lambda}$H (40 MeV) $({}^{4}_{\Lambda}\mathrm{H} \to {}^{4}\mathrm{He} + \pi^{-}, {}^{3}_{\Lambda}\mathrm{H} \to {}^{3}\mathrm{He} + \pi^{-})$ with a range counter system, which is newly developed in the present study.

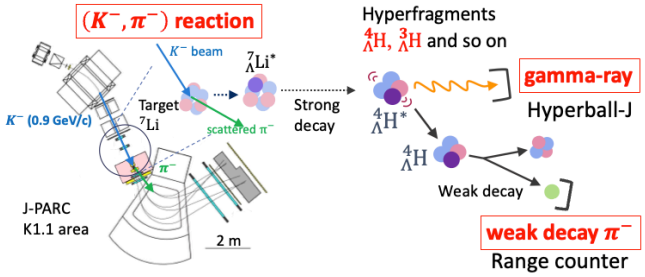

Fig. 1: Principle of the experiment for triple coincidence measurement and the experimental setup.

The range counter system is composed of range counters made of multi-layered plastic scintillator slabs and position detectors of plastic hodoscopes. The purpose of the range counter system is to separate two monochromatic pion peaks in the range spectrum with a kinetic energy resolution less than 3 MeV.

According to the previous study[2], the one-layer thickness of the range counter is optimized by a Monte Carlo simulation taking strong and electromagnetic interactions into account, which shows that ${}^{4}_{\Lambda}$H and ${}^{3}_{\Lambda}$H can be distinguished with a range counter whose each layer is less than 10 mm thick. In this simulation, the hadronic reaction of π^{-} with nuclei incorporated in the simulation could be different from the real interaction, and therefore, we determined the thickness to be 6 mm by taking a safety factor.

The range counter system is made of 24 layers of a 6 mm-thick plastic counter as shown in Fig. 2. We adopted a readout method using wavelength-shifting fibers and SiPMs. In front of the range counter, plastic scintillator

hodoscopes are installed as position detectors for pions, in order to remove angular uncertainty. The range counter system is installed inside the Hyperball-J system.

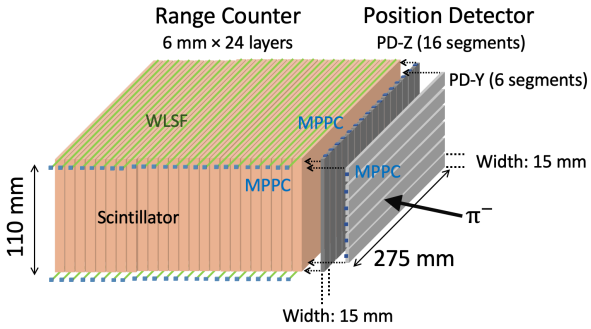

Fig. 2: Range counter system.

4. Test Experiment with Prototype

I fabricated a prototype range counter made of 8 layers of a 6 mm-thick plastic counter. The total thickness of the prototype is one-third of that of the counter for the E63 experiment.

We performed an experiment at the downstream area of the J-PARC K1.8 beam line for the purpose of testing the prototype and evaluating its performance. Negative pions with a momentum of 300 MeV/c were degraded down to less than 110 MeV/c to stop them in the prototype (Fig. 3).

The time of flight was measured using two plastic hodoscopes located just before the prototype. Since the pions had various velocities, the incident energy before the prototype was not uniform.

I selected slow pion events with the information of the time of flight. I confirmed that about 350 pions stopped at the prototype using the information on the energy loss in each layer for each event. Then, I obtained range distributions for two kinetic energy regions around 33 MeV and 20 MeV and found that the two peaks were well separated (Fig. 4). The difference of 33 MeV and 20 MeV (13 MeV) is equal to the difference of kinetic energies of the pions from ${}^{4}_{\Lambda}$H and ${}^{3}_{\Lambda}$H. Therefore, I confirmed that the prototype can separate the pions from ${}^{4}_{\Lambda}$H and ${}^{3}_{\Lambda}$H sufficiently well.

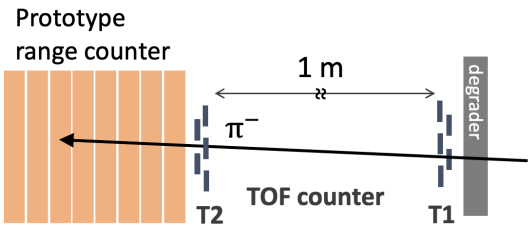

Fig. 3: Experimental setup. Time-of-flight was measured with two counters T1 and T2.

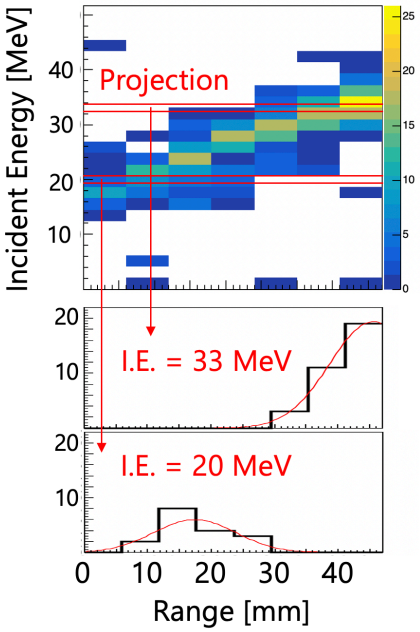

Fig. 4: Top: Correlation between incident energy (I.E.) measured by T1-T2 TOF and the measured range for pion stop events. Bottom: measured range distributions for the incident energy ranges of 33 MeV and 20 MeV.

5. Fabrication and Evaluation of Whole Set of the Range Counter

Results of the test experiment with the prototype confirmed the designed range counter can separate the pions from ${}^{4}_{\Lambda}$H and ${}^{3}_{\Lambda}$H. I fabricated a whole set of the range counter and the position detector for the E63 experiment.

After the fabrication, I tested it with cosmic rays. Thanks to some updates from the fabrication of the prototype, I confirmed that the number of photons detected at SiPMs of the range counter and the position detector were much more than that of the prototype. I also confirmed the detection efficiency of all the layers of the range counter and the segments of the position detectors is higher than 95%.

6. Conclusion

We developed a range counter system for identification of nuclides in a hypernuclear gamma-ray spectroscopy experiment at J-PARC. Based on the results of the experiment with the prototype and of the evaluation of the whole set of the range counter system, we found that the system can identify the weak decay pions in the E63 experiment.

References

[1] T. O. Yamamoto *et al.*, Phys. Rev. Lett., **115** 222501 (2015)
[2] Y. Ishikawa, Master's thesis, Tohoku University (2017)

Contents

Chapter 1

Introduction

The hypernucleus is a many-body system of nucleons and hyperon(s). It has been investigated for studying baryon-baryon interactions and their unique properties caused by hyperons free from the Pauli blocking effect. In particular, the Λ hypernucleus has a much longer lifetime ($\simeq 10^{-10}$ sec) than the time scale of strong interaction ($\simeq 10^{-22}$ sec) and its excited states can be investigated via gamma-ray spectroscopy.

This chapter describes the significance and the purpose of hypernuclear studies, the experimental methods particularly of gamma-ray spectroscopy, and the physics motivations of the future experiment to be performed. Finally, the purpose of this thesis study is described.

1.1 Purpose and Significance of the Study on Hypernucleus

The significance of the study on the hypernucleus is as follows.

Nuclear or Hypernuclear Structures

Hypernuclear studies are interesting from a viewpoint of nuclear structure. Figure 1.1 shows the mass spectrum of ${}^{89}_{\Lambda}$Y [1]. The horizontal axis is the Λ binding energy B_Λ defined as

$$B_\Lambda = M_{core} + M_\Lambda - M_{HYP},$$

where M_{core}, M_Λ, and M_{HYP} represent the mass of the core nucleus, the Λ hyperon,

and the hypernucleus, respectively. Naively, the quantity B_Λ represents "how much lighter the hypernucleus has become after the core nucleus and the Λ are bound".

Since the interaction of ΛN is weaker than that of NN, the spreading width of unbound excited states of Λ hypernuclei is narrower than the Λ's major shell spacing, which allows us to observe the major shell structure of the Λ hyperon in the nuclear potential. This spectrum experimentally confirms the existence of shell structure even in heavy nuclei. This is a good example of how the structure of ordinary nuclei can be studied by using hypernuclei, in which hyperons are free from the Pauli effect and placed inside the nucleus as probes.

Structural changes in hypernuclei due to a hyperon are also interesting. Gamma-ray spectroscopy is one of the best methods to study the properties of nuclei, and it can be also applied to a Λ hypernucleus. Information on the energies and the intensities of gamma-rays makes it possible to study the size and deformation as well as the internal motion of nuclei and hypernuclei. Ge detectors developed by our group enabled high-resolution measurement of energies of gamma-rays from hypernuclei under high-rate and high energy hadron beam conditions. Then, a precise measurement of gamma-rays from ${}^{7}_{\Lambda}$Li was carried out to investigate the structural changes of the nucleus due to the attractive ΛN interaction, and it has been found that the ^{6}Li nucleus shrinks by about 20% due to the Λ hyperon [2].

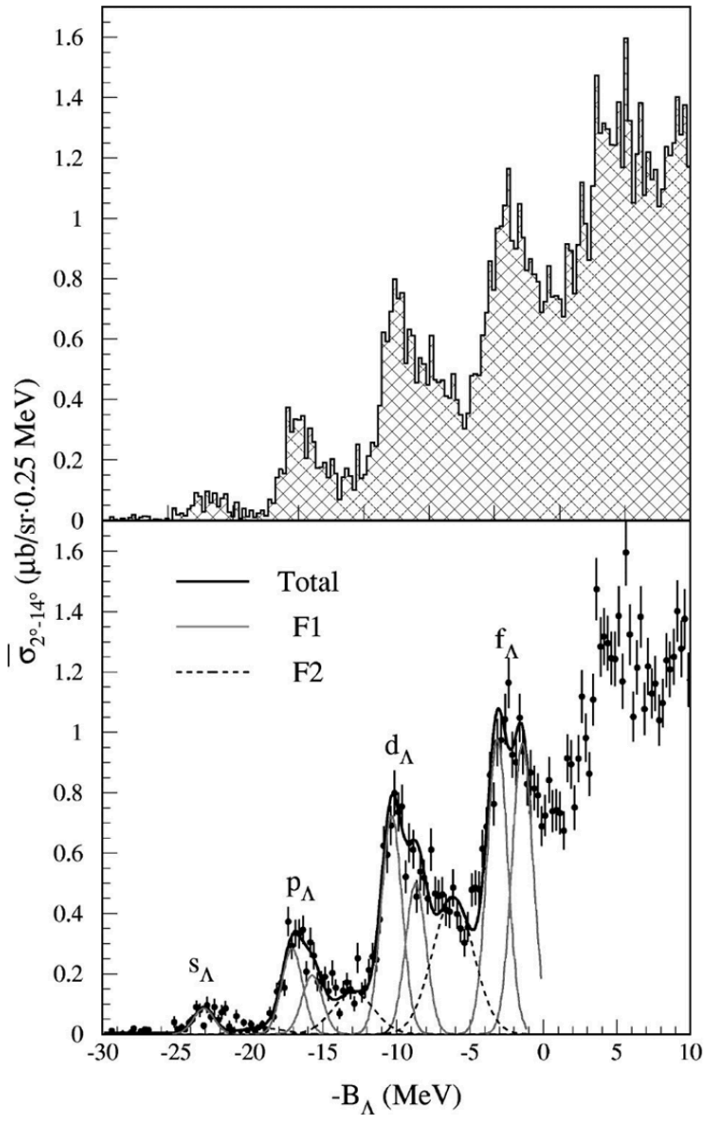

Figure 1.1: Hypernuclear mass spectrum of ${}^{89}_{\Lambda}$Y without/with peak fitting [1].

Hyperon-Nucleon Interaction in Free Space and in Nuclear Medium

Until recently, information on the hyperon-nucleon (YN) interaction was extracted from measurements of the mass or energy levels of hypernuclei. These spectroscopic

studies have been performed using electron beams at JLab and MAMI and using hadron beams at KEK and J-PARC.

However, the YN interaction in a nuclear medium becomes different from that in the free space due to many-body effects in a nucleus. Recently, a Σp scattering experiment was performed with the first great success at J-PARC [3, 4]. The next experiment on Λp scattering has been proposed [5]. These pioneering experiments will make it possible for us to directly determine the YN two-body interactions with high precision.

Under this situation, it becomes more interesting than ever to study the many-body effects in nuclear medium. One of the subjects is $\Lambda N - \Sigma N$ coupling. Though one pion exchange between Λ and N is forbidden because of the isospin invariance of the strong interaction, two-pion exchange is allowed by changing Λ to Σ temporarily as an intermediate state and returning to Λ. This $\Lambda N - \Sigma N$ coupling gives various effects in nuclear matter, but its property and magnitude are not determined at all. The second subject is the three-body interaction. We do not understand well the interaction among three nucleons, and much less the interaction among three baryons including a hyperon. It is suggested that the contribution from ΛNN three-body force might play a key role in a wide range of nuclear systems from light hypernuclei to neutron stars. Now that it is possible to investigate the YN interaction directly from scattering experiments, we can reliably investigate many-body effects extracted from data of hypernuclei.

As described in the following section, we still have a lot of problems to solve even in the simplest few-body systems of hypernuclei such as ${}^{3}_{\Lambda}$H, ${}^{4}_{\Lambda}$He, and ${}^{4}_{\Lambda}$H. The problems in these lightest hypernuclei are most likely due to the lack of understanding of the YN interactions in the free space and the many-body effects in nuclear medium described here. In recent years, new types of calculations such as Lattice QCD, chiral EFT, and ab-initio few-body calculations have emerged. When hyperons are included in nuclear systems, we sometimes meet unexpected problems that were not visible in the ordinary nucleus. This indicates that our theory of baryon-baryon forces is not perfect. The data of few-body hypernuclei are very valuable for verification of new theoretical calculations. Therefore, it is worthwhile to experimentally study light hypernuclei precisely.

Hypernuclei are not just nuclei with an added degree of freedom of strangeness; they are rich objects that change our understanding of the baryon-baryon interactions and give us deeper insights into the properties of baryonic matter that cannot be obtained from ordinary nuclei alone.

1.2 Gamma-ray Spectroscopy of ${}^{4}_{\Lambda}$He (J-PARC E13)

Gamma-ray spectroscopy of Λ hypernuclei has been advanced by the Tohoku University group by the Proton Synchrotron at the High Energy Accelerator Research Organization (KEK) in Tsukuba, Japan (KEK-PS) and the Alternating Gradient Synchrotron in the Brookhaven National Laboratory (BNL) in the United States. Then, the activity moved on to J-PARC in Tokai, Japan, and experiments have been conducted and are currently planned there. A lot of hypernuclei have been investigated by gamma-ray spectroscopy and significant contributions have been made to the understanding of the structure of hypernuclei and the interactions between baryons.

In 2015, our group conducted a precision measurement of the gamma-ray energy of the M1 transition of ${}^{4}_{\Lambda}$He $(1^+ \to 0^+)$ using a high-resolution Ge detector array (Hyperball-J) at J-PARC K1.8 beamline (J-PARC E13).

${}^{4}_{\Lambda}$He hypernuclei were directly produced by the ^{4}He(K^-, π^-) reaction and the energy of the deexcitation gamma-ray was measured with high resolution. As a result, the transition energy of ${}^{4}_{\Lambda}$H $(1^+ \to 0^+)$ was determined to be 1.406 ± 0.003 MeV [6] and the value is much higher than that measured in 1970s. Consequently, the result revealed presence of a large charge symmetry breaking effect in ${}^{4}_{\Lambda}$He and ${}^{4}_{\Lambda}$H as described in the next section.

1.3 Next Hypernuclear Gamma-ray Spectroscopy Experiment (J-PARC E63)

We plan a new experiment of hyerpnuclear gamma-ray spectroscopy (J-PARC E63) employing the K1.1 beam line, K1.1, which is to be newly constructed at J-PARC in near future. In this section, two of the motivations of the experiment are described.

1.3.1 Study on the Charge Symmetry Breaking in the ΛN Interaction

One of the open, crucial problems in the strangeness nuclear physics is charge symmetry breaking (CSB) in the strong interaction between Λ and N. This effect is evident in the four-body hypernuclei of ${}^{4}_{\Lambda}$H and ${}^{4}_{\Lambda}$He. In this section, studies of the CSB are reviewed and the next approach to the problem in the E63 experiment is described.

Charge symmetry and its breaking in many-body-nucleon system

The strong interaction is invariant under replacement of up and down quarks. this symmetry is called charge symmetry. The isospin T = 1/2 doublet of quarks is composed of up ($T_3 = +1/2$) and down ($T_3 = -1/2$) quarks. The charge symmetry, in other words, is the invariance under a rotation by 180° for the x-axis in the isospin space. The symmetry is a special case of charge independence, the invariance under any rotation in the isospin space.

While the charge symmetry in the hadron level is slightly broken as in the mass difference between proton and neutron, the charge symmetry in the nuclear level, namely, the symmetry under replacement between protons and neutrons, holds well in ordinary nuclei (at this moment, ordinary nuclei means nuclei with no strangeness degree of freedom). The symmetry appears in little difference in nuclear binding energies between mirror nuclei ^{3}H and ^{3}He. The difference is 764 keV. About 90% of the difference of 764 keV is explained from the static Coulomb interaction [7, 8, 9], other electromagnetic effects [10], and n, p mass difference in the kinetic energy [11]. The rest of the difference of about 70 keV comes from charge symmetry breaking in strong interaction.

The origin of CSB should be explained from the current mass difference between up and down quarks and the electromagnetic interaction. In the hadron level, the CSB effect, for instance, makes the neutron approximately 0.1% heavier than the proton, and the origin of the CSB is dominantly caused by the mass difference between the quarks, approximately twice more than their electromagnetic repulsion [12].

The origin of the CSB between the ^{3}H and ^{3}He binding energies is attributed to the neutral meson mixing effect. Neutral mesons with the same spin-parity but with different isospins like $\rho^0 - \omega$, $\pi^0 - \eta$, and $\pi^0 - \eta'$ slightly mix because of isospin breaking due to u, d quark mass difference and electromagnetic effects. The effect of the short-range $\rho^0 - \omega$ mixing dominantly contributes to the 70 MeV difference in the nuclear binding energy between ^{3}H and ^{3}He: $\Delta B^3(0^+_{g.s.})$ defined as $\Delta B^3(0^+_{g.s.}) = B[^3\mathrm{He}] - B[^3\mathrm{H}]$, while the others of $\pi^0 - \eta$ and $\pi^0 - \eta'$ make negligible contributions [13].

Charge symmetry breaking in four-body systems of nucleons and a hyperon

Figure 1.2 shows the energy levels of ${}^4_\Lambda$He and ${}^4_\Lambda$H in terms of the Λ binding energy, excluding the difference in binding energies between the core nuclei. As described in

Sect. 1.2, our group precisely measured the gamma-ray energy of the M1 transition of ${}^{4}_{\Lambda}\mathrm{He}\,(1^+ \to 0^+)$. At the same time, the MAMI group successfully performed a decay pion spectroscopy experiment and measured the Λ binding energy of the ${}^{4}_{\Lambda}\mathrm{H}$ ground state [14, 15]. Since the ground state of ${}^{4}_{\Lambda}\mathrm{H}$ decays into two bodies of ${}^{4}\mathrm{He}$ and π^- via weak interaction. It is consequently possible to obtain the Λ binding energy only by measuring the momentum of the π^-, determining the Λ binding energy of the ${}^{4}_{\Lambda}\mathrm{H}$ ground state as $2.157 \pm 0.077\,\mathrm{MeV}$. The Λ binding energy of the 0^+ ground state of ${}^{4}_{\Lambda}\mathrm{He}$ was measured to be $2.39 \pm 0.05\,\mathrm{MeV}$ by an emulsion experiment [16] and, the STAR collaboration has recently reported a value consistent with the emulsion value in a heavy ion experiment [17].

The gamma-ray energy of the transition ${}^{4}_{\Lambda}\mathrm{H}\,(1^+ \to 0^+)$ was measured three times in old experiments [18, 19, 20]. The value in Fig. 1.2 is the averaged value of them.

These measurements revealed the existence of a large CSB effect in the ΛN interaction. The difference in the Λ binding energy between the ground states, $\Delta B^4_\Lambda(0^+_{\mathrm{g.s.}})$, is $233 \pm 92\,\mathrm{keV}$, which is much larger than the difference in the binding energy between the core nuclei of $\Delta B^3(0^+_{g.s.}) = 70\,\mathrm{keV}$. Furthermore, the difference in the Λ binding energy between the 1^+ excited states is $\Delta B^4_\Lambda(1^+_{\mathrm{exc}}) = -83 \pm 94\,\mathrm{keV}$, and the large symmetry breaking in the ground states is recovered in the excited states suggests a large spin dependence of the CSB in ΛN interaction. Here, $\Delta B^4_\Lambda(0^+_{\mathrm{g.s.}})$ and $\Delta B^4_\Lambda(1^+_{\mathrm{exc}})$ are defined as $\Delta B^4_\Lambda(0^+_{\mathrm{g.s.}}) = B_\Lambda[{}^{4}_{\Lambda}\mathrm{He}(0^+)] - B_\Lambda[{}^{4}_{\Lambda}\mathrm{H}(0^+)]$, and $\Delta B^4_\Lambda(1^+_{\mathrm{exc}}) = B_\Lambda[{}^{4}_{\Lambda}\mathrm{He}(1^+)] - B_\Lambda[{}^{4}_{\Lambda}\mathrm{H}(1^+)]$.

In the case of the core nuclei, the binding energy difference mostly comes from Coulomb interaction, but in the case of the Λ binding energy difference in the A = 4 hypernuclei, its contribution is rather small [21]. The $\Delta B^4_\Lambda(0^+_{\mathrm{g.s.}})$ should come from charge symmetry breaking in the strong interaction, suggesting that the Λn interaction is significantly different from the Λp interaction. A Λ hyperon has isospin 0 and consequently, the charge symmetry should hold well between the isospin doublet of Λn ($\mathrm{T}_3 = -1/2$) and Λp ($\mathrm{T}_3 = +1/2$) interactions. However, this is not the reality.

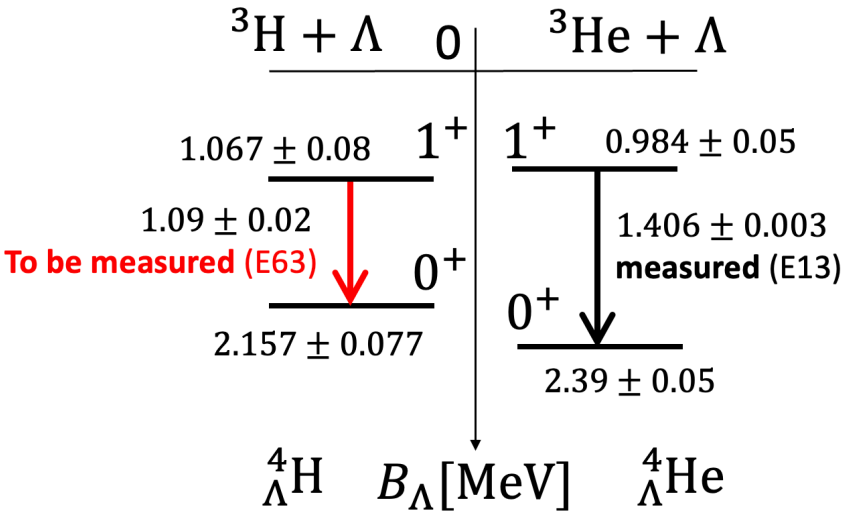

Figure 1.2: Level schemes of γ-ray transitions of $^4_\Lambda$H and $^4_\Lambda$He. The Λ binding energy (B_Λ) of $^4_\Lambda$He (0^+) was measured in emulsion experiments [16] and that of $^4_\Lambda$H (0^+) in decay pion spectroscopy [14, 15].

Theoretical studies on the CSB

Λ hyperons have a small admixture of Σ^0 (T=1 component) due to a small isospin symmetry breaking. Figure 1.3 shows the diagram for the $\Lambda - \Sigma^0$ mixing in ΛN interaction. One-pion exchange between Λ and N is forbidden due to isospin conservation in the first approximation, but because of the mixing, the one-pion exchange is allowed and could contribute to long-range CSB. However, the mixing can not completely explain the observed large effect of CSB in $^4_\Lambda$H and $^4_\Lambda$He. It predicted only $\Delta B^4_\Lambda(0^+_{\rm g.s.}) \simeq 100\,$keV.

Studies with perturbation theory using four-body wave functions from variational Monte Carlo calculation predicted $\Delta B^4_\Lambda(0^+_{\rm g.s.}) \simeq 50\,$keV and $\Delta B^4_\Lambda(1^+_{\rm exc}) \simeq -60\,$keV [23]. On the other hand, ab-initio calculations based on the widely used hyperon-nucleon (YN) Nijmegen soft-core meson exchange model (NSC97e) predicted $\Delta B^4_\Lambda(0^+_{\rm g.s.}) \simeq 70\,$keV and $\Delta B^4_\Lambda(1^+_{\rm exc}) \simeq -10\,$keV [24]. A precise calculation was recently performed based on the chiral EFT interaction (the leading order) with the $\Lambda - \Sigma^0$ mixing effect using a four-body no-core shell model [25]. However, any calculation has not been able to reproduce the large symmetry-breaking effect with satisfaction. It is conjectured that the origin of the CSB is related to ΛN $-$ ΣN coupling and many-body effects like ΛNN three-body interaction (Fig. 1.4) but the

details of the mechanism are still unclear.

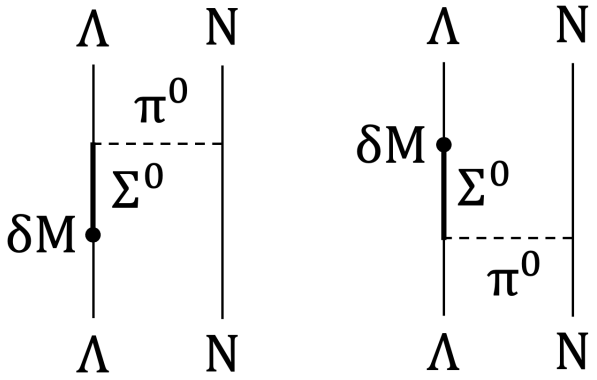

Figure 1.3: CSB contributions involving pion exchange due to $\Lambda\Sigma^0$ mixing [22]

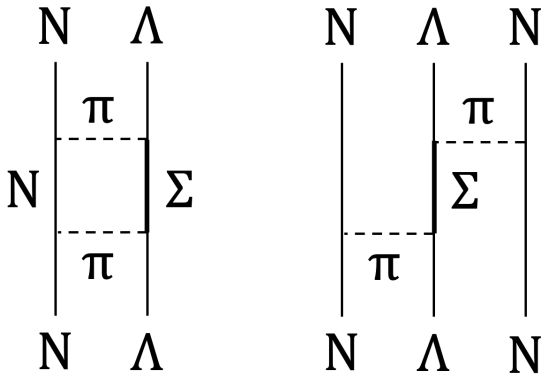

Figure 1.4: Left: ΛN-ΣN coupling between Λ and N. Right: ΛNN three-body interaction due to the ΛN-ΣN coupling

Future measurement of the gamma-ray energy of ${}^{4}_{\Lambda}\mathrm{H}\,(1^+ \to 0^+)$

As mentioned before, the gamma-ray transition of ${}^{4}_{\Lambda}\mathrm{H}\,(1^+ \to 0^+)$ was measured three times in the past. It was measured (1) via stopped K^- on ^{6}Li and ^{7}Li in coincidence with pions with 48-58 MeV of kinetic energy [18], (2) via stopped K^- on ^{7}Li in coincidence with charged one or two particles [19], and (3) via stopped K^- on Li, Be, and C targets coincidently with 53 MeV π^- [20]. The value of 1.09±0.02 MeV in Fig. 1.2 is the averaged value of (1) 1.04 ± 0.04 MeV, (2) 1.09 ± 0.03 MeV, and

(3) $1.114 \pm 0.015 \pm 0.015$ MeV. These three values measured with NaI in the 1970s and 1990s rather diverge from each other, and all the data are poor in statistics and resolution.

Therefore, the E63 experiment plans to measure this energy with an accuracy of several keV, as in the E13 experiment. Although no theory has yet been able to reproduce the magnitude of this CSB effect, ab-initio rigorous calculations of few-body hypernuclei and updated theoretical models of baryon-baryon interactions are being developed at present. Therefore, it is essential to provide high-precision data from the experimental side. Our motivation is to elucidate the origin of the CSB mechanism and contribute to understanding of the baryon-baryon interactions by combining precise measurements of the four-body hypernuclear energies with precise theoretical calculations. The Λp interaction is planned to be studied via a scattering experiment being prepared now. In contrast, the Λn interaction is hard to study directly via scattering experiments. Then, it is significant to study the CSB by precise measurement of the hypernuclear energy levels.

1.3.2 Search for Excited States of ${}^{3}_{\Lambda}$H

Few-body hypernuclear systems are not yet completely understood besides the problem of CSB. In the two-body nucleon system, only deuteron belonging to the isospin singlet (T = 0) is bound, and any two-body nucleon system belonging to the isospin triplet (T = 1) is not bound.

When considering the three-body system with a Λ, only the ground-state hypertriton ${}^{3}_{\Lambda}$H with T = 0 and spin-parity $1/2^{+}$ is considered to be bound. However, the HypHI experiment conducted at the Heavy Ion Institute (GSI) suggested existence of one of the T = 1 three-body systems, nnΛ [26] as a bound state, although it was not predicted to be bound by any calculation [27, 28, 29]. Motivated by this experiment, an experiment to search for the nnΛ state [30] and the final state interaction of nΛ [31] was performed at Thomas Jefferson National Accelerator Facility (JLab) in the United States. The experiment did not find a statistically significant signal for the Λnn state, but the statistics is insufficient to conclude whether the nnΛ state exists. A plan for the next search experiment with increased accuracy is under discussion.

The ground state binding energy of ${}^{3}_{\Lambda}$H was measured using nuclear emulsion plates in the 1970s, and its value was reported to be $B_{\Lambda}({}^{3}_{\Lambda}\mathrm{H}) = 0.13 \pm 0.05$ MeV [16]. Because this value is small, it was naturally believed that ${}^{3}_{\Lambda}$H is a very loosely bound state of a Λ and a deuteron. Therefore, the lifetime of ${}^{3}_{\Lambda}$H was considered to be almost the same as the lifetime of Λ in the free space, and the old emulsion data

with large errors were not inconsistent with this native expectation [33, 34, 35].

Recently, however, heavy ion experiments reported lifetime values inconsistent with that of Λ in the free space (Table 1.1) [36, 37, 38, 39]. They claimed that the lifetime of ${}^{3}_{\Lambda}\mathrm{H}$ is significantly shorter than that of Λ in the free space.

Table 1.1: Lifetime of ${}^{3}_{\Lambda}\mathrm{H}$.

	Lifetime of ${}^{3}_{\Lambda}\mathrm{H}$ [ps]
emulsion [33]	232^{+45}_{-34}
emulsion [34]	285^{+127}_{-105}
emulsion [35]	246^{+62}_{-41}
STAR [36]	157 ± 30
HypHI [37]	$183^{+42}_{-32} \pm 37$
ALICE [38]	$181^{+54}_{-39} \pm 33$
STAR [39]	$142^{+24}_{-21} \pm 29$
Λ in free space [PDG]	263.2 ± 2.0

In addition, the STAR group recently reported that the Λ binding energy of ${}^{3}_{\Lambda}\mathrm{H}$ ($0.41 \pm 0.12(\mathrm{stat.}) \pm 0.11(\mathrm{syst.})$ MeV) [40] is much larger than that obtained by nuclear emulsion experiments.

Thus, the situation is problematic because various lifetime values seem to be significantly inconsistent with the Λ binding energies and, in addition, various experimental values do not agree with each other. This fact suggests that our understanding is still insufficient even for the simplest hypernucleus, ${}^{3}_{\Lambda}\mathrm{H}$.

A possible solution to these two issues may be given by a measurement of the excited state energies of ${}^{3}_{\Lambda}\mathrm{H}$. Although the excited states of ${}^{3}_{\Lambda}\mathrm{H}$ are believed to be unbound, they may emit de-excited gamma-rays (Fig. 1.5). According to Ref. [26], the nnΛ state is possibly bound. Then, from the charge independence, the energy of the $1/2^{+}$ (T=1) state of ${}^{3}_{\Lambda}\mathrm{H}$ may be below or very close to the threshold of $(\mathrm{np})_{\mathrm{T}=1}\Lambda$. In such a case, since the isospin is conserved in strong interaction, the decay of ${}^{3}_{\Lambda}\mathrm{H}\,(\mathrm{T}=1) \to \mathrm{d}\Lambda$ via the strong interaction is suppressed, and $(1/2^{+}\,(\mathrm{T}=1) \to 3/2^{+}\,(\mathrm{T}=0))$ and/or $(1/2^{+}\,(\mathrm{T}=1) \to 1/2^{+}\,(\mathrm{T}=0))$ gamma transitions could be observed.

If these gamma-rays are precisely measured, we can obtain information on the excited states of ${}^{3}_{\Lambda}\mathrm{H}$ (T = 1) and, at the same time, confirm that the nnΛ state can exist either as a bound state or a resonance state. Although theoretical predictions claim that the nnΛ state is not bound with much higher energy than the threshold, it could be bound by an effect of the three-body interaction (especially of T = 1).

If we measure the energy of pnΛ (T = 1), we can obtain important information about the T = 1 three-body interaction, which is especially important in neutron stars where many neutrons exist. On the other hand, it is possible that the excited state energy of $3/2^+$ (T = 0) is lower than or very close to the threshold of dΛ. In this case, a gamma-ray of $3/2^+$ (T = 0) → $1/2^+$ (T = 0) transition will be observed. This measurement will reveal the magnitude of the ΣN − ΛN coupling. We plan to measure the energies of these gamma transitions using Hyperball-J.

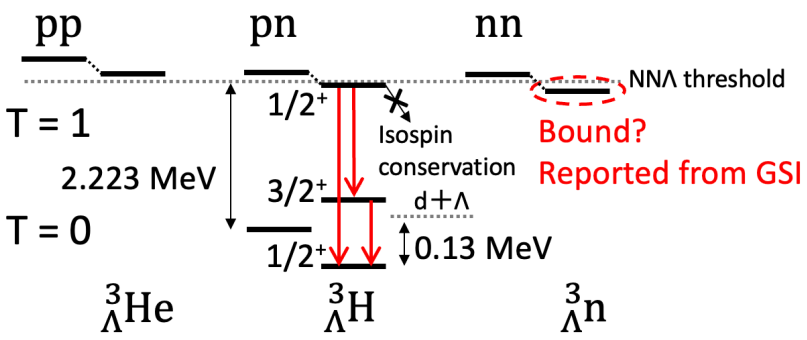

Figure 1.5: Energy levels of the three-body system of Λ and nucleons and observable gamma transitions of ${}^{3}_{\Lambda}$H.

1.4 Purpose of this Study

The E63 experiment uses ^{7}Li (K^-, π^-) reaction. ${}^{4}_{\Lambda}$H and ${}^{3}_{\Lambda}$H are produced when unbound, highly excited states of ${}^{7}_{\Lambda}$Li are produced and decay via strong interaction with emission of ^{3}He or ^{4}He, respectively. Hypernuclei such as ${}^{4}_{\Lambda}$H and ${}^{3}_{\Lambda}$H which are produced after the decay of the unbound excited states hypernuclei directly generated from the (K^-, π^-) or (π^+, K^+) reactions are called secondary hypernuclei or hyperfragments. To measure the energy of gamma-rays from ${}^{4}_{\Lambda}$H and ${}^{3}_{\Lambda}$H, it is necessary to identify the nuclides of secondary hypernuclei produced after the (K^-, π^-) reaction. In this study, we developed a detector system for identifying the nuclides.

Chapter 2

J-PARC E63 Experiment

We plan to measure gamma-rays from ${}^{4}_{\Lambda}$H and ${}^{3}_{\Lambda}$H. One of the purposes is a precision measurement of the energy difference between the ground doublet states in the ${}^{4}_{\Lambda}$H for study of the origin of charge symmetry breaking in the four-body baryon system. The other purpose is to search for excited states of ${}^{3}_{\Lambda}$H. This chapter describes outline of the E63 experiment and the gamma-ray measurement method.

2.1 Experimental Methods

2.1.1 Production of Hypernuclei and Measurement of Gamma-rays

We use ^{7}Li target for production of ${}^{4}_{\Lambda}$H and ${}^{3}_{\Lambda}$H. Here I explain the reason for using the target and the way of producing ${}^{4}_{\Lambda}$H and ${}^{3}_{\Lambda}$H. Reactions commonly used to create a Λ hyperon are $K^{-}\mathrm{n} \to \pi^{-}\Lambda$ and $\pi^{+}\mathrm{n} \to \mathrm{K}^{+}\Lambda$, where a neutron is converted to a Λ hyperon. However, ^{4}H decays in a half-life of 1.4×10^{-22} seconds. Although ^{3}H has a relatively long half-life of 12 years, it is not easy to prepare much of ^{3}H. Thus, it is hard to produce ${}^{4}_{\Lambda}$H or ${}^{3}_{\Lambda}$H directly from the reactions of (K^{-}, π^{-}) or (π^{+}, K^{+}). Alternatively, there are (e, $e'K^{+}$), (π^{-}, K^{0}), and (K^{-}, π^{0}) reactions that change a proton to a Λ. Since both ^{4}He and ^{3}He are stable nuclei, direct production is possible in these reactions. However, it is not easy to produce ${}^{4}_{\Lambda}$H or ${}^{3}_{\Lambda}$H from these reactions; in the (e, $e'K^{+}$) reaction, the background is extremely high because a primary beam is used, which makes it impossible to measure gamma-rays coincidently. In the (π^{-}, K^{0}) and (K^{-}, π^{0}) reactions, the detection efficiency is low because of the necessity to measure neutral particles of K^{0} and π^{0}, which leads to a low production yield.

We adopt $^{7}\mathrm{Li}\,(K^{-}, \pi^{-})$ reaction for the production of ${}^{4}_{\Lambda}$H or ${}^{3}_{\Lambda}$H, where these

hypernuclei are expected to be produced efficiently. In the $^{7}\mathrm{Li}\,(K^{-},\,\pi^{-})$ reaction, various excited states of $^{7}_{\Lambda}\mathrm{Li}$ are produced, and if they have relatively high energy, they decay into two or more nuclear fragments including hypernuclei (called hyperfragments) depending on the energy the $^{7}_{\Lambda}\mathrm{Li}$ excited state has.

The energy levels and decay channels of $^{7}_{\Lambda}\mathrm{Li}$ are shown in Fig. 2.1. Highly-excited unbound states of $^{7}_{\Lambda}\mathrm{Li}$ decay via strong interaction into various hyperfragments. In the region of excitation energy higher than 19.3 MeV, $^{4}_{\Lambda}\mathrm{H}$ can be produced, and in that higher than 6.9 MeV, $^{3}_{\Lambda}\mathrm{H}$ can. In the experiment, the missing mass of $^{7}_{\Lambda}\mathrm{Li}^{*}$ is measured, and the production of $^{4}_{\Lambda}\mathrm{H}$ or $^{3}_{\Lambda}\mathrm{H}$ can be enhanced by selecting the appropriate regions of the missing mass. The missing mass is obtained from the momentum of beam K^{-} and scattered π^{-} as;

$$\mathrm{M_{HYP}} = \sqrt{(\mathrm{E}_{\pi} + \mathrm{M} - \mathrm{E_K})^2 - (\overrightarrow{P_{\pi}} - \overrightarrow{P_K})^2},$$

where the E_{π} ($\mathrm{E_K}$) is the total energy of π^{-} (K^{-}), $\overrightarrow{P_{\pi}}$ ($\overrightarrow{P_K}$) is the momentum of π^{-} (K^{-}), and M is the mass of the target nucleus.

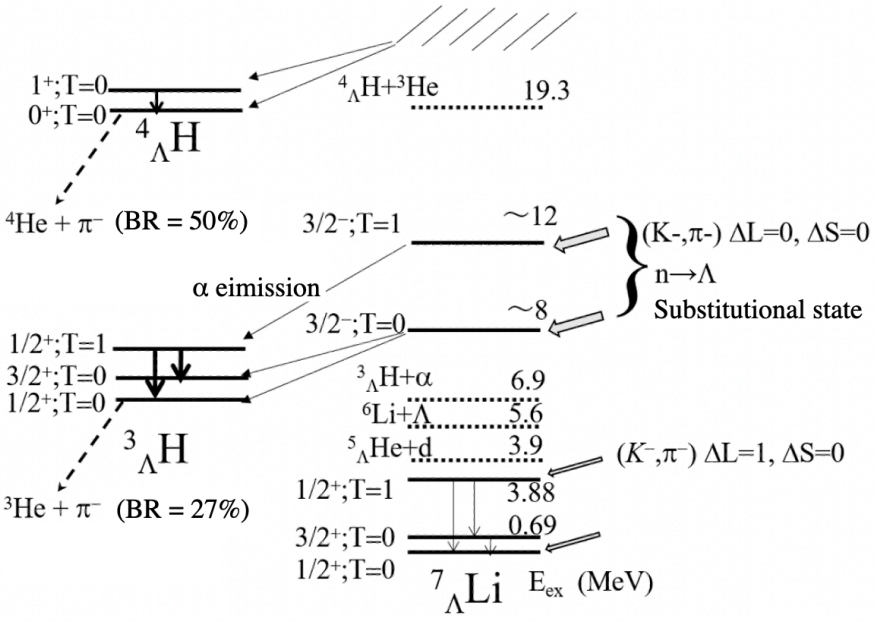

Figure 2.1: The energy levels and decay channels [46]

Production of $^{4}_{\Lambda}\mathrm{H}$

We produce $^{4}_{\Lambda}\mathrm{H}$ from the in-flight $^{7}\mathrm{Li}\,(K^{-},\,\pi^{-})$ reaction at 0.9 GeV/c. The gamma-ray was observed in an experiment at the Alternating Gradient Synchrotron in Brookhaven National Laboratory (BNL-AGS) in the past [41]. This experiment was

conducted to measure the gamma-ray transition of ${}^{7}_{\Lambda}$Li via the (K^-, π^-) reaction at $P_{K^-} = 0.82\,\mathrm{GeV/c}$ with 10^{10} kaons on Li target. Fig. 2.2 shows gamma-ray energy spectra observed in coincidence with the (K^-, π^-) reaction. This figure is shown separately in three excitation-energy regions of ${}^{7}_{\Lambda}$Li; (a) -2 to 6 MeV (b) 6 to 22 MeV, and (c) 22 to 39 MeV. In (c), we can see a peak at 1.1 MeV, and the peak was believed to be the gamma-ray from both ${}^{4}_{\Lambda}$H and ${}^{4}_{\Lambda}$He at that time. However, the E13 experiment recently determined the gamma-ray energy of ${}^{4}_{\Lambda}$He to be 1.406 MeV. Therefore, the peak at 1.1 MeV is considered to be only from ${}^{4}_{\Lambda}$H. It shows that a large yield of gamma-rays from excited ${}^{4}_{\Lambda}$H is expected in this reaction. Therefore, we decided to adopt this reaction.

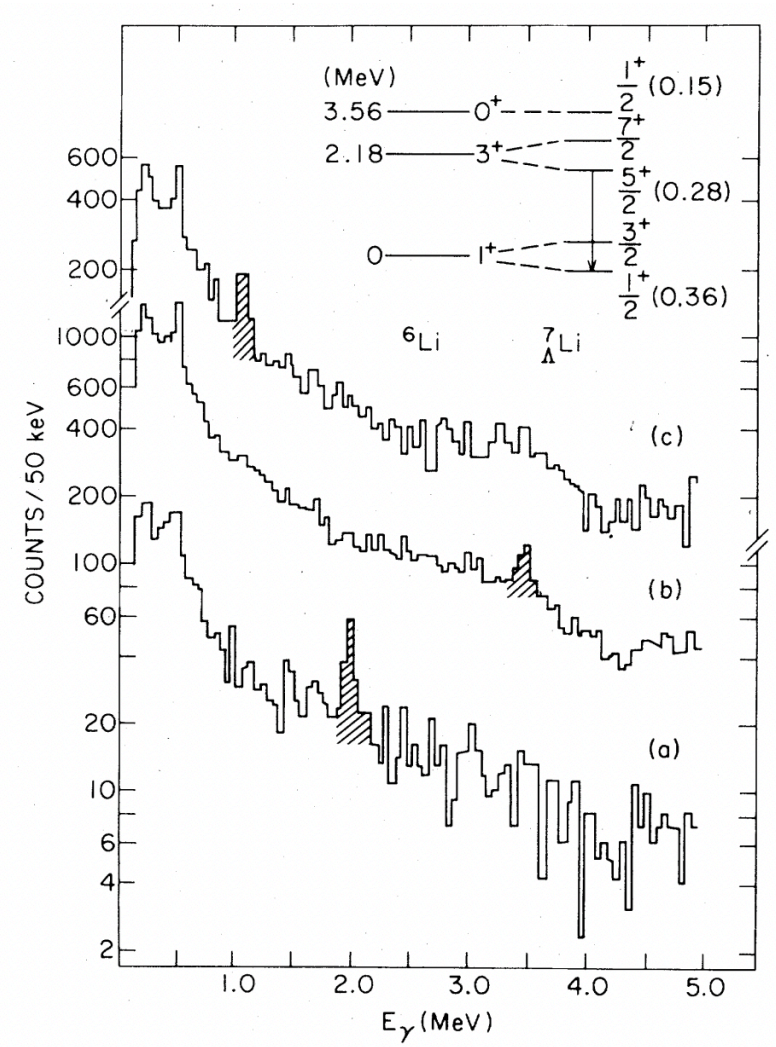

Figure 2.2: Gamma-ray energy spectra observed in coincidence with the (K^-, π^-) reaction [41]. This figure is shown separately in three excitation-energy regions of ${}^{7}_{\Lambda}$Li; (a) -2 to 6 MeV (b) 6 to 22 MeV, and (c) 22 to 39 MeV.

Production of ${}^{3}_{\Lambda}$H

In the ^{7}Li nucleus, there is a cluster structure of ^{3}H and ^{4}He. Therefore, ${}^{3}_{\Lambda}$H is likely to be produced when the ^{3}H cluster in ^{7}Li target is converted by the ^{7}Li(K$^-$, π^-) reaction. As Fig. 2.1 shows, the ${}^{3}_{\Lambda}$H production threshold is about 8 MeV in the ${}^{7}_{\Lambda}$Li excitation energy. In the (K^-, π^-) reaction with a beam K^- around 1.0 GeV/c,

substitutional state production is favored and produced states are likely to decay into ${}^{3}_{\Lambda}\mathrm{H}$.

When the excitation energy of ${}^{7}_{\Lambda}\mathrm{Li}$ is over 12 MeV, the excited state with T = 1 can be produced and it is likely to decay into the excited state of ${}^{3}_{\Lambda}\mathrm{H}$ with isospin T = 1 and spin-parity $1/2^{+}$ due to isospin conservation. When in the region of the excited energy from 8 to 12 MeV, the exited ${}^{7}_{\Lambda}\mathrm{Li}$ state has $3/2^{-}$ of spin-parity and T = 0 isospin. The state is likely to decay into either two states of ${}^{3}_{\Lambda}\mathrm{H}$ with $3/2^{+}$, T = 0 or $1/2^{+}$, T = 0.

2.2 Experimental Setup

2.2.1 J-PARC K1.1 Beamline

Japan Proton Accelerator Research Complex (J-PARC) is a group of proton accelerators and experimental facilities for conducting cutting-edge research in a wide range of fields, from elementary particle physics to nuclear physics, material science, life science, and nuclear transmutation. J-PARC's proton accelerator group accelerates protons to 400 MeV with a linac, 3 GeV with a synchrotron called Rapid Cycling Synchrotron (RCS), and 30 GeV with another synchrotron called Main Ring (MR).

At the Hadron Experimental Facility (Fig. 2.3), primary protons extracted from the MR and the secondary particles generated by bombarding the primary protons to a gold target (T1 target) are used. The primary beam is extracted slowly so that many particles are produced continuously at the T1 target, which enables a high-intensity beam in experimental areas. It takes about 2 sec to slowly extract protons little by little. This method is called slow extraction. Primary protons and secondary particles are transported to the experimental areas such as K1.8, K1.8BR, KL, and high-p beamline. In the facility, many experiments have been ever carried out from elementary particles to hadron and nuclear physics.

The K1.1 is a new beamline that is to be constructed at the J-PARC Hadron Experimental Facility (Fig. 2.4). It is possible to use secondary particles such as K mesons and π mesons as high-purity beams. In using K^{-} as beam, the beam K^{-} are mixed with background π^{-} due to the decay of K^{0} or K^{-}. In order to remove these π^{-} and increase the purity of K^{-}, an intermediate focal slit (IF) is installed immediately after the D2 magnet. The magnets upstream of the IF compose an optical system that focuses the secondary particles from the T1 target to the IF, and the impurity π^{-} is removed from the beam. After the IF slit,

two-stage electrostatic separators (ESS1 and ESS2) are installed, which separate particles by their velocities with a high electric field and a perpendicular magnetic field applied. A maximum of ±350 kV voltage is applied between the electrodes. The upstream part of the beamline has already been successfully operated from the T1 target to the D3 magnet including ESS1. The ESS2 will be installed after the D3 magnet. These systems allow the use of high-purity K^- beams up to the maximum momentum 1.1 GeV/c, where the cross section of the spin-flip state of Λ hypernuclei is maximized.

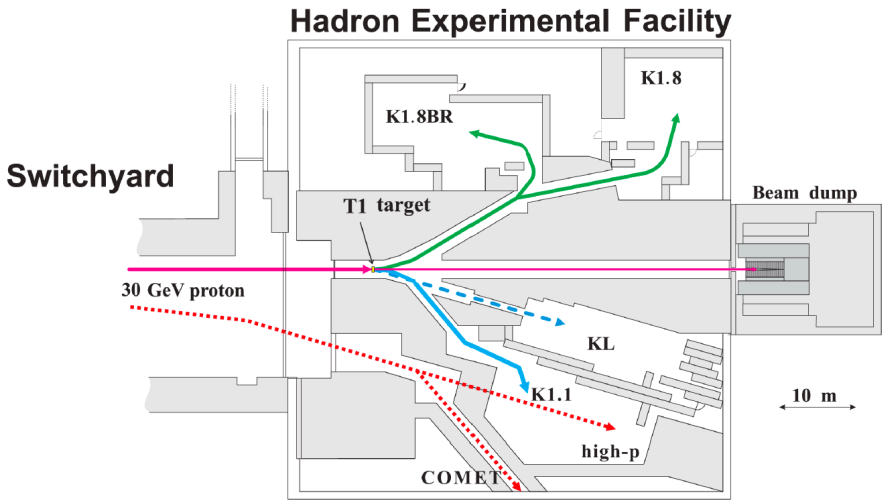

Figure 2.3: J-PARC Hadron Experimental Facility [42]

2.2.2 Spectrometers and Background Suppression Detectors for Identification of the (K^-, π^-) Reaction

In the E63 experiment, we produce Λ hypernuclei by the (K^-, π^-) reaction. We identify the reaction that occurred, through momentum measurement and particle identification of the beam and scattered particles, using a beamline spectrometer and SKS spectrometer, respectively. We ensure that the reaction occurred by momentum measurement and particle identification of beam and scattered particles using a beamline spectrometer and SKS spectrometer, respectively.

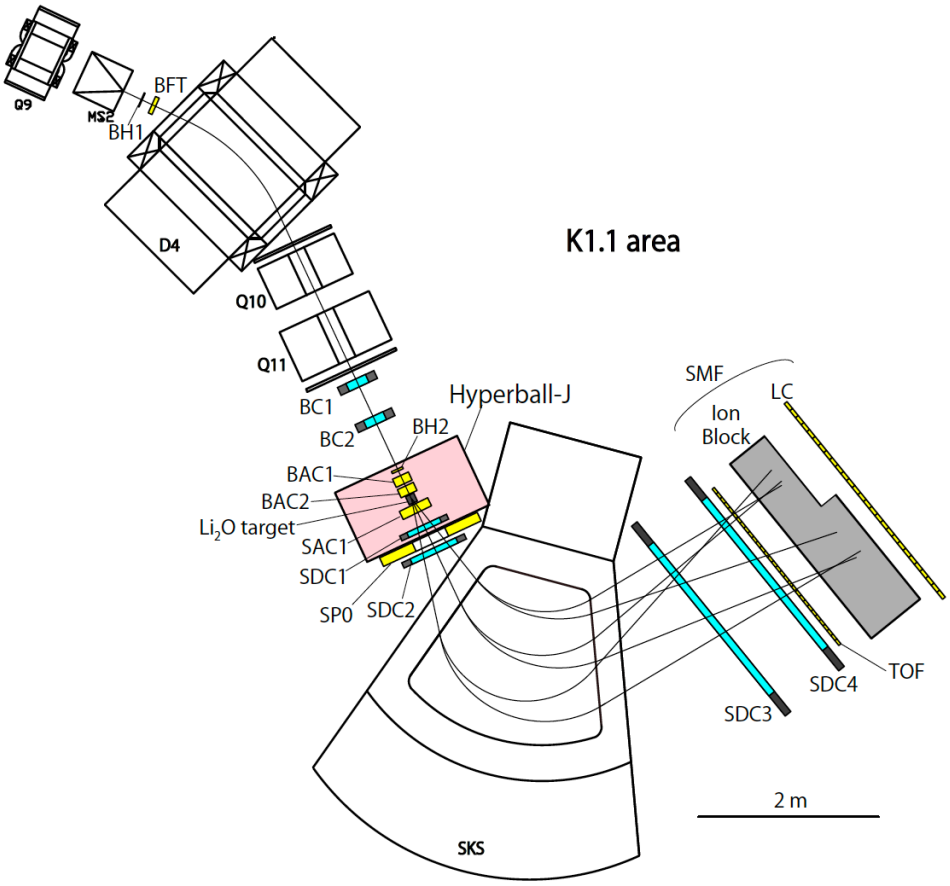

Figure 2.4: K1.1 beamline and an experimental setup for the E63 experiment.

K1.1 beamline spectrometer

The K1.1 beamline spectrometer is used for momentum measurement and particle identification of the beam K^-. The spectrometer is composed mainly of one dipole and two quadrupole magnets (D4, Q10, and Q11) and located at the most downstream of the K1.1 beamline. In addition to the magnets, we install counters: two beam hodoscopes (BH1 and BH2) for measurement of time of flight and two aerogel Cherenkov counters for particle identification (BAC1 and BAC2). We also install tracking detectors: a fiber detector (beam fiber tracker, BFT) and two MWPCs (multi-wire proportional chamber: BC1 and BC2).

Although the beam particles are separated by the electrostatic separators as described in Sect. 2.2.1, negatively charged particles such as π^-, e^- and $\overline{p}$ are con-

taminated in the K^- beam and transported to the experimental target. Thus, the beamline spectrometer has to be equipped with counters for particle identification. Beam K^-s are identified by BAC1 and BAC2 at the following trigger level.

$$K_{in} = \mathrm{BH2} \times \overline{\mathrm{BAC1}} \times \overline{\mathrm{BAC2}}$$

Both of BAC1 and BAC2 are necessary because the beam π^- misidentified as K^- increases the trigger rate.

K^-s are also identified by the time-of-flight method using BH1 and BH2 in offline analysis. We take data with a trigger of (K^-, π^-) and also make π^- trigger with SKS spectrometers and other detectors, as described in the following sections.

SKS spectrometer

We install a superconducting kaon spectrometer (SKS) for momentum measurement and particle identification of scattered π^-. The SKS spectrometer is composed of the SKS magnet, four drift chambers (SDC1-4) for particle tracking, a TOF counter, and an aerogel Cherenkov counter (SAC1).

Specification of the SKS spectrometer for the (K^-, π^-) reaction for kaons with a momentum of 1.1 GeV/c is as follows (Table 2.1).

Table 2.1: Specifications of the SKS spectrometer

Momentum acceptance	$0.7 - 1.1\,\mathrm{GeV/c}$
Momentum resolution	$< 0.2\%$
Bending angle	100°
Magnet field at the center	2.5 T (400 A)
Solid angle	140 msr at maximum
Flight path	about 5 m

Other trigger counters for background suppression

Only with these magnets, chambers, and counters, the background or dummy events are expected to remain in the (K^-, π^-) missing mass spectrum. Possible background events are as follows; (1) misidentified events with a beam K^- going through the target ("beam-though" events) or (K^-, K^-) scattering events at the target and (2) the beam decay of (a) $K^- \to \pi^0\,\pi^-$ (BR = 21%) or (b) $K^- \to \mu^-\,\overline{\nu_\mu}$ (BR = 64%). We install the following trigger counters to suppress the background events of (1), (2a), and (2b).

(1) Beam-thorough veto couter: SFV and SAC3

To suppress the misidentification of the beam-through or scattered K^- as a scattered π^- at SAC1, we install a beam-through veto counter called Scattered forward veto detector (SFV) and an aerogel Cherenkov counter (SAC3). SFV is a segmented plastic scintillation counter installed at the exit of the SKS magnet. We reject all the particles which are regarded as a beam K^- when they are detected by both SFV and SAC3 in the trigger level. The trigger logic of the beam-through K^- ($K^-_{B.T.}$) is defined as

$$K^-_{B.T.} = \mathrm{SFV} \times \overline{\mathrm{SAC3}}.$$

(2) The beam decay

Two cases of K^- decays of $K^- \to \pi^0\,\pi^-$ and $K^- \to \mu^-\,\overline{\nu_\mu}$ must surely be suppressed because the former has the same kinematics as the (K^-, π^-) reaction of hypernuclear production and the latter has a large branching ratio.

(2a) Scattered pion zero detector: SP0

There is a possibility that we misidentify the π^- from the $K^- \to \pi^0\,\pi^-$ decay as a scattered π^- from the (K^-, π^-) reaction. To suppress the π^- from the K^- decay, we detect the π^0 from the K^- decay by installing a π zero detector, SP0. SP0 is an electromagnetic calorimeter made of multi-layered lead sheets and plastic scintillators. In the lead sheets, electromagnetic showers are generated from high energy gamma-rays of $\pi^0 \to 2\gamma$. SP0 rejects $K^- \to \pi^0\,\pi^-$ decay events by tagging the electromagnetic showers.

(2b) Scattered muon filter: SMF

SMF is a detector for rejecting μ^- from $K^- \to \mu^-\,\overline{\nu_\mu}$ decay. It is composed of iron blocks and lucite Cherenkov counters (LC) behind the iron blocks. While π^- mesons induce reactions via strong interaction in the iron blocks, the μ^- penetrates the iron blocks and is detected by LC.

From the (2a) and (2b) cases above, the trigger of K decay event ($\pi^-_{D.E.}$) is defined as;

$$\pi^-_{D.E.} = \mathrm{SP0} + \mathrm{SMF}$$

(K^-, π^-) trigger

In the case that there are hits on BH2 and SAC1, the events are judged as scattered π^- events (π_{out} trigger). However, there are background events from beam-through and beam-decay events. Thus, the real scattered π^- trigger event should include neither of $K^-_{B.T.}$ nor $\pi^-_{D.E.}$. Therefore, the (K^-, π^-) trigger is given as

$$(K^-,\, \pi^-) = K_{in} \times \pi_{out} \times \overline{K^-_{B.T.}} \times \overline{\pi^-_{D.E.}}.$$

2.2.3 Germanium Detector Array for Hypernuclear Gamma-rays Measurement: Hyperball-J

We detect gamma-rays from hypernuclei with Hyperball-J, a large germanium detector array used in hypernuclear gamma-ray spectroscopy at J-PARC. Our group developed and constructed Hyperball-J in 2011-2014 and successfully carried out the E13 experiment with Hyperball-J in 2015. Hyperball-J can be operated under high-intensity conditions using a hadron beam, thanks to a mechanical cooling of the Ge crystals. All the Ge crystals are surrounded by PWO scintillators for background suppression of Compton scattering and high energy gamma-ray from π^0 decay.

Ge detector

The germanium (Ge) detector is a semiconductor detector with a diode made of high-purity Ge crystal and used with a reverse bias applied. When a gamma-ray hits on the Ge crystal, secondary electrons are generated via the interactions of photoelectric effect, Compton scattering and electron-positron pair production. In most cases, the gamma-ray energy is eventually converted to electrons, and the electrons lose their energy while creating many electron-hole pairs in the Ge crystal. The generated electrons and holes are respectively collected by both electrodes and can be read out as electric signals.

Since the bandgap of the Ge crystal is as small as about 0.7 eV, the average energy required for electron-hole pair creation is as small as 2.96 eV, which enables the Ge detector to have a high resolution of about 2 keV for gamma-rays with an energy of 1 MeV.

Since electron-hole pairs are easily created by thermal excitation due to their small bandgap, the current increase and the damage to Ge crystal are serious problems. The hadron beam intensity is very high at J-PARC, and we cannot overlook radiation damage to Ge crystals. It is reported that the effect of radiation damage is suppressed when the Ge crystal temperature is below 80K, lower than that achieved by liquid nitrogen cooling ($\sim$ 90K). Therefore, we need to cool the crystals below 80 K to suppress the radiation damage. We adopt a mechanical cooling method and succeeded in cooling the crystals to 70 K in the E13 experiment.

As shown in Fig. 2.5, Hyperball-J is composed of 32 Ge detectors at maximum,

and we can change the geometrical arrangement of the Ge detectors depending on requirements in each experiment. In the E63 experiment, we plan to use 28 Ge crystals excluding four L-types located downstream as Fig. 2.6 shows. In this arrangement, the Ge detector covers 24% of the total solid angle viewed from the target center.

The photopeak efficiency of each Ge crystal for 1.33 MeV gamma-ray is 60% relatively to that for a ϕ 3 inch×3 inch NaI crystal.

PWO suppression detector

Each Ge detector is surrounded by PWO ($PbWO_4$) scintillation counters. It is used for suppression of background events like high energy gamma-ray events from π^0 decay and Compton scattering events. It is characterized by a high density, a large effective atomic number, and a short decay time (about 10 ns). This decay time is much shorter than that of BGO ($Bi_4Ge_3O_{12}$) (about 300 ns), which enables us to operate the Ge detector array under the high-intensity beam condition at J-PARC.

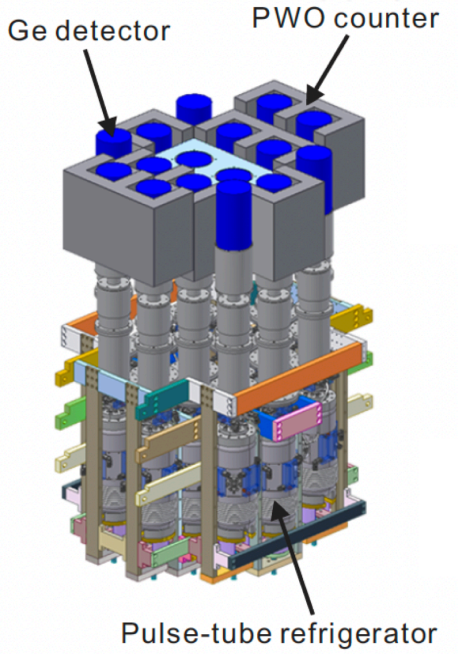

Figure 2.5: Schematic view of the lower half of the Hyperball-J [43].

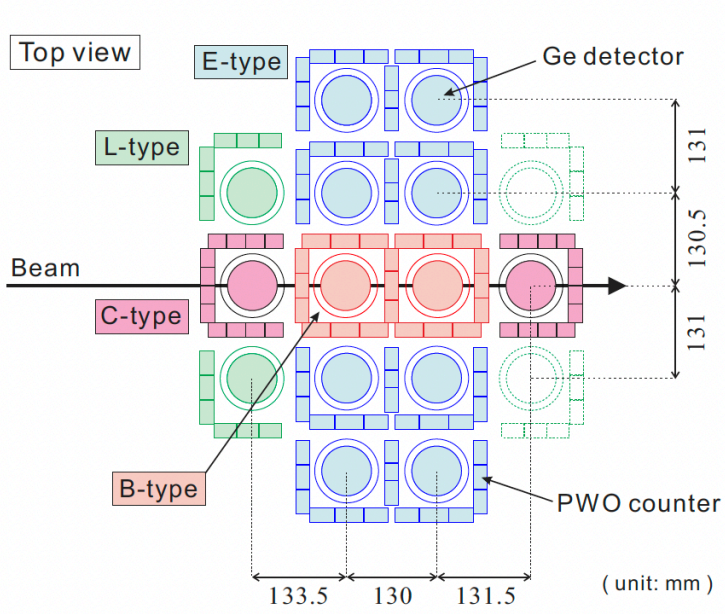

Figure 2.6: Arrangement of the Ge detectors and the PWO counters of Hyperball-J view from the target center to the bottom. In the E63 experiment, we plan to use 28 Ge crystals except for four L-types located downstream [43].

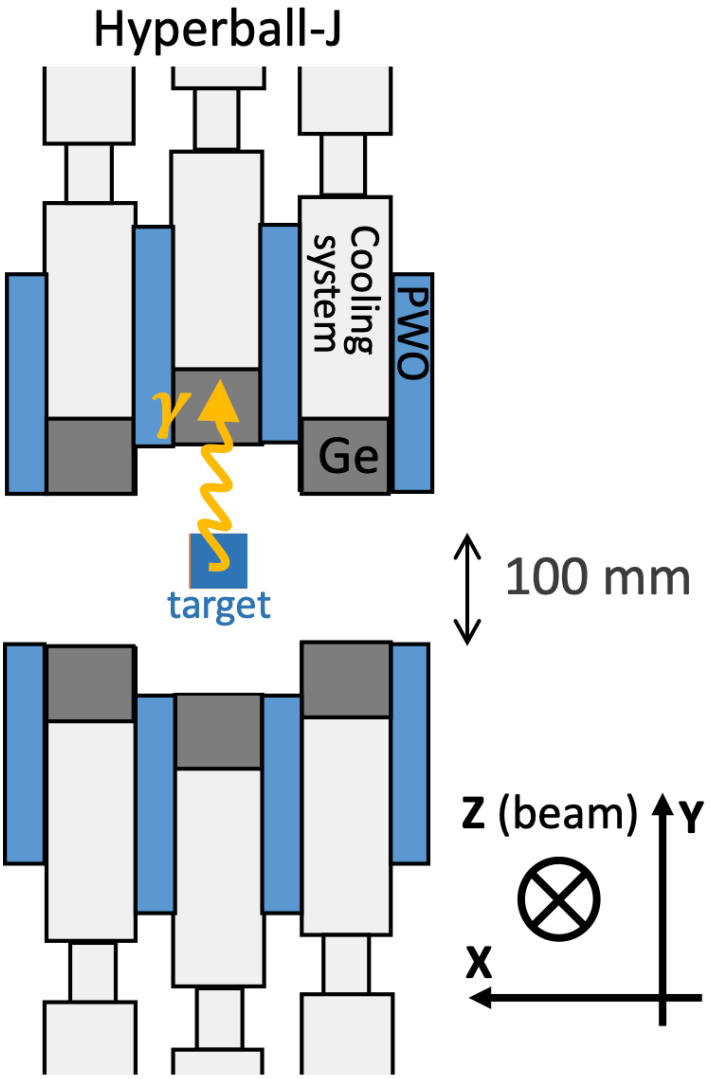

Figure 2.7: Arrangement of the Ge detectors and the PWO counters of Hyperball-J viewed from the beam direction.

2.3 Data Acquisition System

We use a network-based data acquisition (DAQ) system called HD-DAQ with a DAQ software using the TCP/IP and trigger/tag distribution system which was developed for experiments at J-PARC Hadron facility [44].

In the K1.1 and K1.8 beamlines, the Event Builder program in the main computer collects data from each front-end computer for each detector group and integrates the data into one-event data. In this distributed DAQ system, a trigger/tag distribution module (Master Trigger Module, MTM) and a reception module (Receiver Module, RM) play an important role (as described again in Sect. 3.3.3).

2.4 New Detector System for Identifying Nuclides

Highly excited states of ${}^{7}_{\Lambda}$Li could decay with emission of hyperfragments of ${}^{3}_{\Lambda}$H, ${}^{4}_{\Lambda}$H, ${}^{4}_{\Lambda}$He, ${}^{5}_{\Lambda}$He, ${}^{6}_{\Lambda}$He, and ${}^{6}_{\Lambda}$Li. By identifying the (K^-, π^-) reaction and measuring the momenta of K^- and π^-, the missing mass gives the energy of the ${}^{7}_{\Lambda}$Li excited state. By limiting the excitation energy, it becomes possible to choose the hyperfragment production threshold. However, since this method produces all the hyperfragments above the production threshold, it seems difficult to identify the nuclide of the hypernucleus from which measured gamma-ray is emitted. In the case that we want to enhance the ${}^{4}_{\Lambda}$H production, for example, many hypernuclei can be produced as Fig. 2.1 showed. Therefore, we need to identify the nuclide of the hyperfragment by installing a new detector for nuclide identification in the system in order to measure and identify gamma-rays from the hyperfragments.

Chapter 3

Detector System for Identification of Secondary Hypernuclei

When the ${}^{7}_{\Lambda}$Li hypernuclei produced in the ^{7}Li (K^-, π^-) reaction are highly excited, they decay with production of various kinds of secondary hypernuclei (hyperfragments) via strong interaction. In order to identify ${}^{4}_{\Lambda}$H and ${}^{3}_{\Lambda}$H among them, we plan to install a new detector system. In this chapter, I describe a nuclide identification method using the detector system, requirement for the detector and the detector configuration.

3.1 Triple Coincidence Method for Identification of Secondary Hypernuclei

In the ^{7}Li (K^-, π^-) reaction, various kinds of secondary hypernuclei are produced, and gamma-rays from those hypernuclei can be detected. We should determine which hypernucleus emitted the gamma-ray observed by the Hyperball-J. By selecting an optimum region of the excitation energy of ${}^{7}_{\Lambda}$Li, we can enhance the yield of a certain nuclide of secondary hypernucleus, which helps us to identify which hypernucleus emits the observed gamma-ray. Only by selecting the energy region, however, we cannot unambiguously identify the nuclide as explained in Sect. 2.4. We focus on monochromatic pions emitted when ${}^{4}_{\Lambda}$H or ${}^{3}_{\Lambda}$H decay via weak interaction. Since these pions have a characteristic kinetic energy, we can unambiguously identify the hypernucleus which emitted the gamma-ray.

We identify the (K^-, π^-) reaction by momentum measurement and particle identification of the beam particles and the scattered particles using spectroeters in front of and behind the target, and we accurately measure gamma-ray energy by

the Hyperball-J array. Simultaneously, we plan to measure the kinetic energy of π^- from the weakly decaying hypernucleus by using a detector that is newly installed. In this way, in the E63 experiment, we identify the nuclide of secondary hypernuclei via a triple coincidence measurement of the (K^-, π^-) reaction for the hypernuclear production, gamma-rays from the hypernucleus, and π^- from the weak decay of the hypernucleus. This triple coincidence method has never been performed yet. If we establish this method, we can conduct gamma-ray spectroscopy experiments of various hyperfragments which cannot be directly produced by the (K^-, π^-) or (π^+, K^+) reactions.

3.2 Requirement for the Range Counter System

Highly-excited states of ${}^{7}_{\Lambda}$Li produced in the ^{7}Li (K^-, π^-) reaction decay by emitting a hyperfragment, for instance, such as ${}^{7}_{\Lambda}\mathrm{Li}^* \rightarrow {}^{4}_{\Lambda}\mathrm{H} + {}^{3}\mathrm{He}$ and ${}^{7}_{\Lambda}\mathrm{Li}^* \rightarrow {}^{3}_{\Lambda}\mathrm{H} + {}^{4}\mathrm{He}$. The ${}^{4}_{\Lambda}$H and ${}^{3}_{\Lambda}$H emit a monochromatic π^- via the weak decay; ${}^{4}_{\Lambda}\mathrm{H} \rightarrow {}^{4}\mathrm{He} + \pi^-$ and ${}^{3}_{\Lambda}\mathrm{H} \rightarrow {}^{3}\mathrm{He} + \pi^-$. In order to identify the hypernucleus, we measure the kinetic energies of these pions by installing a new detector system.

Detection method

It is difficult to install a magnetic spectrometer for momentum measurement of the π^- due to spatial limitations around the target where the Hyperball-J covering a large solid angle is installed. Although it is also possible to install a calorimeter to measure the kinetic energy of π^-, the π^- reacts with nucleons within the calorimeter via strong interaction, which leads to nuclear destruction. The total energy measured by the calorimeter could be larger than the kinetic energy of π^-, which is unsuitable for our purpose. Therefore, we decided to install a multi-layered plastic scintillator and measure the range of π^- to determine their kinetic energy.

Spatial limitation and signal readout

Hyperball-J and other trigger counters are installed around the target, and the range counter system needs to be compact due to spatial constraints. Also, since the SKS spectrometer is nearby, it is necessary to adopt a readout method that is not affected by the magnetic field. That is why we use not a photomultiplier tube (PMT) but a semiconductor photosensor called SiPM (silicon photomultiplier). We also use wavelength-shifting fibers by embedding them into a plastic scintillator slab for efficiently collecting photons and guiding them to the small number of SiPMs.

Pion separation

The kinetic energies of the monochromatic pions from the weak decay of ${}^{4}_{\Lambda}$H and ${}^{3}_{\Lambda}$H are 53 MeV and 40 MeV, respectively. The branching ratios of these two-body weak decays are 50% and 27%, respectively. In addition to ${}^{4}_{\Lambda}$H and ${}^{3}_{\Lambda}$H, ${}^{6}_{\Lambda}$He also decays into two bodies with an emission of π^- with 37 MeV. This pion should be separated from the pions from ${}^{4}_{\Lambda}$H and ${}^{3}_{\Lambda}$H: $\pi^-({}^{4}_{\Lambda}\mathrm{H})$ and $\pi^-({}^{3}_{\Lambda}\mathrm{H})$. Other fragments decay into three bodies with an emission of a pion, but these pions do not matter here; these pions have a kinetic energy less than that of the pion from ${}^{6}_{\Lambda}$He. The requirement for the range counter system is to separate two peaks from $\pi^-({}^{4}_{\Lambda}\mathrm{H})$ and $\pi^-({}^{3}_{\Lambda}\mathrm{H})$ in the range spectrum with a confidence level of more than 3σ.

By selecting the missing mass of ${}^{7}_{\Lambda}\mathrm{Li}^*$, we can enhance the production of ${}^{4}_{\Lambda}$H and ${}^{3}_{\Lambda}$H and obtain gamma-ray energy spectra. In the gamma-ray spectra, we select the peak regions of the gamma-rays from ${}^{4}_{\Lambda}$H and ${}^{3}_{\Lambda}$H, and additionally, among the gamma-ray peak events, we choose the events for which we measured a weak-decay pion in coincidence. For the coincidence events, if the kinetic energy matches those of the pions from ${}^{4}_{\Lambda}$H or ${}^{3}_{\Lambda}$H, the nuclide of the hypernucleus is identified. We identify the hypernucleus according to the following criteria: (1) A mean value of the kinetic energy of pions measured by the detector matches the expected kinetic energy of the pions from ${}^{4}_{\Lambda}$H or ${}^{3}_{\Lambda}$H within an error and (2) the pion kinetic energy from the other hypernucleus is away from the mean value by more than 3σ. When the measured energy value for pions from one of the hypernucleus is obtained within 1σ from the kinetic energy, we can identify the nuclide if the value is away more than 3σ from kinetic energy of pions from another hypernucleus. Therefore, the energy resolution of the detector is required to be $(53-40)/4 \simeq 3\,\mathrm{MeV}$, or the range resolution to be 5.8 mm.

In this estimation of the required energy resolution, the pions from ${}^{6}_{\Lambda}$He are not included because even if the excited state could deexcite with a gamma-ray emission, the energy is small, and therefore we can identify the hypernucleus.

The number of triple coincidence events is expected to be 30 and 55 in 6 days beamtime, respectively [45], on the assumption that the efficiency of the gamma-ray measurement is 6% for ${}^{4}_{\Lambda}$H, and 3% for ${}^{3}_{\Lambda}$H, and the efficiency of the weak-decay pion measurement is 10%. Table 3.1 shows the number of expected triple coincidences for ${}^{4}_{\Lambda}$H and ${}^{3}_{\Lambda}$H.

Table 3.1: Summary of monochromatic pions from ${}^{4}_{\Lambda}$H, ${}^{3}_{\Lambda}$H, and ${}^{6}_{\Lambda}$He

	$\pi^-({}^{4}_{\Lambda}\mathrm{H})$	$\pi^-({}^{3}_{\Lambda}\mathrm{H})$	$\pi^-({}^{6}_{\Lambda}\mathrm{He})$
Kinetic energy [MeV]	53	40	37
Range in plastic counter [mm]	99.5	64.6	55.2
Number of expected triple coincidences	30	55	

Tracking pions

By employing a range counter made of a multi-layered plastic scintillator slab, we can obtain information only information on the depth where the π^- stopped within the detector. However, if the incident angle of π^- is unknown, the range along the track is not accurately obtained. Therefore, we have to install a position detector that determines entering positions of π^- in front of the range counter, so as to obtain the incident angle of π^- with respect to the range counter. Since the π^- emission point (weak decay point) can be assumed to be the same as the (K^-, π^-) reaction point, we can obtain the incident angle by additionally measuring the entering position of π^-.

Previous study by a Monte Carlo simulation

In a previous research [46], the thickness of one layer of the range counter is optimized by a Monte Carlo simulation. In the simulation, the detector system for nuclide identification consists of a range counter of a multi-layered plastic scintillator and a position detector, and it was examined whether we can distinguish π^-s from weak decays of ${}^{4}_{\Lambda}$H and ${}^{3}_{\Lambda}$H.

The pions interact with nuclei in the detector via strong as well as electromagnetic interactions, and the distribution of the last layer where it has energy deposit becomes more complicated with hadronic interaction than without it as shown in Fig. 3.1. The optimum thickness of one layer was found to be 10 mm in a Monte Carlo simulation [46]. With the strong interaction, various particles are produced from a nuclear reaction after π^- stops and the produced particles give their energy to the layers deeper than the layer where the π^- stops, which results in misidentification of the π^- stop layer.

Figure 3.2 shows typical π^- stop events obtained in the simulations with/without the hadronic interaction [46]. Without the hadronic interaction, the energy loss in each layer should draw a Bragg curve calculated with the assumption that particles lose their energy only via the electromagnetic interaction like Fig. 3.2 (1) As seen in Fig. 3.2 (2), the energy loss in some layers with the hadronic interaction is likely

to be much higher than that without the hadronic interaction. It is difficult to determine the stop layer in real experiments.

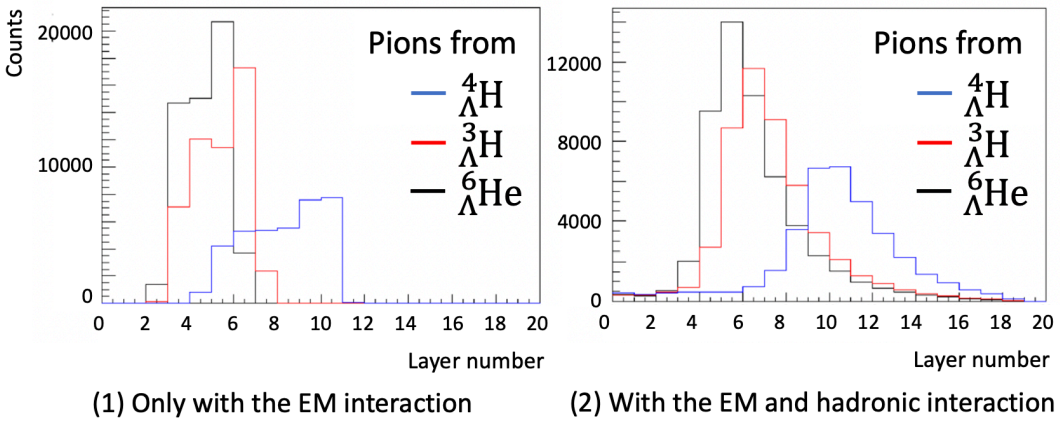

Figure 3.1: Simulated distribution of the last layer with energy deposit in the range counter (one layer thickness: 10 mm) [46] (1) only with the electromagnetic interaction and (2) with the electromagnetic and hadronic interactions.

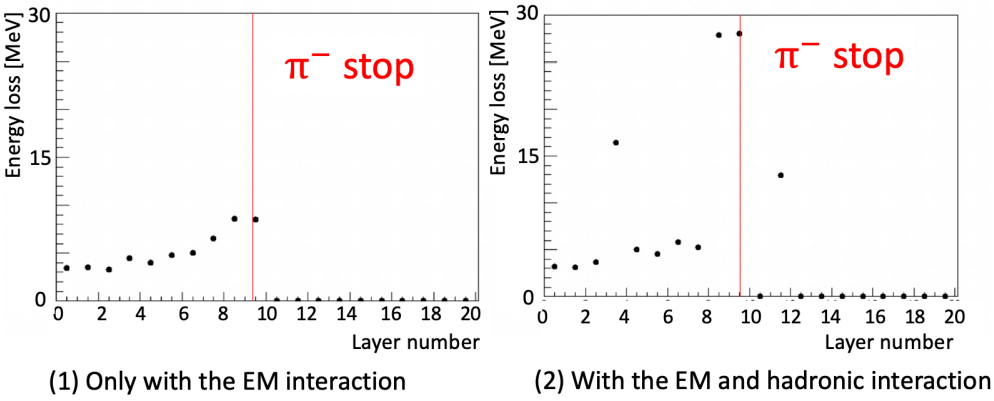

Figure 3.2: Energy loss in each layer of the range counter for a typical event simulated (1) only with the electromagnetic interaction and (2) with the electromagnetic and hadronic interactions [46]. Energy loss in some layers with the hadronic interaction is often much higher than without the hadronic interaction.

Figure 3.3 shows the relation between the energy resolution (simga) and the thickness of each layer of the range counter. The sigma is the standard deviation of the π^- energy distribution. The simulation also shows that ${}^{4}_{\Lambda}\mathrm{H}$ and ${}^{3}_{\Lambda}\mathrm{H}$ can be distinguished with a range counter whose each layer is less than 10 mm thick, by taking into account the energy deposit in the target and the position detector, as well as the incident angle of π^- obtained from hit information of the position detector and the weak-decay π^- emission point obtained as the reaction point of (K^-, π^-) (See Sect. 3.3.2 for details). In the simulation, the hadronic interaction is taken into account, but the hadronic reaction process with nuclei incorporated in the simulation could be different from the real interaction, and therefore, we determined the thickness to be 6 mm by taking a safety factor.

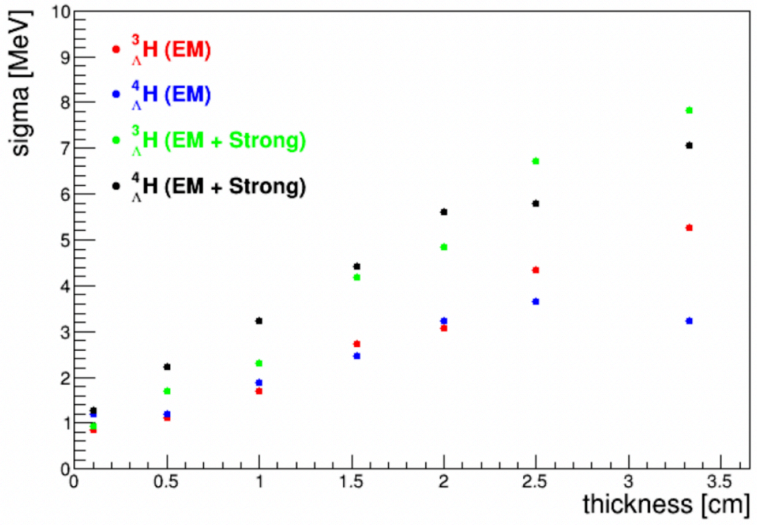

Figure 3.3: The relation between the energy resolution (simga) and the thickness of each layer of the range counter estimated in a simulation [46]. The sigma is the standard deviation of the π^- energy distribution.

3.3 Detector Design

In a previous study, a one-layer prototype was built for testing the performance. The prototype adopted a signal readout using wavelength-shifting fiber and SiPMs. Scintillation photons with wavelength of $400 - 500\,\mathrm{nm}$ are converted in the wavelength-shifting fiber embedded in the plastic scintillator to green photons with a wavelength

of 476 nm at the emission peak, and the photons are transported along the fiber to the SiPM at the end of the fiber. The wavelength of photons emitted from the wavelength-shifting fiber matches a peak sensitivity wavelength of SiPM.

As the result of the test using plastic scintillator slabs of 5, 10, and 15 mm thick with two, four, and six wavelength-shifting fibers, they found that there is no significant difference in the light yield among the three thicknesses and the energy resolution around 2 MeV (better than the range straggling limit) was achieved in any of the thicknesses. They found any of the thicknesses to be good and any of the numbers of fibers to be good. Therefore, the thickness was determined to be 6 mm and the number of fibers to be two.

The detector design was determined as shown in Fig. 3.4. It is made of 24 layers of 6 mm-thick plastic scintillator slabs. Scintillation photons are converted and transported in the wavelength-shifting fibers embedded in the two sides of the scintillator, and read out with SiPMs attached to each of the fibers. In front of the range counter (RC), a plastic scintillator hodoscope as a position detector for pions (PD) is installed. Thanks to the position detector, the ambiguity of the range due to angular uncertainty is removed.

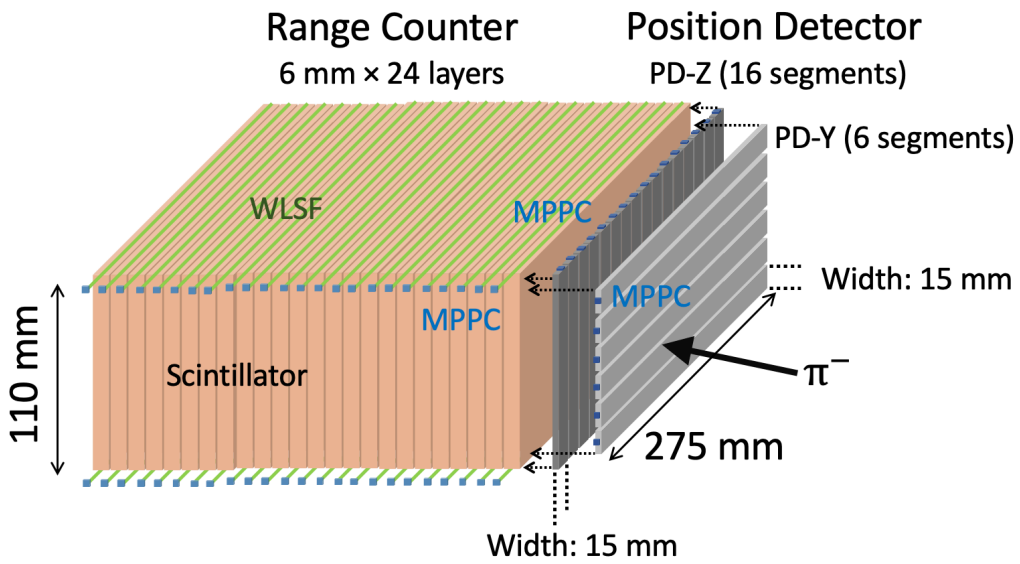

Figure 3.4: Range Counter and Position Detector. The range counter is made of 24 layers of 6 mm-thick plastic scintillator slabs. We adopted the readout method using wavelength-shifting fibers and SiPMs. In front of the range counter, a plastic scintillator hodoscope as a position detector for pions is installed. PD is composed of PD-Y (6 segments of plastic hodoscope) and PD-Z (16 segments of plastic hodoscope).

Figure 3.5 shows two sets of the range counter systems installed inside the Hyperball-J Ge detector array. They are installed on the left and right side of the target when viewed from the beam direction. The overall dimensions of the system were determined to be $155^x \times 125^y \times 295^z\,\mathrm{mm}^3$ so that the system would just fit into the available room in the Hyperball-J. The distance to the target center was determined to be 85 mm so as not to affect the measurement efficiency by Hyperball-J by a relative value higher than 4%. The total solid angle is 10% from the target center.

Many types of range counters have been used so far in nuclear physics, and signals are read with PMTs commonly in those range counters. In this range counter, the signals are read out using WLSF and SiPM, which makes the detector compact. It is a unique feature of this range counter system.

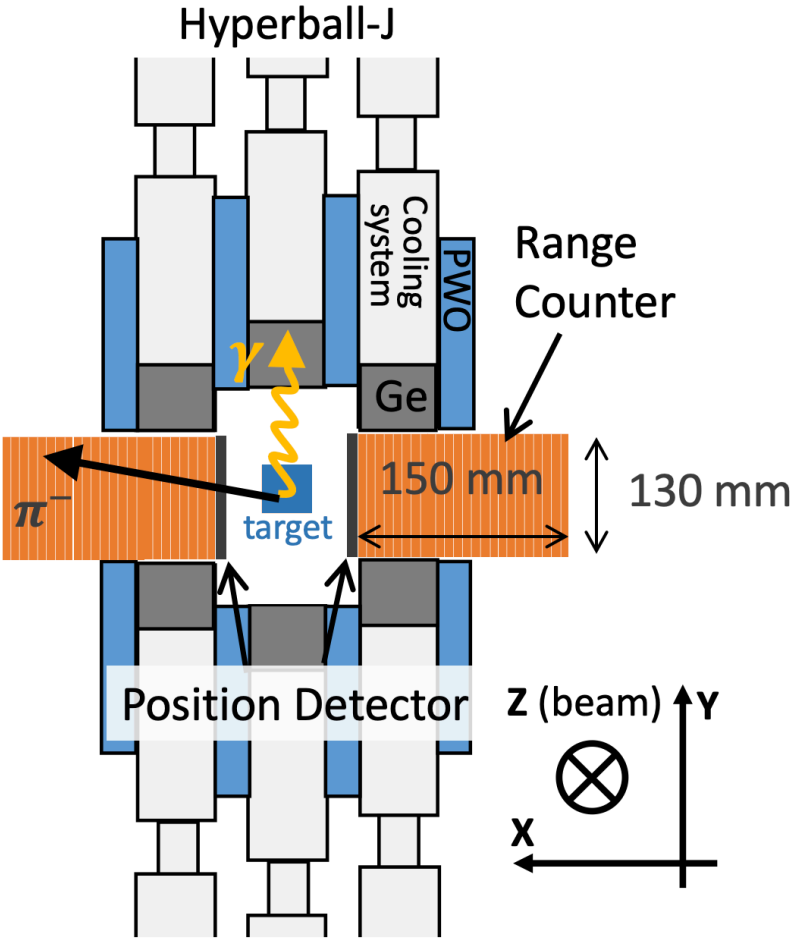

Figure 3.5: Two sets of range counter systems installed inside the Hyperball-J. They are installed on the left and right side of the target when viewed from the beam direction. The total solid angle is 10%.

3.3.1 Range Counter

As shown in Fig. 3.4, semi-cylindrical grooves are dug on the surface of the top and bottom sides of each scintillator slab and wavelength-shifting fibers are embedded. The light from each fiber is read out by a SiPM (MPPC) developed by Hamamatsu. Twenty-four layers of 6 mm scintillator slabs are stacked. The total thickness is 144 mm, which is enough for stopping the pion from ${}^{4}_{\Lambda}\mathrm{H}$ decay with a range of 99.5 mm.

The scintillator slabs are fixed with an aluminum frame with a thickness of 3 mm. Although this aluminum frame should affect the efficiency of Hyperball-J around the range counter due to interaction with gamma-rays, it turns out that the effect is negligibly small; The efficiency is reduced by a relative value of 4% with

the range counter installed, according to a calculation taking the photon absorption coefficient of aluminum into account.

Details of the plastic scintillator, the wavelength-shifting fiber, and the SiPM are described below.

Plastic scintillator

We fabricated the range counter using plastic scintillator EJ-200, of which properties are shown in Table 3.2. The dimensions of one layer slab of the range counter are 275mm × 110mm × 6mm.

We dug semi-cylindrical grooves for embedding fibers on the surface of the top and bottom sides of the scintillator slab and polished the entire surface of the scintillator slab well. We wrapped each scintillator slab with polytetrafluoroethylene (PTFE) sheet that diffusely reflects scintillation photons with high reflectance. We used raw PTFE sheet (Teflon) made by Chukoh. This 0.1 mm thick Teflon sheet reflects the photon with 400 nm wavelength at 100% reflectance compared to $BaSO_4$, which enables scintillation photons not to leak from the scintillator slab.

Table 3.2: Specifications of the plastic scintillator EJ-200

PROPERTIES	**EJ-200**
Scintillation Efficiency (Photons/1 MeV e^-)	10,000
The wavelength of Maximum Emission [nm]	425
Light Attenuation Length [cm]	380
Rise Time [ns]	0.9
Decay Time [ns]	2.1
Pulse Width, FWHM [ns]	2.5
No. of H [$10^{22}/cm^3$]	5.17
No. of C [$10^{22}/cm^3$]	4.69
No. of e^- [$10^{22}/cm^3$]	3.33
Density [g/cm^3]	1.023
Polymer Base	Polyvinyltoluene
Refractive Index	1.58

Wavelength-shifting fiberes

Wavelength-shifting fiber (WLSF) is a type of plastic scintillation fiber (PSF). The core (inside) is made of polystyrene resin containing a fluorescent agent, and the clad (outside) is made of one or two layers of methacrylic resin. The photon that

enters the optical fiber from the side normally goes out because it cannot satisfy the conditions for total reflection, and the photon cannot be transmitted by the fiber. However, by mixing the wavelength-shifting material in the core, the fiber core absorbs the entered blue photon and isotropically emits a photon with a green wavelength, which is then transmitted along the fiber with a high probability.

In the range counter, we used a single-clad type WLSF, Kuraray-Y11. It emits green light (emission peak: 476 nm) when scintillation photons enter. The properties of Y-11 with a diameter of 1.0 mm used this time are shown in table 3.3. The absorption peak matches the emission peak of EJ-200.

Table 3.3: Properties of Kuraray Y11 wavelength-shifting fiber

PROPERTIES	**Y-11**
Diameter [mm]	1.0
Emission color	green
Emission peak [nm]	476
Absorption peak [nm]	430
Attenuation length [m]	>3.5

Multi-Pixel Photon Counter, MPPC

To detect photons transmitted through the WLSF, we use a semiconductor photon sensor called SiPM. It is a photon-counting device composed of a multi-pixel Geiger mode Avalanche Photo Diode (APD). We use SiPMs named as Multi-Pixel Photon Counter (MPPC) developed by Hamamatsu. By operating an APD with a reverse voltage higher than the breakdown voltage, avalanche amplification occurs after a photon enters and an electron-hole pair is created, generating a device-specific saturated output that does not depend on the number of incident photons. This process is called Geiger discharge because it is similar to the Geiger mode in gas counters. Once a Geiger discharge occurs, it continues to discharge as long as the electric field inside the device is maintained. Thus, it is necessary to stop the discharge to detect successive photons. In MPPC, a method of connecting a quenching resistor in series with the APD is adopted to stop the avalanche amplification in a short time. A basic unit (pixel) consists of an APD and a quenching resistor. Several tens or hundreds pixels are combined and arranged two-dimensionally, and a signal proportional to the number of pixels which receive photons is emitted; when the number of incoming photons is much smaller than the number of pixels, photon counting is possible (Figure 3.6).

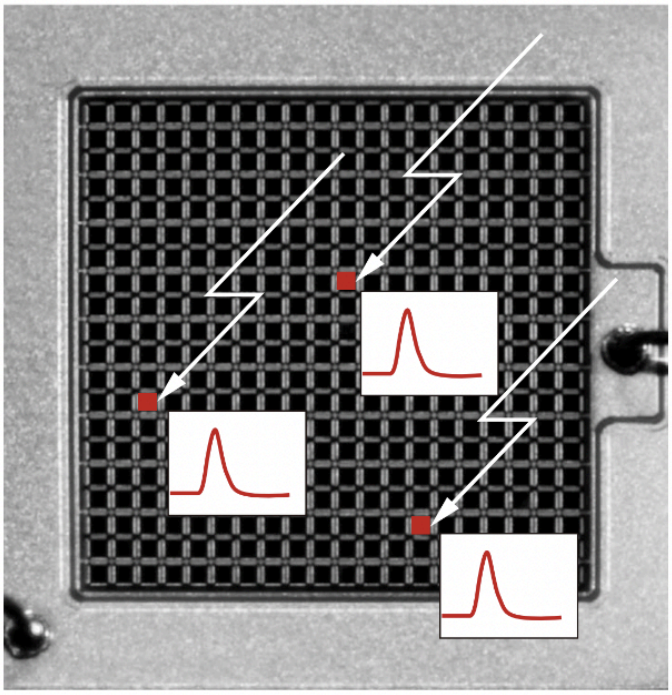

Figure 3.6: Conceptual diagram of photon counting in MPPC. A basic unit (pixel) is arranged two-dimensionally and each pixel emits a signal when a photon enters. The sum of the signals is proportional to the number of hit pixels, which is almost proportional to the number of incoming photons on the MPPC [47].

MPPC is characterized by a small afterpulse, low crosstalk, low dark counts, a high multiplication factor, and good time resolution. In addition, because of its small size, it is suitable for reading out detectors installed around targets with space constraints. Since it is a semiconductor detector not affected by magnetic fields, and then it is also suitable for reading out near the SKS spectrometer. For the above reasons, I adopted MPPCs for reading the signals of the range detector system.

The model number of the MPPC used for the range detector is S13360-1325PE. The size of the light receiving window is $1.3 \times 1.3\,\mathrm{mm}^2$. The number of pixels is 2668

and the pixel pitch is 25 μm. The fill factor (the fraction of the photon-sensitive area over the MPPC window area) is 47%. Details of the specifications are summarized in Table 3.4.

The longer the pixel pitch is, the larger the fill factor is, but the worse the linearity between the photon number and signal height becomes at the same time. For use with the range counter, we do not need to accurately measure the energy loss in the counter like a calorimeter, but we need to acquire an ADC value of the MPPC signal to know the energy loss information in each layer. Therefore, we chose the type of MPPC with a relatively small fill factor so that the linearity is sustained over a wide range of light amounts.

The MPPC has a large temperature dependence. According to the specification sheet, the recommended operation voltage changes 54 mV per 1 K ($\Delta T_{V_{op}}$ in Table 3.4).

This MPPC is also used in a position detector described later.

Table 3.4: Specifications of MPPC (S13360-1325PE). The detection efficiency is for the wavelength with the peak sensitivity, 450 nm.

PROPERTIES	**MPPC S13360-1325PE**
Pixel pitch [μm]	25
Effective photosensitive area [mm^2]	1.3×1.3
Number of pixels	2668
Fill factor [%]	47
Spectral response range wavelength [nm]	320 to 900
Peak sensitivity wavelength [nm]	450
Gain	7.0×10^5
Breakdown voltage [V]	53±5
Crosstalk probability [%]	1
Temperature coefficient at a recommended operating voltage $\Delta T_{V_{op}}$[mV/K]	54
Detection efficiency [%]	25

3.3.2 Position Detector

It is impossible to obtain the incident angle of π^- only with the range counter. Therefore, we install a position detector (PD) in front of the range counter. A highly excited state of ${}^{7}_{\Lambda}$Li is produced from the (K^-, π^-) reaction in the target. The secondary hypernucleus is emitted and stopped in the target, and then it decays weakly by releasing π^-. If we know a point where the π^- is released in the target and the position where the π^- passes on the position detector, we can obtain the angle

of incidence on the range counter. However, we can measure not the emission point of π^- but the reaction point of the (K^-, π^-), that is, the production point of ${}^{7}_{\Lambda}\mathrm{Li}^*$. Therefore, we can obtain the angle of incidence on the range counter only under the assumption that the π^- is emitted from the reaction point of the (K^-, π^-) reaction. This assumption does not matter because the momentum transfer is rather small ($70 - 160\,\mathrm{MeV}/c$) in the (K^-, π^-) reaction at $0.9 - 1.1\,\mathrm{GeV}/c$ (scattering angle: $0^\circ - 10^\circ$). Assuming that produced hypernuclei of ${}^{4}_{\Lambda}\mathrm{H}$ and ${}^{3}_{\Lambda}\mathrm{H}$ have momenta of $160\,\mathrm{MeV}/c$ at maximum, their ranges in the ^{7}Li target are estimated to be less than 2 mm, where the value is much less than the σ_z of the spatial resolution of (K^-, π^-) reaction point: (σ_x, σ_y, σ_z) = (1.2, 2.6, 22) [mm] in the previous gamma-ray spectroscopic experiment of ${}^{4}_{\Lambda}\mathrm{He}$ (E13). The same resolution as the E13 is expected in the E63. From the information on the angle and the stop layer in RC, the range is obtained. In addition, we also obtain the path length of the weak decay π^- in the target and estimate the energy loss in the target.

The spatial resolution of the (K^-, π^-) reaction point is expected to be (σ_x, σ_y, σ_z) = (1.2, 2.6, 22) [mm] also in the E63 experiment. Thus, it is not necessary to place a detector with positional accuracy of less than 1 mm, such as a drift chamber. Therefore, we adopted two layers of plastic hodoscopes as the position detector and measure the incident point of the π^- to the range counter. PD is composed of two layers of a hodoscope for measuring the y and z positions (PD-Y and PD-Z). We determined the width of one strip from estimation of PD width dependence on the position resolution of the range counter. The range resolution is determined by the position resolutions of the reaction vertex, the range counter, and the position detector. We examined relationship between the range resolution and PD-Y resolution ($\sigma_{\mathrm{PD_Y}}$) and between the range resolution and PD-Z resolution ($\sigma_{\mathrm{PD_Z}}$), assuming the resolutions of the vertex to be the same as those in E13. The required range resolution for separating ${}^{4}_{\Lambda}\mathrm{H}$ and ${}^{3}_{\Lambda}\mathrm{H}$ is:

$$\sigma_{\pi^-({}^{4}_{\Lambda}\mathrm{H})} + \sigma_{\pi^-({}^{3}_{\Lambda}\mathrm{H})} < (\text{range difference of pions})/3 := \Delta\mathrm{R}/3,$$

where the range difference ΔR is 34.9 mm. The estimation is done for the case where pions enter the range counter with the largest angle, which corresponds to the worst resolution (Fig. 3.7). There is no $\sigma_{\mathrm{PD_Y}}$ dependence in the range resolution with a fixed $\sigma_{\mathrm{PD_Z}}$ to 10 mm (Fig. 3.8). This is well understood considering that the position resolution of the vertex z is the worst and all the y components of the position resolutions including $\sigma_{\mathrm{PD_Y}}$ have almost no effect on the range resolution. On the contrary, the range resolution is dependent on $\sigma_{\mathrm{PD_Z}}$ (Fig. 3.9). Here, $\sigma_{\mathrm{PD_Y}}$

is fixed to 10 mm. It can be seen that the range resolution converges to a certain value in the regions smaller than around $\sigma_{\mathrm{PD_Z}} = 10\,\mathrm{mm}$. Therefore, we determined the width of both PD-Y and PD-Z to be 15 mm corresponding to $\sigma_{\mathrm{PD_Y}}$ and $\sigma_{\mathrm{PD_Z}}$ of less than 5 mm.

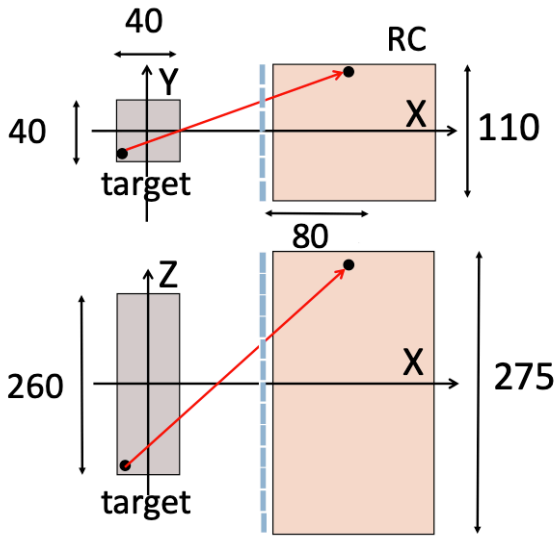

Figure 3.7: A pion track (red line) used for estimating the range resolution, where pions enter the range counter with the largest angle, which corresponds to the worst resolution.

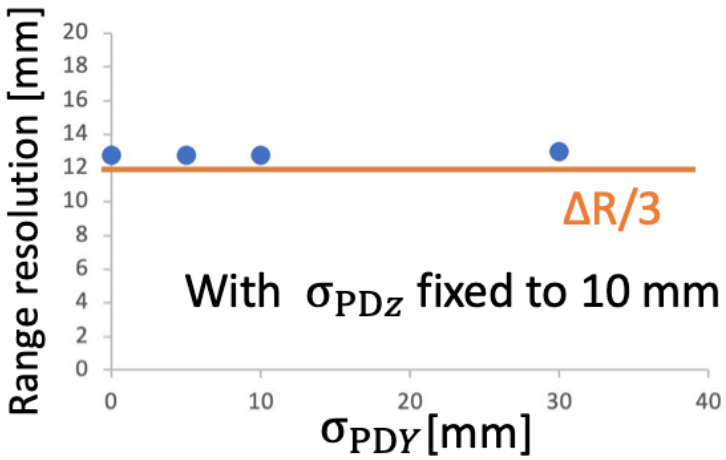

Figure 3.8: Calculated $\sigma_{\mathrm{PD_Y}}$ dependence of the range resolution, showing no $\sigma_{\mathrm{PD_Y}}$ dependence in the range resolution with a fixed $\sigma_{\mathrm{PD_Z}}$ to 10 mm.

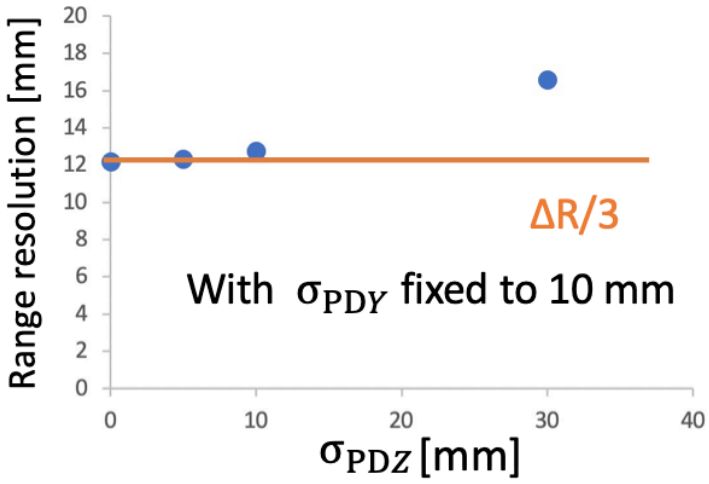

Figure 3.9: Calculated $\sigma_{\mathrm{PD_Z}}$ dependence of the range resolution. $\sigma_{\mathrm{PD_Y}}$ is fixed to 10 mm.

The dimensions of the one segment and the number of segments are 15 mm × 275 mm × 3 mm and 6 segments for PD-Y and 15 mm × 110 mm × 3 mm and 16 segments for PD-Z. Each segment is wrapped with Teflon sheet for light reflection in the same way as the range counter.

Unlike the range counter, in the PD, scintillation photons are read out by a MPPC directly attached to one end of the scintillator slab without WLSFs, because we just need to know the hit information on the PD and we do not need so many photon counts. As described in Sect. 5.1, more than about 10 photons are obtained using a ^{90}Sr source, of which photon yield is sufficient for our purpose.

Triple coincidence measurement with the range counter system

We identify the (K^-, π^-) reaction by momentum measurement and particle identification of the beam particles and the scattered particles using the K1.8 spectrometer installed upstream of the target and the SKS spectrometer installed downstream of the target, respectively. We accurately measure energies of gamma-rays emitted from excited hypernuclei by the Hyperball-J. Simultaneously, we measure the kinetic energy of π^- from the weakly decaying hypernucleus with the range counter system, focusing on monochromatic pions emitted from ${}^{4}_{\Lambda}$H or ${}^{3}_{\Lambda}$H decay via weak interaction. Employing the range counter system, we identify the nuclide of the secondary hypernuclei by performing a triple coincidence measurement of the (K^-, π^-) reaction, gamma-rays from the hypernucleus, and a π^- from the weak decay of the hypernucleus.

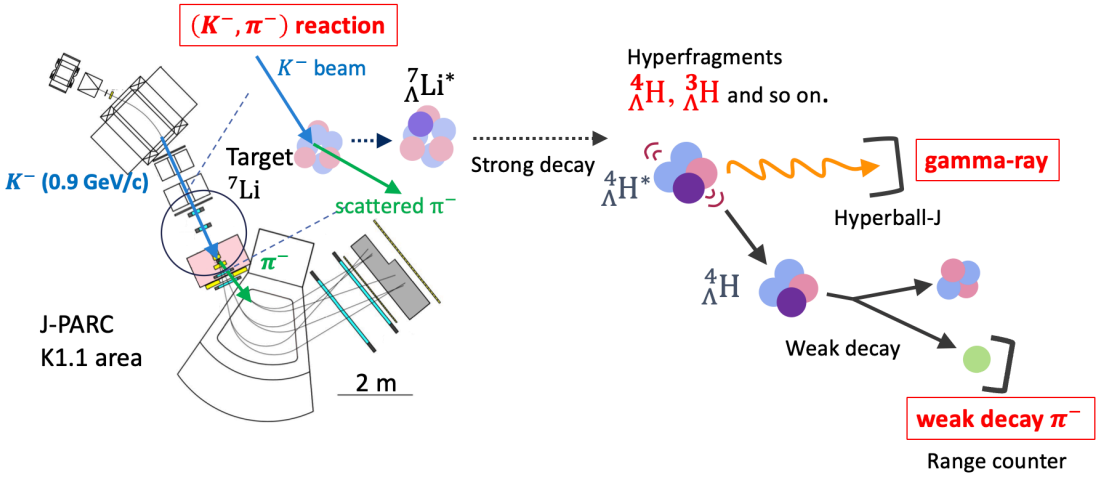

Figure 3.10: Schematic illustration showing triple coincidence measurement of (K^-, π^-) reaction and gamma-ray, as well as weak-decay π^- for the identification of secondary hypernuclei.

3.3.3 Data Acquisition

In this section, I explain the data acquisition system mainly related to the range counter system. Scintillation photons are read out at MPPCs both in TD and RC.

As briefly summarized in section 2.3, the data acquisition system is network-based (HD-DAQ) [44]. As data-taking Front-ends are distributed in the experimental area, information on a trigger or an event tag should be distributed to each Front-end. The Master Trigger Module (MTM) manages the trigger and the event tag. The Receiver Modules (RM) on each Front-end accept the information from MTM. The RM also transfers its Busy signal, and the MTM manages the Busy from all of the Front-ends. In each Front-end, the RM connects to all the modules for TDC or ADC on the same crate and distributes the trigger and the event tag to them via the crate bus, and RM also sends the sum of the Busy of all the modules to the MTM. The Event Builder (EB) collects the data taken in each Front-end, and it also collects the event tag and reconstructs the event.

In the circuit for data taking of the range counter system, an ASIC module for multi-channel MPPC readout (EASIROC) [48] is used. An ASIC board for the

EASIROC should be adapted to the HDDAQ system, that is, it is required that the board can receive the trigger and send the event tag or the Busy via the network.

EASIROC

Since the number of MPPCs used in the range counter system is large, we use the EASIROC board developed for MPPC multi-channel readout. EASIROC (Extended Analogue Silicon PM Integrated Read-Out Chip) is a multi-channel analog frontend ASIC for reading PPD (Pixelated Photon Detector) developed by OMEGA/IN2P3 [48]. One EASIROC chip can read 32 MPPCs and the EASIROC has basic functions such as a bias adjustment, a shaping amplifier, and a discriminator for each of 32 MPPCs. Figure 3.11 shows the overview of the EASIROC internal circuit.

◇ MPPC bias adjusment

The gain of the MPPC is sensitive even to fine bias differences. Therefore, although we apply the same bias of each MPPC to all the MPPCs, we need to adjust the bias on the lower voltage side using an input 8-bit DAC (InputDAC) on the EASIROC chip. Thanks to the InputDAC placed at the beginning of the input line, we can regulate the MPPC gain by changing the bias of each MPPC in the range from 0 to 4.5 V channel by channel.

◇ High gain and low gain

The input line is connected to two capacitors and the signal is divided into two parts; the high gain (HG) signal and the low gain (LG) signal. The capacitance ratio determines the amplification ratio of HG and LG, and the charge is divided with a ratio of 10:1 between HG and LG. PreAmp is placed after the capacitor, and the signal is amplified. Both low-gain and high-gain preamplifiers can be changed on 4 bits, allowing a voltage gain from 1 to 15 for LG and from 10 to 150 for HG. This is achieved by changing the capacitance of each PreAmp capacitor. EASIROC has a dynamic range from 160 fC to 320 pC, which corresponds to 1 p.e. to 2000 p.e.

◇ Fast shaper and slow shaper

The shapers follow the PreAmp sections. EASIROC has two built-in shapers: a fast shaper for time measurement and a slow shaper for charge measurement. The fast shaper is located only on the high-gain side and the slow shaper is on both the high gain and low gain.

◇ **Time measurement**

The signal is shaped with a peaking time (time from signal rise to peak) of about 15 ns with the fast shaper and becomes an input to the discriminator. The signal for time measurement and trigger is obtained from the discriminator. The threshold is common for all the 32 channels and is set by a 10-bit DAC which allows threshold tuning from 1.1 V to 2.4 V. The signal output after the discriminator is sent to TDC outside of EASIROC or used for a trigger of data taking.

◇ **Charge measurement**

In the slow shaper, the signal is shaped with a peaking time of about 50 ns. The peaking time is variable and can be set between 25 ns and 180 ns.

In order to help us to obtain ADC information, the EASIROC has a function for memorizing the wave height, not integrating total charge. One capacitor is placed after the slow shaper and holds the voltage at the time when the pulse reaches the peak. Since the maximum wave height is not automatically detected, EASIROC must be informed of the timing of the maximum wave height from outside. The logic signal to inform EASIROC of the timing is called a HOLD signal. The HOLD signal disconnects the switch, which is conductive when the logic is high and disconnected when the logic is low. The recorded analog voltage can be serially output from the analog output pin using a read register, and by connecting the pin to an external ADC (Analog to Digital Converter), we can measure the charge by EASIROC.

◇ **Slow Control**

InputDAC value, PreAmp gain, Slow Shaper time constant, and discriminator threshold setting can be rewritten externally by SlowControl.

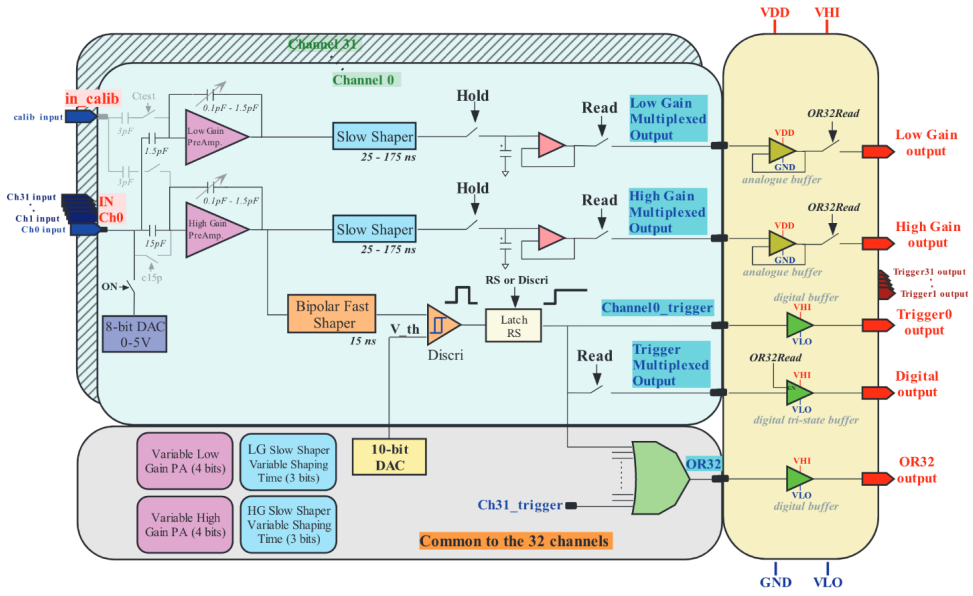

Figure 3.11: Overview of the EASIROC internal circuit[48].

EASIROC boards

The VME-EASIROC board is developed mainly for the Time-Digital-Convertor and the Analog-Digital-Convertor of MPPC signals, as well as data acquisition or transfer to the Receiver Module (Fig. 3.12). Since a EASIROC can read 32 MPPCs with one chip, the VME-EASIROC board is equipped with two chips, and then the board can read 64 MPPCs. The EASIROC chip is connected to FPGA. The FPGA is responsible for controlling the ASIC and taking the ADC or TDC data. The board can accept the trigger and the hold timing via KEK-VME J0 bus and transfer the data to the Front-end with the SiTCP protocol via the Ethernet. All the VME-EASIROC boards are connected to a Receiver Module, GP-IO, which accepts the trigger and the event tag from MTM and distributes them to the EASIROC boards on the local network via the J0 bus.

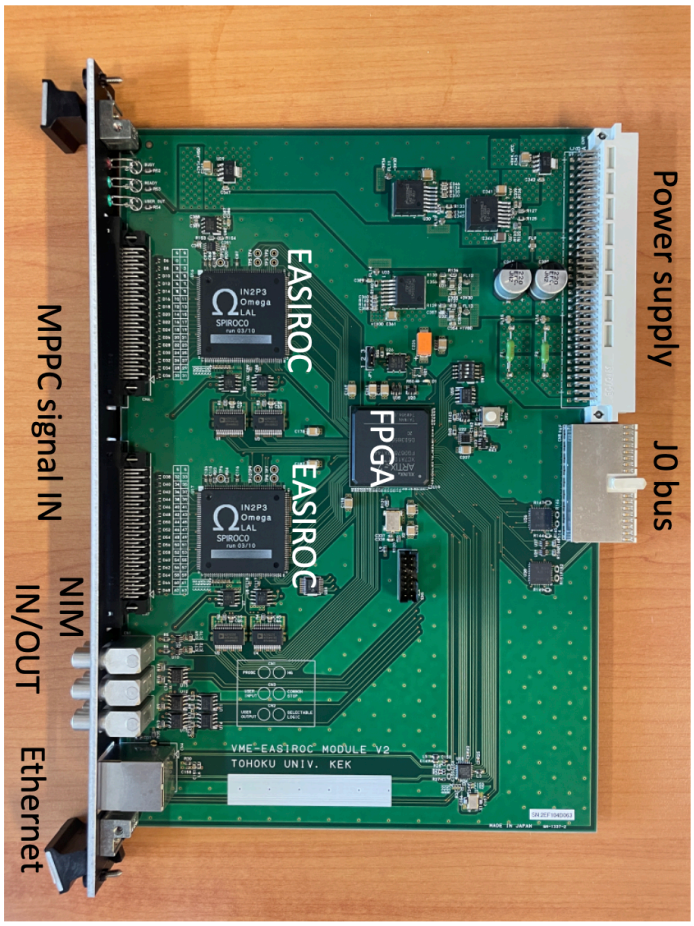

Figure 3.12: VME-EASIROC board developed mainly for the Time-Digital-Convertor and the Analog-Digital-Convertor of MPPC signals, as well as data acquisition and their transfer to the Receiver Module. The board can accept the trigger and the hold timing via KEK-VME J0 bus and transfer the data to the Front-end with the SiTCP protocol via the Ethernet. All the VME-EASIROC boards are connected to a Receiver Module.

Chapter 4

Evaluation Experiment of Prototype Range Counter

I fabricated a prototype range counter made of 8 layers of a 6 mm-thick plastic scintillator slab. The total thickness of the prototype is one-third of that of the range counter used for the E63 experiment. I conducted an experiment at the downstream end of the J-PARC K1.8 beam line to test the prototype and evaluate its performance. As a result, I confirmed that the prototype satisfies the requirements to separate the pions in the E63 experiment. In this chapter, I explain the details of the prototype and the experiment.

4.1 Configuration of Prototype

I fabricated a prototype composed only of a range counter except for a tracking detector. The components of the prototype range counter (the model number of plastic scintillators, wavelength-shifting fibers, and MPPC) are the same as the range counter for the E63 experiment (henceforth, called E63 Range Counter) described in Sect. 3.3. The only difference from the full size of the range counter is the total thickness of the prototype; the number of layers in the prototype is only one-third of that of the E63 Range Counter.

4.2 Fabrication of Prototype

The method and process of the fabrication are summarized in this section.

◇ **Embed fibers in plastic scintillator**

The plastic scintillator slab, cut to the size needed for the range detector, had its

surface polished and grooves dug on the top and bottom surfaces of it. The grooves are semi-cylindrical with a diameter of 1 mm. I embedded a wavelength-shifting fiber in the groove carved into the scintillator slab and fixed it with optical cement (EJ-500)(Fig. 4.1). I wiped off the excess cement, being careful not to let any dirt or dust adhere to the cement. In spite of careful work, the surface became a little dirty. After the optical cement hardened, I wrapped the slab with Teflon sheet all over the scintillator slab, carefully not to tear or wrinkle the Teflon. I fabricated 8 layers of that and the total thickness of the Teflon sheets of 8 layers is less than 1.6 mm.

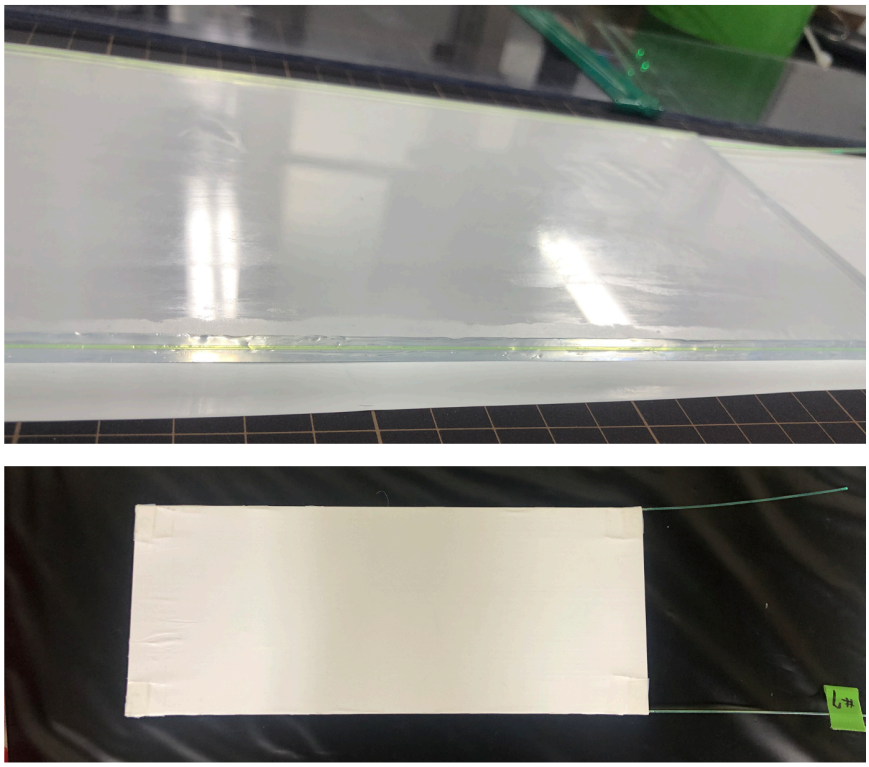

Figure 4.1: Process of embedding wavelength shifting fibers in a groove on the scintillator slab, fixing them with optical cement (top) and wrapping the slab with Teflon sheet (bottom).

◇ **Fix scintillator slabs with aluminum frame**

I fixed eight scintillator slabs together with an aluminum frame (Fig. 4.2). I also installed an aluminum board for mounting a circuit board with MPPCs (MPPC readout board) and guiding the fibers to the MPPCs. At that time, the design was such that there was almost no extra space in the holes for the fibers to pass through smoothly, and I worked for a long time to pass a total of 16 fibers through the holes on the aluminum board little by little, taking great care not to crack or damage the

fibers.

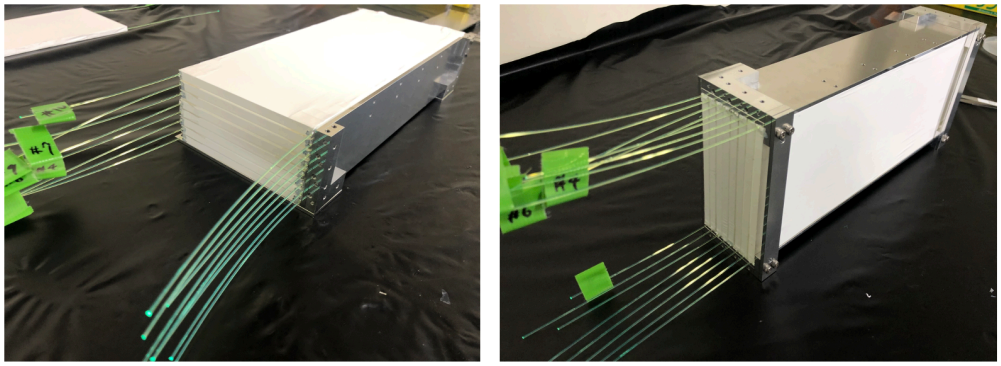

Figure 4.2: Fixing scintillators with aluminum frame.

◇ **Polish the readout surface of fibers**

After threading the fibers through the holes and fixing the aluminum board, I fixed the fibers with optical cement. As shown in Fig. 4.3, the fiber was further fixed with epoxy resin in order to polish the cut end of the fibers without breaking and damaging them. Then, I sanded the cut end of the fiber and polished it. I put a black rubber sheet on the aluminum board to prevent crosstalk between the fibers as shown in Fig.4.4 and installed the MPPC readout board (Fig. 4.5) on it.

◇ **MPPC readout board for the prototype**

I designed the MPPC readout board. The circuit is shown in Fig. 4.6 and the board design is shown in Fig. 4.7. It is made of a two-layered circuit, with layer 1 (front side), L1, used for mounting components of cable connectors as well as capacitors and resistors and for mounting HV lines, and with layer 2 (back side), L2, used for mounting SiPMs and the signal lines.

The fabrication of the prototype range counter was completed as shown in Fig.4.8.

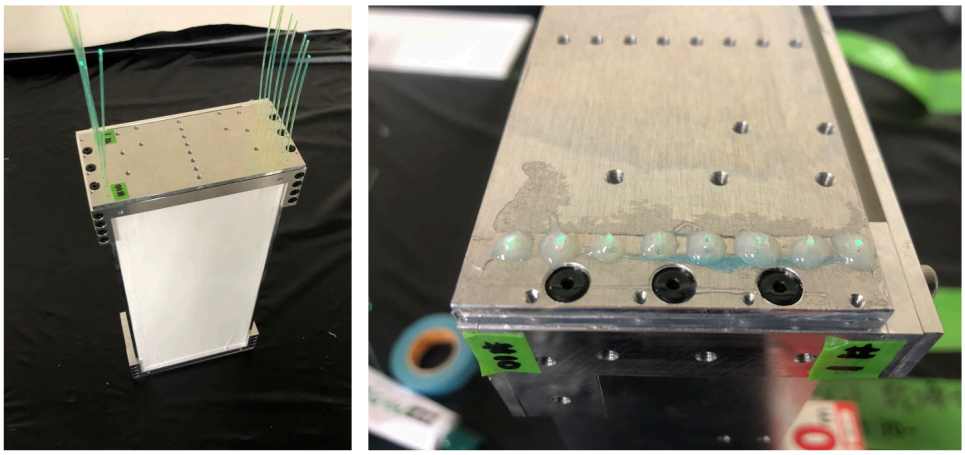

Figure 4.3: Polish the readout surface of fibers.

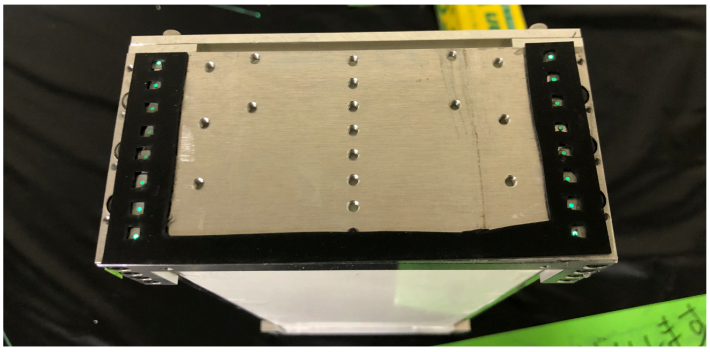

Figure 4.4: Black rubber sheet put on the aluminum board to prevent crosstalk between the fibers

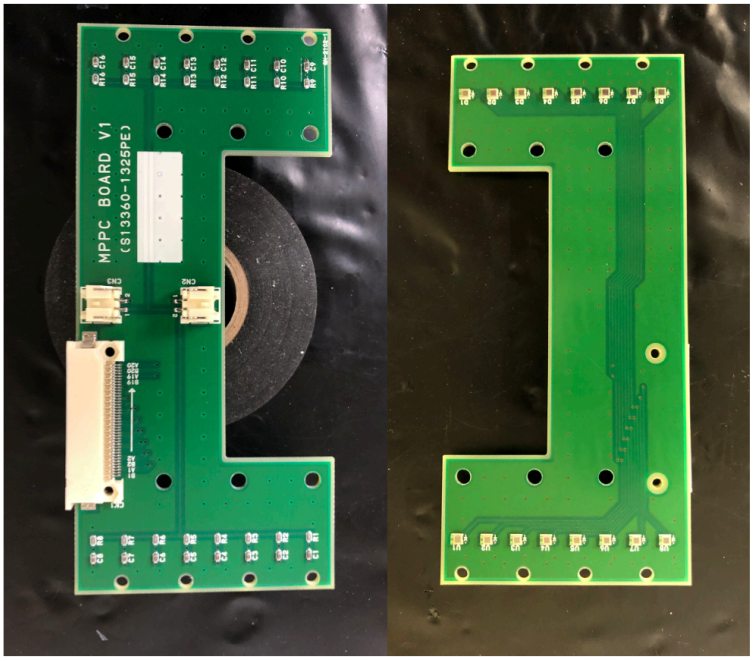

Figure 4.5: MPPC readout board for the prototype. It is made of a two-layered circuit, with layer 1 (front side), L1, used for mounting components of cable connectors as well as capacitors and resistors and for mounting HV lines and layer 2 (back side), L2, used for mounting SiPM and the signal lines.

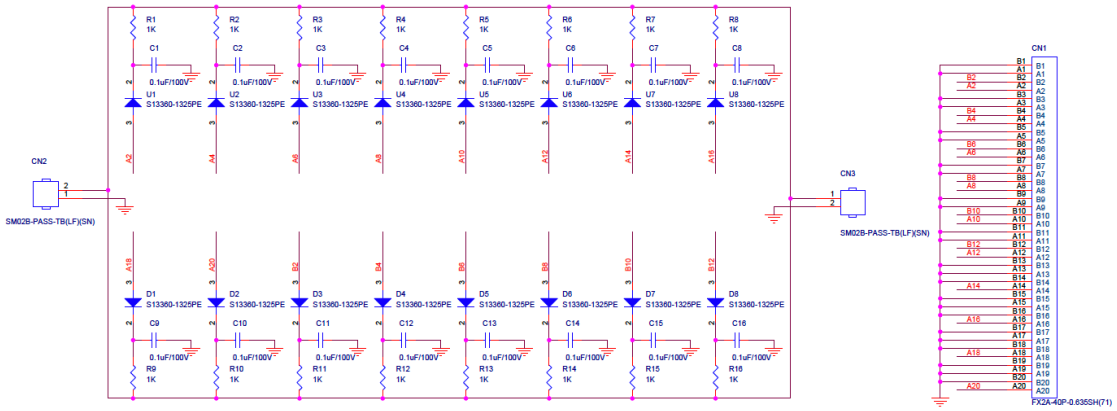

Figure 4.6: Circuit of the MPPC readout board for the prototype. This circuit is made of 16 channels of MPPC. Each channel is composed of MPPC (S13360-1325PE), capacitor ($0.1\,\mu$F), and resistor ($1\,\mathrm{k}\Omega$).

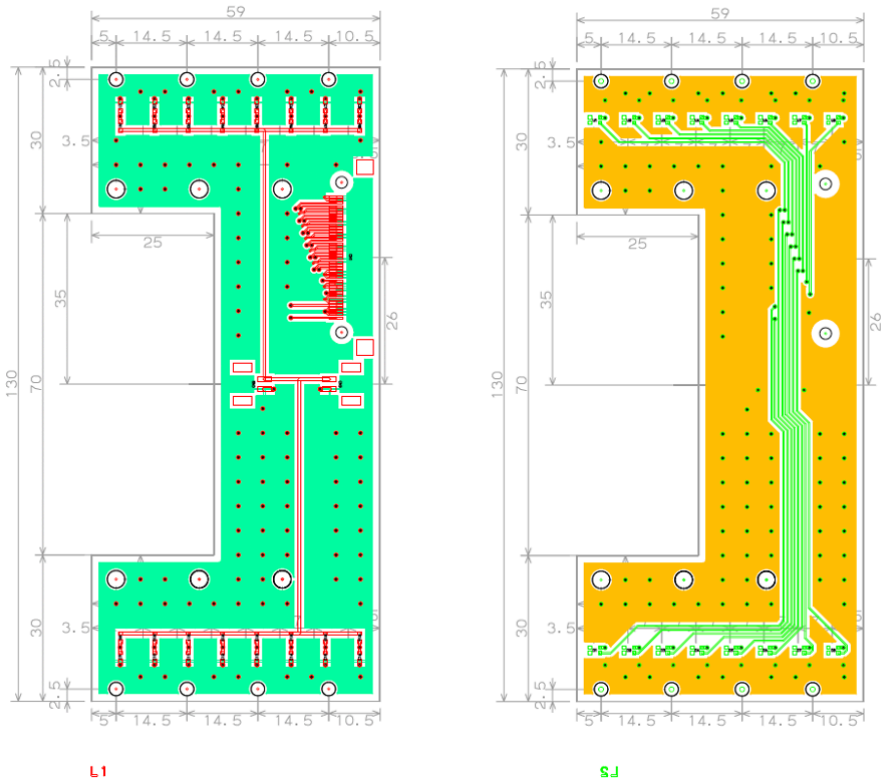

Figure 4.7: Board design of the MPPC readout board for the prototype. Left: L1 (front side) used for mounting components of cable connectors, capacitors, and resistors and for mounting HV lines. The red line represents the HV line, and the green area represents the ground. Right: L2 (back side) is used for mounting SiPMs and the signal lines.

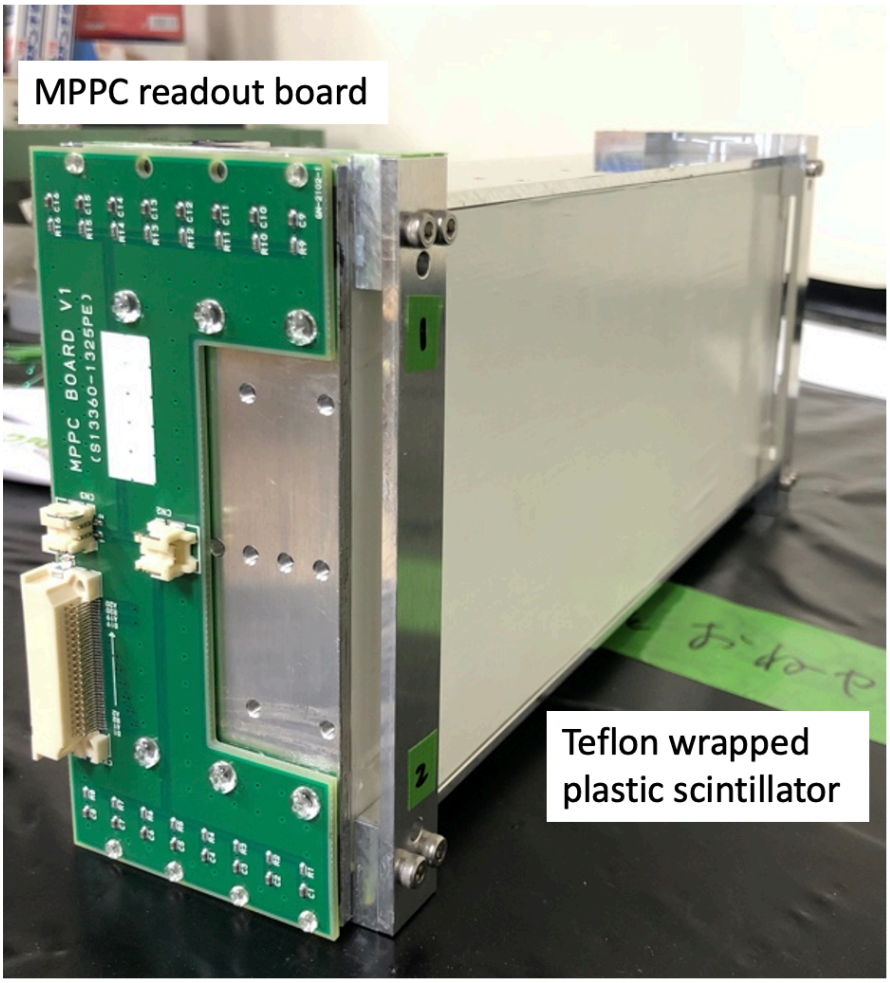

Figure 4.8: Prototype range counter

4.3 Evaluation Experiment

I conducted an experiment to evaluate the prototype range counter. The purposes of the experiment are: (1) to check if the signal is read out correctly and the number

of photons is sufficient, (2) to confirm it possible to identify the pion stop events in the prototype, and finally (3) to test if the prototype can separate the pions from ${}^{3}_{\Lambda}\mathrm{H}$ and ${}^{4}_{\Lambda}\mathrm{H}$.

1. Check the operation of the readout

I adopted the readout method using wavelength-shifting fibers and MPPCs as described in Sect. 3.3. Scintillation photons are converted and transported in the wavelength-shifting fibers embedded in the two sides of the scintillator slab, and read out with SiPMs. First of all, it is necessary to confirm whether this reading method is properly working without any defects. As described in Sect. 3.3.1, I take the data not only of hit information but also of the ADC information from each MPPC, and if I acquire enough photons with MPPC when pions are injected and stop in the range counter, I should observe the energy loss in each layer follows a Bragg curve.

2. Identify the pion stop events in the prototype and investigate effects of the pion interaction

As a Monte Carlo simulation suggests in Sect. 3.2, pions stop in the range counter with larger energy loss than the cases without hadronic interaction with some probability. The strong interaction effect is hard to calculate precisely in a low energy region and experimental data is limited, and therefore, the interaction in simulations could be different from the real interaction. Therefore, I should study whether the energy loss in each layer of the range counter agrees with the simulated one or not because, if not, it becomes difficult to determine the stop layer. In addition, I should also confirm how often pions lose their energy via strong interaction in the range counter.

3. Test if the prototype can separate the pions from ${}^{3}_{\Lambda}\mathrm{H}$ and ${}^{4}_{\Lambda}\mathrm{H}$

In order to identify the hypernuclei of ${}^{4}_{\Lambda}\mathrm{H}$ and ${}^{3}_{\Lambda}\mathrm{H}$, the range counter should have a kinetic energy resolution less than 3 MeV as explained in Sect. 3.2. In the test experiment, the resolution should be also investigated.

4.3.1 J-PARC K1.8 Beamline

I conducted the experiment at the J-PARC K1.8 beamline where pions were available as a beam. The K1.8 beamline is optimized for Ξ hyperon production. The maximum momentum of the supplied K^- beam is 2.0 GeV/c. The production cross section of Ξ hyperons is largest at 1.8 GeV/c [51]. By using the produced hyper-

ons, it is possible to study hypernuclei with S = −2 such as double Λ hypernuclei and Ξ hypernuclei, in addition to single Λ/Σ hypernuclei. The K1.8 beamline is equipped with two stages of electrostatic separator (ESS) that separates particles according to their velocity among various secondary beam particles produced at an upstream production target and selected for their momenta with bending magnets. Since the world-highest intensity of K^- beam with up to around 5 M/spill (spill = 2.0 seconds) is available, I use it for systematic research of hypernuclei via missing-mass spectroscopy and gamma-ray spectroscopy, and of YN two-body interaction via hyperon-nucleon scattering with high statistics.

As the J-PARC can provide us with a high-intensity hadron beam, it is a suitable place to test the prototype using a pion beam. However, as the beamtime in J-PARC is very limited, I cannot obtain a beam time only for testing a detector. In this situation, a prototype test experiment was conducted in the most downstream part of the K1.8 experimental area in parallel with an experiment for searching for H-dibaryon (J-PARC E42). In this experiment, H-dibaryon is produced via the (K^-, K^+) reaction on a carbon (diamond) target. Momentum measurement and particle identification of the beam K^- and the scattered K^+ are performed by K1.8 beamline spectrometer and a spectrometer for scattered particle (KURAMA) as shown in Fig. 4.9.

4.3.2 Experimental Setup

In the downstream part of the E42 setup, I installed detectors and took data with an independent data acquisition system of the E42 experiment. Pions with a momentum of 0.33 GeV/c decay in 20 m, and a particle at the downstream may be different from the original particle at the upstream. Even though I could monitor what particles were transported to the downstream part, I could not identify each particle entering the prototype. I should identify the particles and measure their velocity with my detectors just before the prototype.

The experimental setup is given in Fig. 4.9, 4.10, 4.11, and 4.12. I measured the time-of-flight with TOF counters (T1 and T2) because particles fly with various velocities. Both T1 and T2 are plastic hodoscopes of 5 segments. From the time of flight, I obtained the velocity of the particle before entering the prototype range counter. The segment number assignment in Fig. 4.10 is used in the following analysis and discussion. The basic information on T1 and T2 is summarized in Table 4.1.

I took data with three conditions: (1) 1.8 GeV/c π^- beam run, (2) 300 MeV/c π^- beam run, and (3) scattered proton run as summarized in Table 4.2. In the runs

(1) and (2), there was no target in the E42 experiment, and the KURAMA magnet was turned off. Therefore, the incident particle was mainly a negatively-charged pion coming directly through the K1.8 spectrometer as the dotted arrow shown in Fig. 4.9. These pion beams in (1) and (2) had a momentum of 1.8 GeV/c and 300 MeV/c, respectively. The former was used for the calibration of the prototype and the latter was for the study of the performance of the prototype with low momentum pions stopped inside.

While beam particles were used in the runs (1) and (2), scattered particles were used in the run (3). There was a diamond target for the E42 experiment, and the KURAMA magnet was turned on. Positively-charged particles like protons and pions (and muons) were produced in the reaction between the diamond and K^- beams, and they were bent by the KURAMA magnet to the downstream part. I mainly used the scattered protons with momenta around 600 MeV/c. The setup was changed from the runs (1) and (2) as shown in Fig. 4.9.

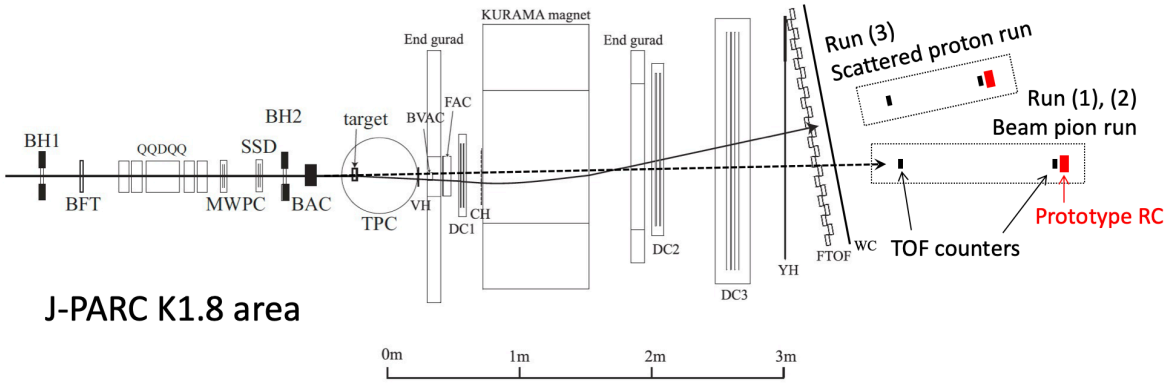

Figure 4.9: Setup of the H dibaryon search experiment at K1.8 beam line (J-PARC E42), with which a test experiment for the prototype was performed in parallel. The setup for the prototype was changed two ways for beam pion runs and a scattered proton run.

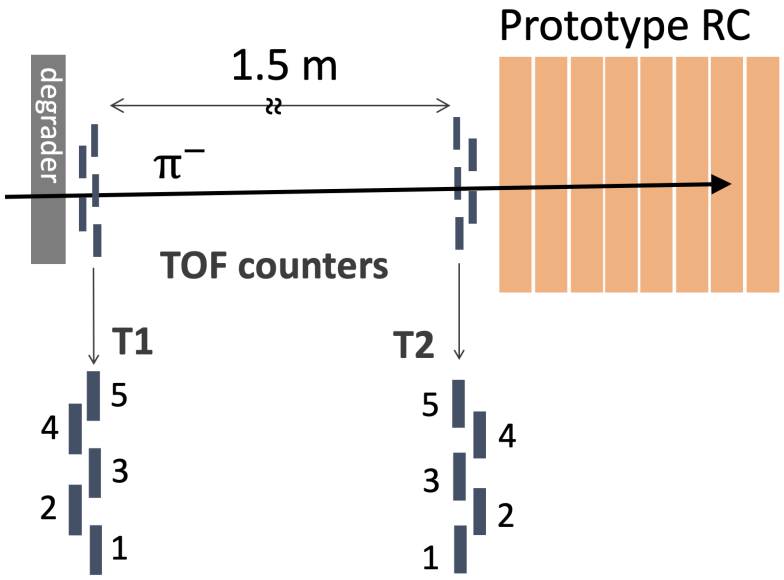

Figure 4.10: Experimental setup. The time-of-flight was measured with a TOF counter (T1 and T2). Both T1 and T2 are plastic hodoscopes of 5 segments. From the time of flight, I obtained the kinetic energy of the particle before entering the prototype range counter (Incident energy). I used a degrader for stopping pions in the prototype, and the distance between T1 and T2 was about 1.5 m. This figure shows the setup for the pion runs, (1) and (2). In the scattered proton run (3), I did not use the degrader, and the distance between T1 and T2 was about 1.0 m.

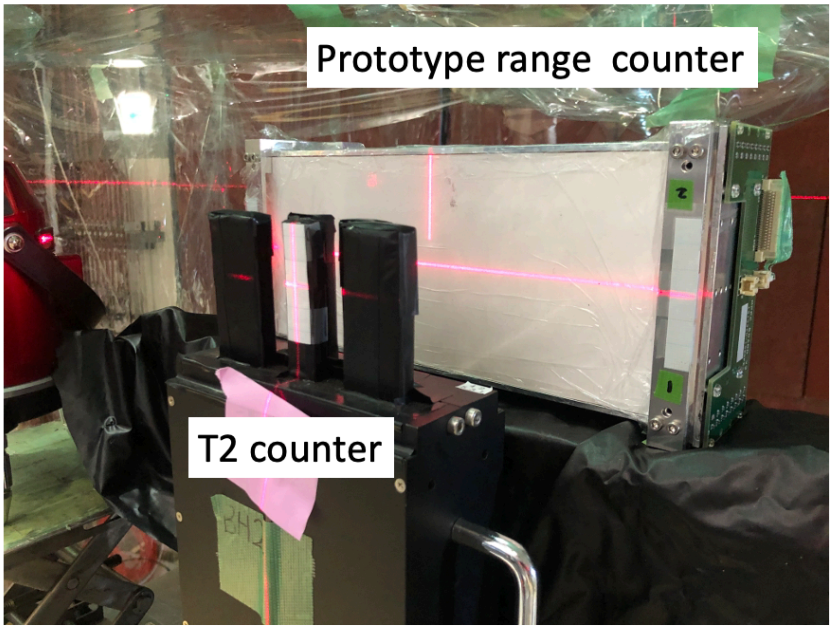

Figure 4.11: Experimental setup of the prototype and T2 counter viewed from the upstream. The position of the prototype and TOF counters was determined by using cross line laser levels.

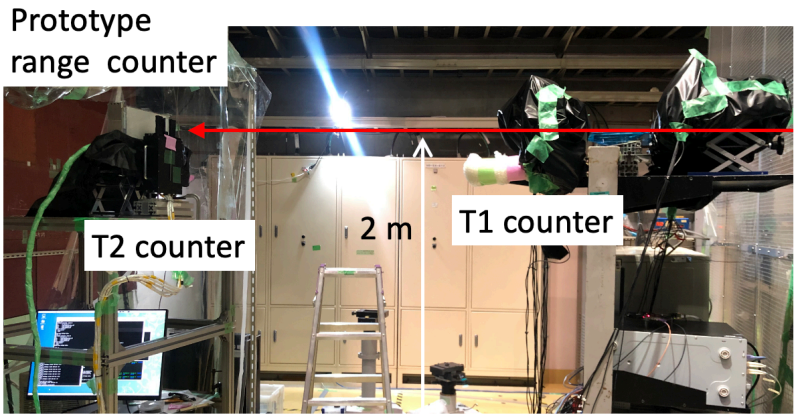

Figure 4.12: Experimental setup of the prototype and TOF counters viewed from the side for the beam pion run.

Table 4.1: Information on T1 and T2

	T1	T2
Number of segments	5	5
segment size (H × W × T [mm^3])	20 × 50 × 5	50 × 20 × 5
readout	MPPC	PMT
	both-side	one-side

Table 4.2: Data summary

	(1)	(2)	(3)
Particle	beam π^-	beam π^-	scattered proton
Momentum	1.8 GeV/c	0.3 GeV/c	$\sim$ 0.6 GeV/c
E42 target	no target	no target	Diamond
Degrader	With degrader	With degrader	Without degrader
Material	Iron	Iron	
Thickness [g/cm^2]	19, 24, 28	19, 24, 28	
KURAMA magnet	OFF	OFF	ON
Number of triggered events	80K	400K	18M
Distance b/w T1 and T2	1.4 - 1.5 m	1.4 - 1.5 m	1.0 - 1.1 m

In the experiment (2), the pions of about 300 MeV/c were degraded into less than about 110 MeV/c in a degrader so that the pion would stop in the prototype. Three iron blocks with different thicknesses of 19, 24, and 28 g/cm^2 were placed next to each other as the degrader. The pion flies with various velocities before the degrader and also between T1 and T2.

4.3.3 Data Acquisition

The data acquisition system is independent of the one for the main experiment, E42. The data-acquisition circuit is given in Fig. 4.13. I took data with a coincidence trigger of both T1 and T2 (L1 trigger). Fan In/Fan Out (FI/FO) separated the L1 trigger in n stop.

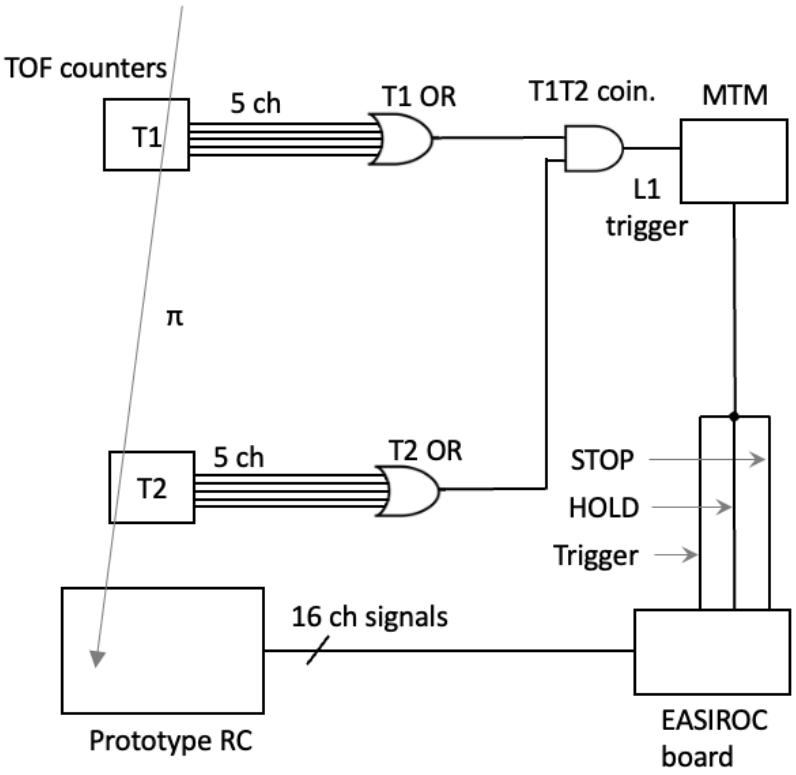

Figure 4.13: Data acquisition circuit in the test experiment for the prototype. The data was taken with the T1-T2 coincidence trigger (L1 trigger). The L1 trigger was separated into three signals: Trigger, HOLD, and Common stop (STOP) for data taking in the EASIROC.

4.4 Analysis

4.4.1 Beam Particle

The momentum of the beam particle was measured by the K1.8 spectrometer (Fig. 4.14) event by event, but I cannot use the information because the data acquisition system is separated from the DAQ system for testing the prototype. Therefore, the information was used just for monitoring the beam. The momentum spread in Fig. 4.14 is not caused by the detector resolution in the K1.8 beam spectrometer but by momentum distribution determined by the K1.8 beam line (the momentum bite). Figure 4.15 shows the Time-Of-Flight measured by two hodoscopes BH1 and BH2 (called BTOF) for electron, μ^-, and π^-. The flight path was 10.044 m. The total number of electrons and that of pions in the (2) run were both 3.3×10^7, and that of muons was 3.7×10^6. These numbers were counted by BH1 and BH2, but all the particles did not reach the prototype. The momentum of electrons, muons, and pions was 0.303 GeV/c from the BTOF.

Assuming that the lifetimes of pion and muon are 22 nsec and 2.2 μsec, respectively, and both momentuma are 0.303 GeV/c, the decay rate of pions in the distance of 5 m from BH2 to the prototype is estimated to be 23%. Assuming that only 23% of the total number of pions decayed to muons at BH2 (3.3×10^7 in total), the number of pions which reached the prototype is extimated to be 2.5×10^7 and that of muons is 1.1×10^7. In this analysis, the fraction of muons mixed with the pion beam is less than 31% because the TOF selection was applied and the event selection was also performed.

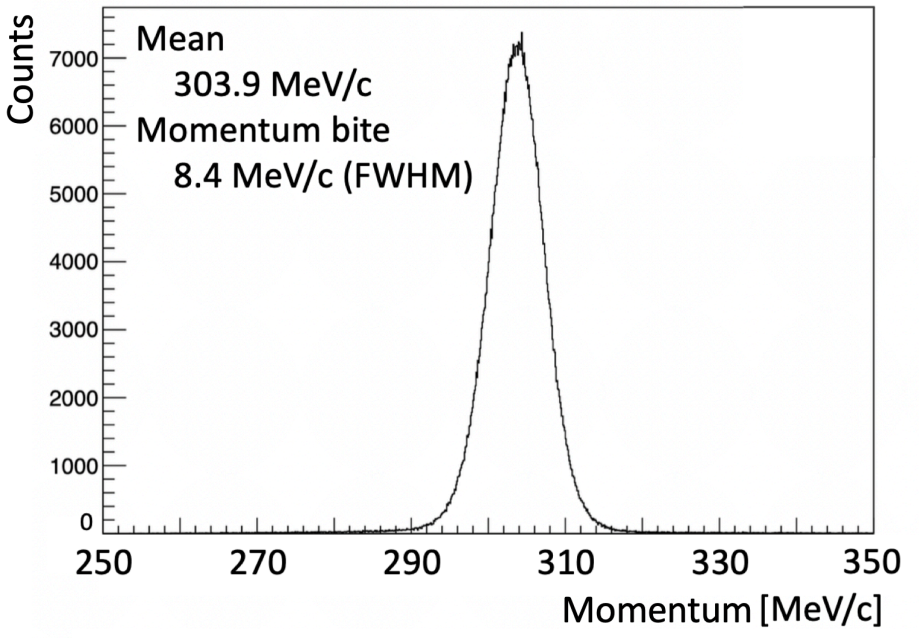

Figure 4.14: Distribution of beam momentum measured by the K1.8 beam spectrometer in the low momentum pion run.

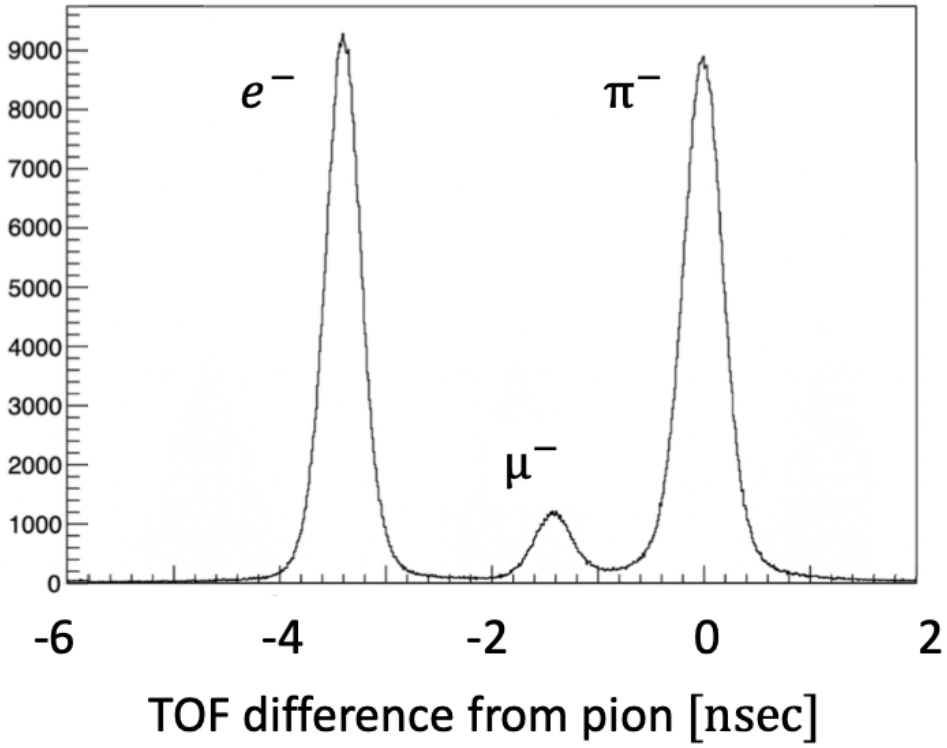

Figure 4.15: Time of flight between BH1 and BH2 in the K1.8 beamline. The TOF was a relative value with respect to the pions. Kaon and antiprotons were too slow and cannot be seen in this figure.

4.4.2 Energy Calibration

I do not have to accurately measure the energy loss in the counter but need to acquire the pulse height information from each MPPC in order to know the energy loss in each layer. Minimum-ionizing particles (MIP) lose an energy of 2 MeV per 10 mm in plastic scintillator until the particle was degraded to a velocity much slower than the speed of light and regarded as not a MIP.

The ADC data of the prototype range counter was calibrated using the data of 1.8 GeV/c π^- run. Two values in the ADC distribution of each layer were used for the enegy calibration. One is a MIP peak whose most probable value corresponds to the energy loss of 1.2 MeV as shown in Fig. 4.16. The other is a pedestal peak (zero energy peak). Hereafter, "mip" is used as a unit of energy corresponding to 1.2 MeV. The MIP peak appeared when the data was taken by the trigger of T1 and T2 coincidence and the pedestal peak appeared when the data was taken mainly by other triggers.

As a result of the calibration using these two values, the two-dimensional distribution as shown in Fig. 4.17 was obtained. The typical photon number was about 15 photons for one mip.

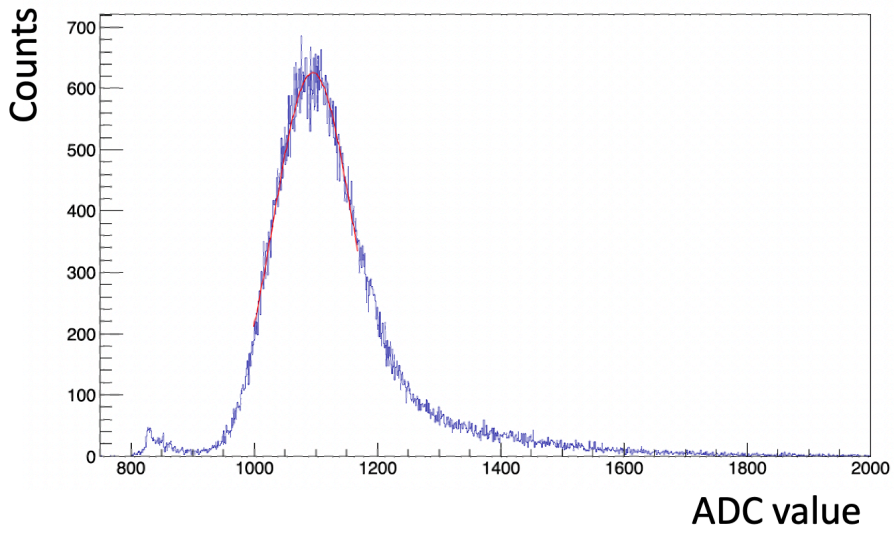

Figure 4.16: ADC distribution of layer number #2. The horizontal axis shows the ADC value and the vertical one shows the counts. The most probable value of the MIP peak corresponds to 1.2 MeV energy deposit.

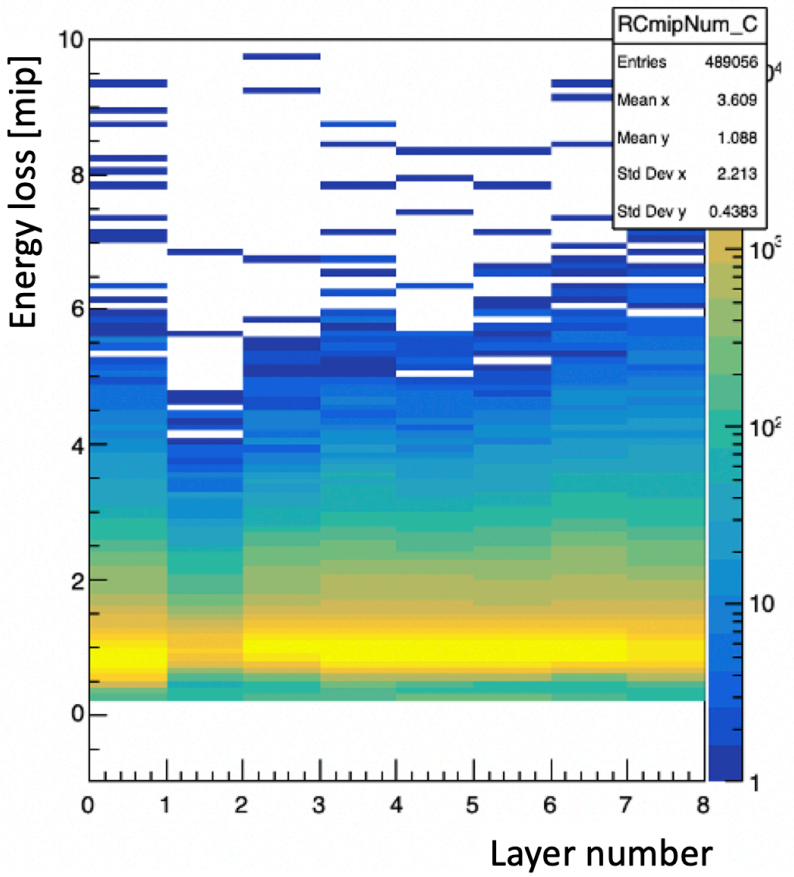

Figure 4.17: Two-dimensional distribution of layer number and energy loss. The energy is calibrated by the ADC values obtained in the 1.8 GeV/c π^- run.

4.4.3 Slewing Correction of TDC

In this section, I explain the analysis of the time of flight. Information on the timing when a particle enters a counter is obtained naively from the time when the pulse crosses a certain threshold. However, the pulse height fluctuates for each event depending on the energy loss of the particle loses in the counter as well as the fluctuation of the number of photons detected by the photo sensor, and a difference in the pulse height leads to a difference in the rise time of the signal, and finally leads to a difference in the TDC data. In other words, even if two particles entered a counter at the same time, we would obtain different timings when the two particles give different pulse heights. Therefore, it is necessary to correct the timing obtained directly from the TDC module into the true timing. This correction is called slewing correction and is usually done using TDC values and either ADC (pulse height) or

QDC (total charge) values.

Figure 4.18 shows an example of the slewing correction for the 1.8 GeV/c π^- run for the combination of T1 seg. 5 and T2 seg. 2. I took QDC values of the TOF counters called Q_{T1}, Q_{T2} and TDC values T_{T1}, T_{T2}, where the Q_{T1} and the T_{T1} are mean values of the left and right readouts of the T1 segment. The time difference (ΔT) in Fig. 4.18 is defined as $C_2 \cdot T_{T2} - C_1 \cdot T_{T1}$, where C_1 and C_2 are TDC calibration parameters. The parameters C_1 and C_2 were obtained channel by channel with a Time Calibrator module, CAEN V775. The C_1 and C_2 values determined for each TDC channel were distributed in $0.032 - 0.035$ nsec. The corrected Time difference (ΔT_{corr}) in Fig. 4.18 is defined as

$$\Delta T_{corr} = C_2 \cdot T_{T2} - C_1 \cdot T_{T1} - P_1/\sqrt{Q_{T1}} - P_2/\sqrt{Q_{T2}} - T_0,$$

where the P_1, P_2, and T_0 are correction parameters. Figure 4.18 left shows a two-dimensional distribution of $1/\sqrt{Q_{T1}}$ (horizontal) and Time difference ΔT (vertical) with a fitted function (red line). As a result of the fitting, the P_1 value was obtained. After the correction with respect to the Q_{T2} in the same way as Q_{T1}, the P_2 and T_0 values were obtained. Figure 4.18 right shows a distribution of $1/\sqrt{Q_{T1}}$ and the time difference ΔT_{corr} after the corrections concerning Q_{T1} and Q_{T2}.

Figure 4.19 shows the TOF distribution before and after the slewing correction for the combination of T1 seg. 5 and T2 seg. 2 obtained by projecting the distributions to the vertical axis in Fig. 4.18. The horizontal axis in Fig. 4.19 represents the TOF difference from the $\beta = 1$ particle, and the peak is located at 0 nsec because 1.8 GeV/c π^- is regarded as a $\beta = 1$ particle. By the slewing correction, the TOF resolution was improved from 250 ps to 160 ps. The improved TOF resolutions for all the combinations of the segments of T1 and T2 are summarized in Table 4.3. The slewing corrections for 300 MeV/c π^- and scattered protons were done also using the parameters obtained in the correction for 1.8 GeV/c π^-.

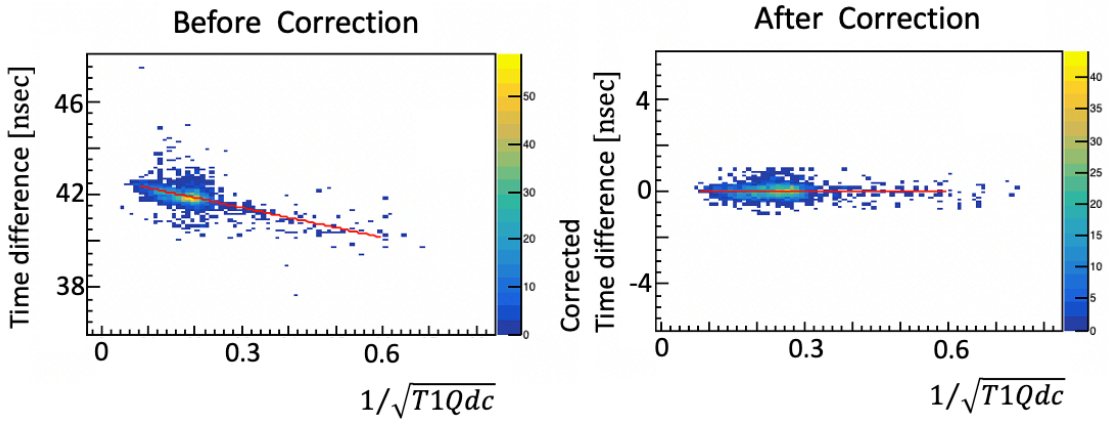

Figure 4.18: Time difference distribution with respect to $1/\sqrt{Q_{T1}}$ before/after slewing correction for the combination of T1 seg.1 and T2 seg.2. Left: Two-dimensional distribution of $1/\sqrt{Q_{T1}}$ (horizontal) and Time difference ΔT (vertical) with a fitted function (red line). Right: Distribution ΔT_{corr} after the corrections concerning Q_{T1} and Q_{T2}.

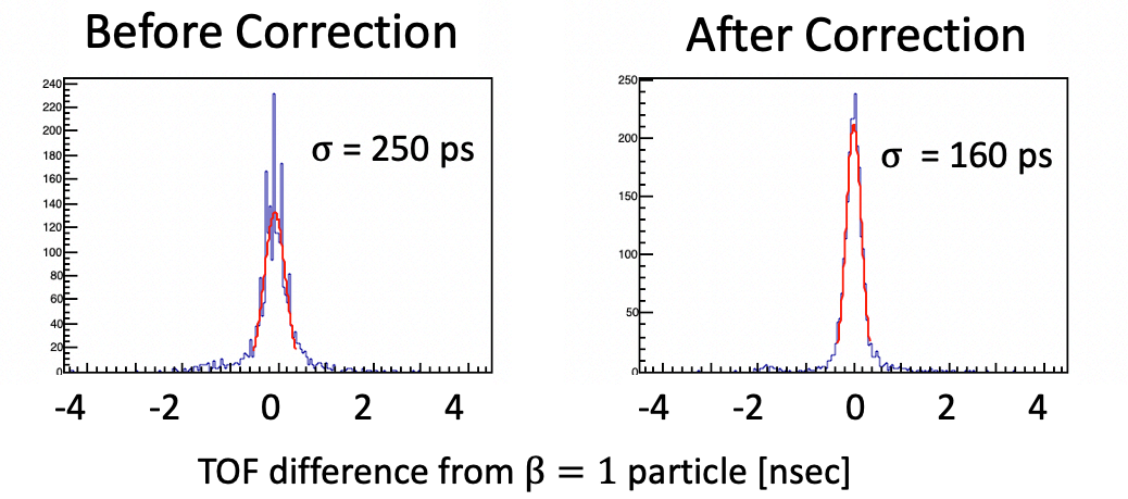

Figure 4.19: TOF difference from $\beta = 1$ particles before and after the slewing correction for the combination of T1 seg. 5 and T2 seg. 2 in the run of 1.8 GeV/c π^-. The horizontal axis represents the TOF difference from $\beta = 1$ particles.

Table 4.3: The TOF resolution after the slewing correction for all the combinations of the segments of T1 and T2 [psec]

segments		T1				
		1	2	3	4	5
T2	1	143	132	169	167	197
	2	164	116	120	154	160
	3	116	121	105	134	203
	4	151	136	116	140	225
	5	177	161	131	140	209

4.4.4 Stop Event Selection

In this section and the following sections, results are shown and considerations of them are given.

Low momentum pions are selected by applying a cut to the obtained TOF difference distribution in Fig. 4.20. The origin of the horizontal axis was adjusted so that the peak made of the distribution of $\beta = 1$ electrons is located at 0 nsec. The distribution is simulated with Monte Carlo method taking into account strong interaction of pion in matter. In this simulation, muons and pions with a ratio of 1 : 10 are injected with a momentum of 0.290 GeV/c into a setup consisting of the WC as well as the degrader, the TOF counters, and the prototype as in the test experiment. Particles are injected into the setup just before the WC which mainly affects the number and velocity of the particles. As a result, the ratio of the number of muons and pions reaching the prototype is estimated to be 10 : 1, and, in other words, the number of pions decreases to 1/100 of the initial number. Assuming the same time resolution as that of the TOF counters, muons are distributed about 1 nsec slower than the $\beta = 1$ particles, and pions are distributed in the region slower than 2 nsec, which is consistent with the distribution shown in Fig. 4.20.

I selected slower particles than the $\beta = 1$ peak, and the selected area is shown as a red band, where pions can be stopped at the prototype range counter, corresponding to less than 38 MeV in terms of kinetic energy, 0.62 in terms of beta, and 109 MeV/c in terms of momentum. When I plotted the energy deposit in each layer of the range counter for the selected events, I observed Bragg curves as shown in Fig. 4.21. These events are defined as stop events in the following discussion. In the events selected by the TOF cut, a particle continues losing the energy to the Nth layer, where N is less than 8, and the energy loss is less than 0.5 mip in each layer from (N+1)th to the 8th. Such an event is defined as the event where the particle

stopped in the Nth layer. I confirmed that 350 pions stopped in the prototype.

For the case of the scattered proton run, Fig. 4.22 and Fig. 4.23 show the TOF difference distribution and the energy deposit in each layer of the range counter for selected events.

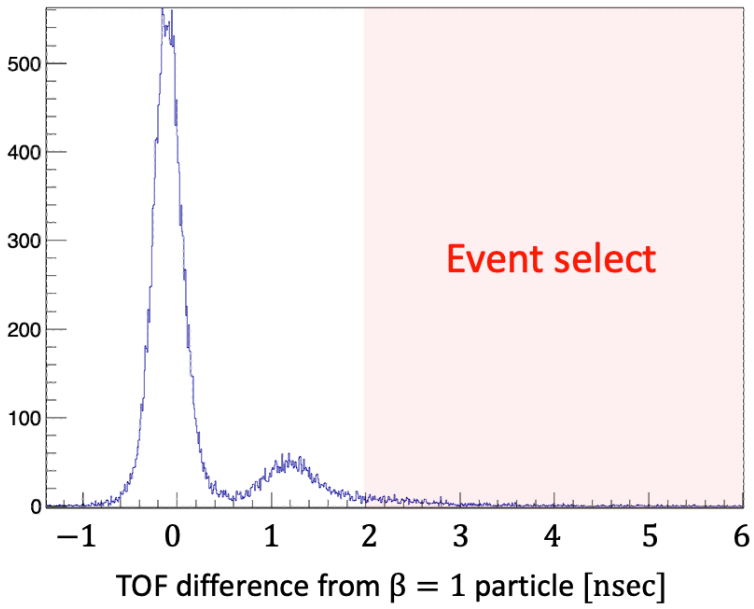

Figure 4.20: Distribution of the TOF(T1-T2) (difference from $\beta = 1$ particles) for pions for all the combinations of T1 and T2. The peak located at 0 nsec is the distribution of $\beta = 1$ electrons. The red band shows the region for low momentum pions selected as the stopping events in the prototype.

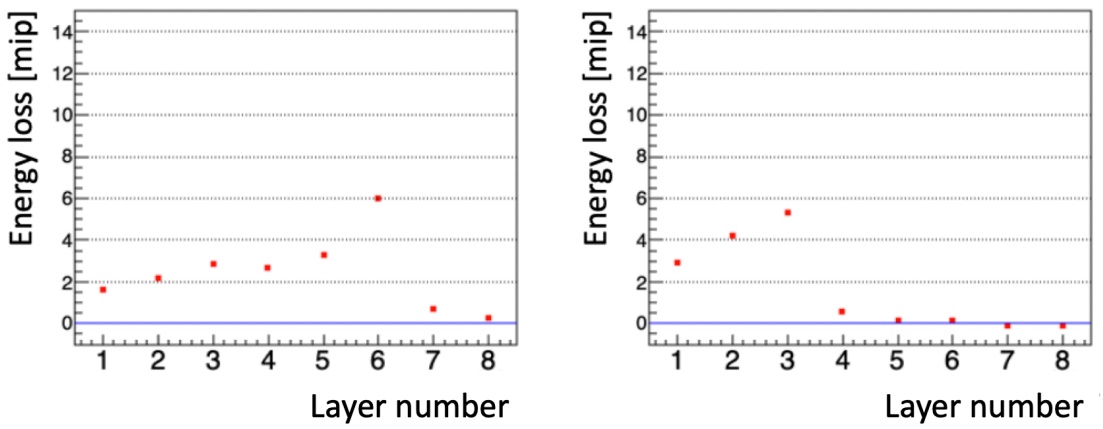

Figure 4.21: Energy deposit in each layer for typical stop events of pions.

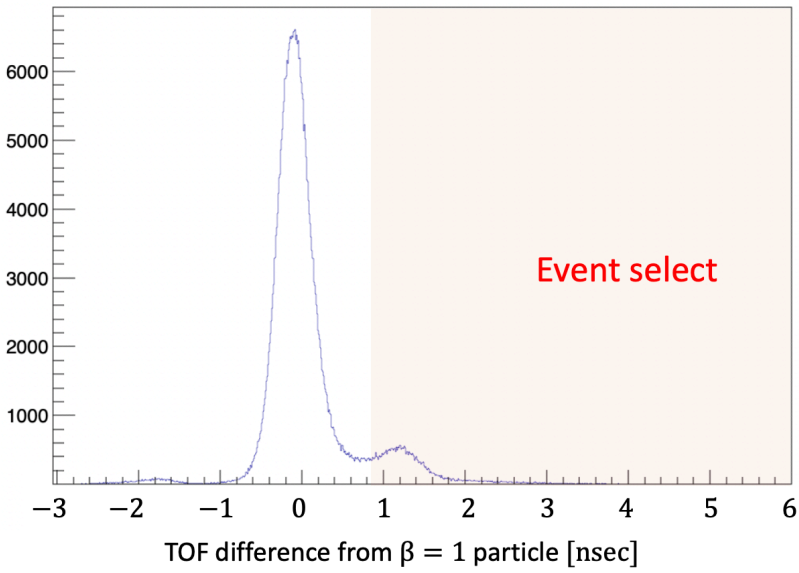

Figure 4.22: Distribution of the TOF(T1-T2) (difference from MIP) for protons. The red band shows the region for selection.

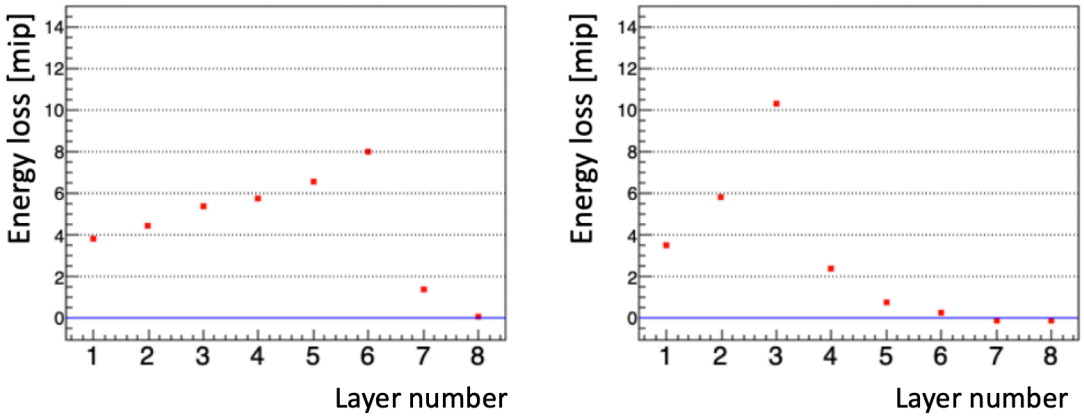

Figure 4.23: Energy loss in each layer for typical stop events of protons

4.4.5 Comparison of Experimental Data with SRIM

I compared the energy deposit in the prototype obtained in the low momentum pion run with the calculation by the SRIM (Stopping and Range of Ions in Matter) code [53, 54] in order to verify the validity of the data and investigate effects of pion interaction on identification of stop layer.

Energy Deposit Difference

The comparison of energy deposit in the prototype between data and the SRIM calculation for typical events satisfying $\beta < 0.7$ is shown in Fig. 4.24. The calculation of SRIM was performed using the β from the data, where I defined the initial β as β_{init}. I used the ranges and dE/dx for each kinetic energy of a particle in a plastic scintillator predicted by the SRIM code. The particle was set as a positively charged particle with the pion mass, and the density of the plastic scintillator was set the same as that of EJ200.

As shown in Fig. 4.24, there are no large differences between the data and the SRIM calculation for particles with a large β_{init} penetrating the prototype like the event 170 and the event 171. For stop events like the event 163, 176, and 177, the stop layers are different between the data and the SRIM, and for these events, it can be observed that the energy deposits in the stop layer calculated by the SRIM

are larger than those of the data.

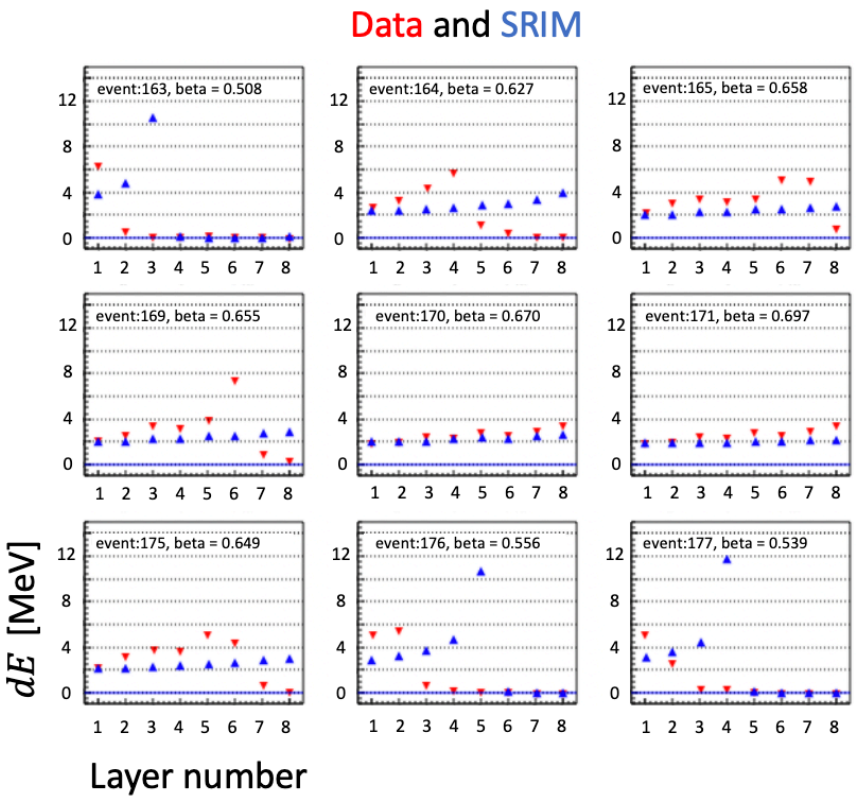

Figure 4.24: Comparison of energy deposit in the prototype between the data and the SRIM calculation for typical events satisfying $\beta < 0.7$ in data (Data: red, SRIM: blue)

Beta Dependence of Energy Deposit Difference

The stop layer differs between the data and the SRIM as shown in Fig. 4.25. One possible reason for this is that the measured β_{init} is larger than the true β value. Secondly, the large difference of the data from the SRIM in small β_{init} may suggest a difference of the interaction in the SRIM from the real interaction in lower energy regions. The third one is that muons were mixed in with the pions.

However, the second reason is not likely considering the accuracy of the SRIM calculation. The SRIM code is based on real data measured in many experiments so far. In the regions of the energy of Bragg peaks and less than the energy, the error of the stopping power in the SRIM is as large as $5 - 10\%$. As a particle with a kinetic energy of less than 10 MeV has a range shorter than one layer thickness of the prototype, the measured range is determined by the accuracy in the kinetic energy region larger than 10 MeV. The accuracy of dE/dx is less than 2% in this region [53, 54], which means there is no possibility of misidentifying the stop layer

more than one layer due to difference of the SRIM from the real interaction.

The third reason should be also considered. I calculated the same way as in the case of pions assuming the particles as muons. However, the stop layers differ very much between data and SRIM also with the assumption.

Therefore, I consider the difference of the measured β_{init} values from the true ones as the first reason why the stop layers of the data and the SRIM are different as mentioned at the beginning of this section.

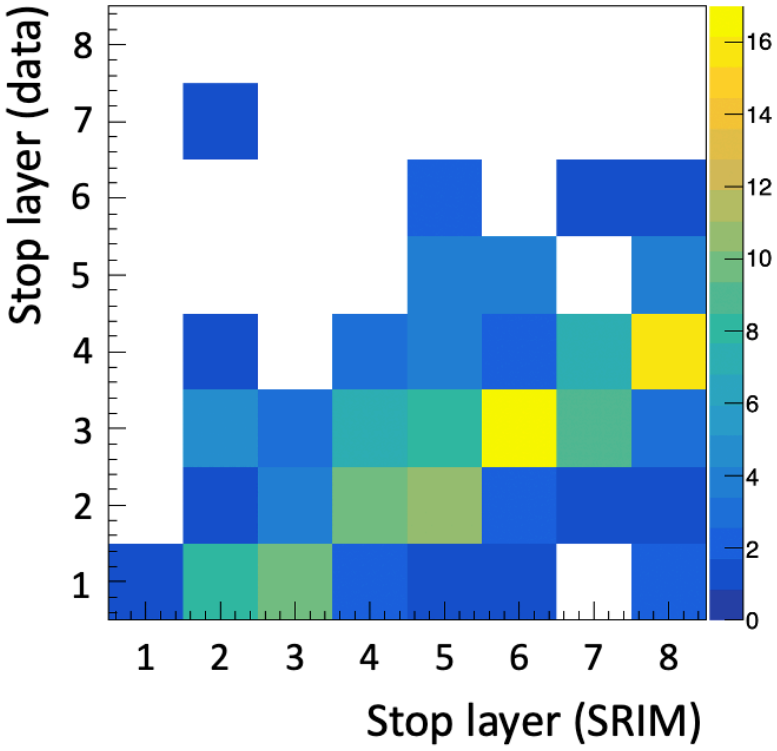

Figure 4.25: Correlation of stop layer between the data and the SRIM. It is observed that the stop layers are different between both for many events and also that many particles stopped in shallower layers than the SRIM calculation, which results in the ΔED being much less than zero.

I changed the measured β values by changing the factor C as $\beta_{init} \rightarrow C \cdot \beta_{init}$ so that stop layers in data and the SRIM become the same. Figure 4.26 shows the result. When the factor of C was adjusted to 0.9022, the stop layer correlation between the data and the SRIM was changed as shown in Fig. 4.26 top. Figure 4.26 bottom shows a projected distribution of the stop layer in the SRIM for the events in which particles stop in the 7th layer in the data and the fitted gaussian function, where the mean stop layer is 7.00 and the σ is 1.07. I changed the C so that the

mean value of the stop layer becomes seven, and I obtained this result. I use this factor $C = 0.9022$ in the following discussions. As shown in Fig. 4.26 top, for all the stop layers from 1st to 6th, the stop layers in the data and the SRIM calculation agree with each other. Figure 4.27 shows energy deposits in each layer for typical events with the adjusted β_{init}. These events are selected randomly. The data and the SRIM are much more consistent than in Fig. 4.24. In addition, I confirmed that the possibility of misidentification of stop layer by more than one layer is less than 10%. This suggests that effects of pion interaction is small enough.

Although the stop layers differ between the data and the SRIM under the assumption that the particles are muons as referred to at the beginning of this section, the possibility that the particles are muons should be mentioned a little more. I performed the same analysis under the assumption that the particles are muons, but I need the same adjustment in that case. The β_{init} should be also made about 5% slower. Therefore, I conclude that the β_{init} is estimated to be larger than the true value.

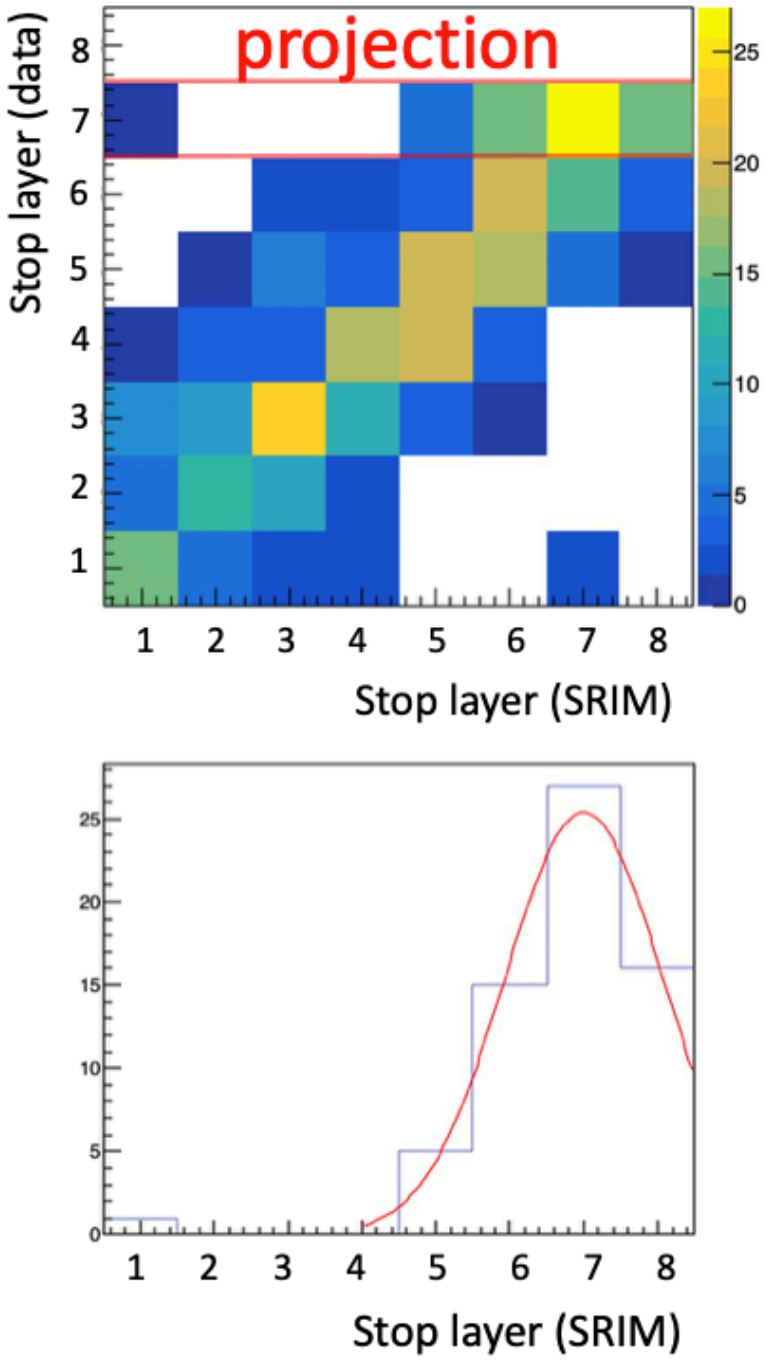

Figure 4.26: Top shows a correlation of stop layer between the data and the SRIM after adjustment of the β_{init} as $\beta_{init} \rightarrow C \cdot \beta_{init}$. The bottom shows a projected distribution of the stop layer in the SRIM for the events in which particles stop in the 7th layer in the data and the fitted gaussian function, where the mean stop layer is 7.00 and the σ is 1.07.

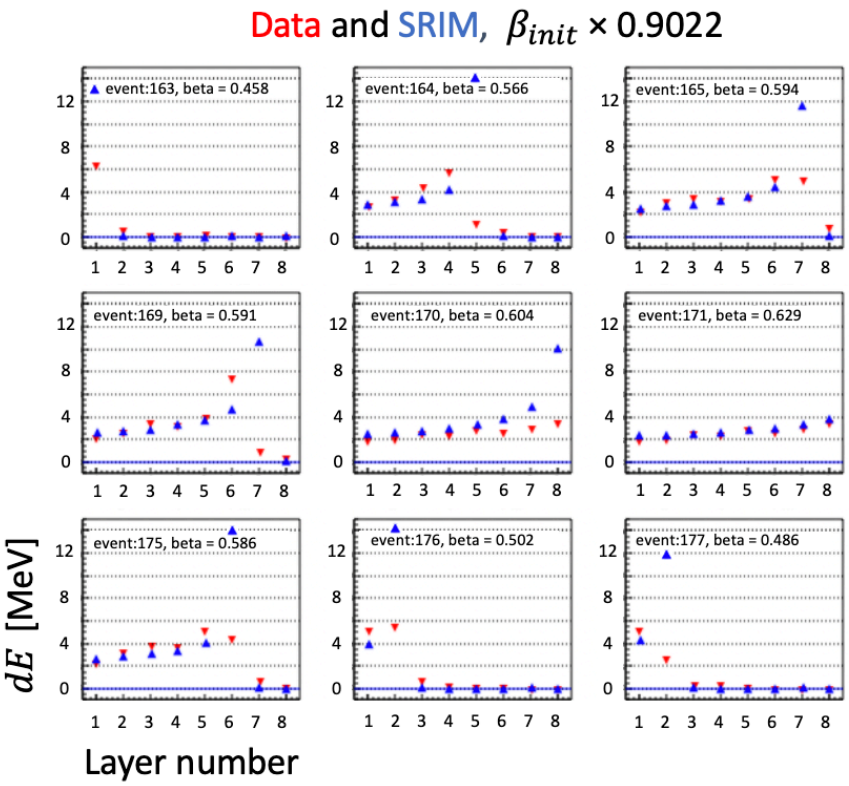

Figure 4.27: Energy deposits in each layer for typical events with the adjusted β_{init}.

Figure 4.28 and 4.29 respectively show two-dimensional distributions of energy deposit difference from the SRIM ($\Delta dE = dE_{data} - dE_{SRIM}$) with the β_{init} and the adjusted β_{init} ($0.9022 \times \beta_{init}$) for each layer (L1 – L8), where the events are selected by requiring energy deposit in the 1st layer to be more than 1 MeV. Compared to Fig 4.28, the data and the SRIM are matched better thanks to the adjustment of the β_{init}. In Fig. 4.29, the points in the region of $\Delta dE < 0$ are the events in which particles stop in the layer, but the energy deposit of the SRIM is larger than that of the data due to a quenching effect.

In the stop layer, large energy is deposited in the SRIM. The reasons why the ΔdE is much less than zero are the following two. First, it is explained by the quenching effect in plastic scintillator. For a large dE/dx in the scintillator, response to the energy deposit becomes non-linear due to a quenching effect of scintillation. Figure 4.30 shows two-dimensional distributions between the stop layer and the energy deposit in the layer for data (left) and the SRIM (right). The energy deposit in the stop layer is about twice smaller as that in the SRIM. Ref. [55] reported that the quenching factor is about $0.3 - 0.9$ at $dE/dx = 10 - 100$ MeV/cm and also the factor becomes lower for larger dE/dx. This is consistent with the difference of the

data and the SRIM in Fig. 4.30.

From the study with the adjusted β_{init}, it is considered that the measured β_{init} was shifted to the faster side. In addition, all the β_{init} values from all the combinations of TOF counters should be systematically changed to the slower side in order to make the difference between the data and the SRIM small. Two possible reasons for this are considered. One is that there is something wrong with measuring the distance between the TOF counters and the second is with correcting the TOF. In the former case, the 10% difference of the β corresponds to the 14 cm difference of the distance between TOF counters. In the latter case, something wrong with time calibration led to the problem, but I carefully calibrated the TDC using a time calibrator module, and then, it is impossible.

Despite the systematic discrepancies in the β, the energy losses in the data and SRIM match very well after the discrepancies are removed, except for the energy deposit at the stop layers. The difference in the deposit at the stop layer is about a factor of 2, which is considered to be due to the quenching effect. Although the reaction between a pion and matter via strong interaction in the low energy region is complicated and still poorly understood, the results of this experiment show that the data and the SRIM are very well matched for many events. Although statistics is poor, there are some events in the $\Delta dE > 0$ region, and these may be those events in which the π^- reacts via strong interaction with the matter and loses a large energy. Considering the quenching effect in plastic scintillator, the positive ΔdE value far off from 0 means that there was a much larger energy loss than the one dropped by electromagnetic interaction. In the next section, I will discuss how large energy deposit the prototype can measure when the reaction of π^- occurred due to strong interaction in plastic scintillator.

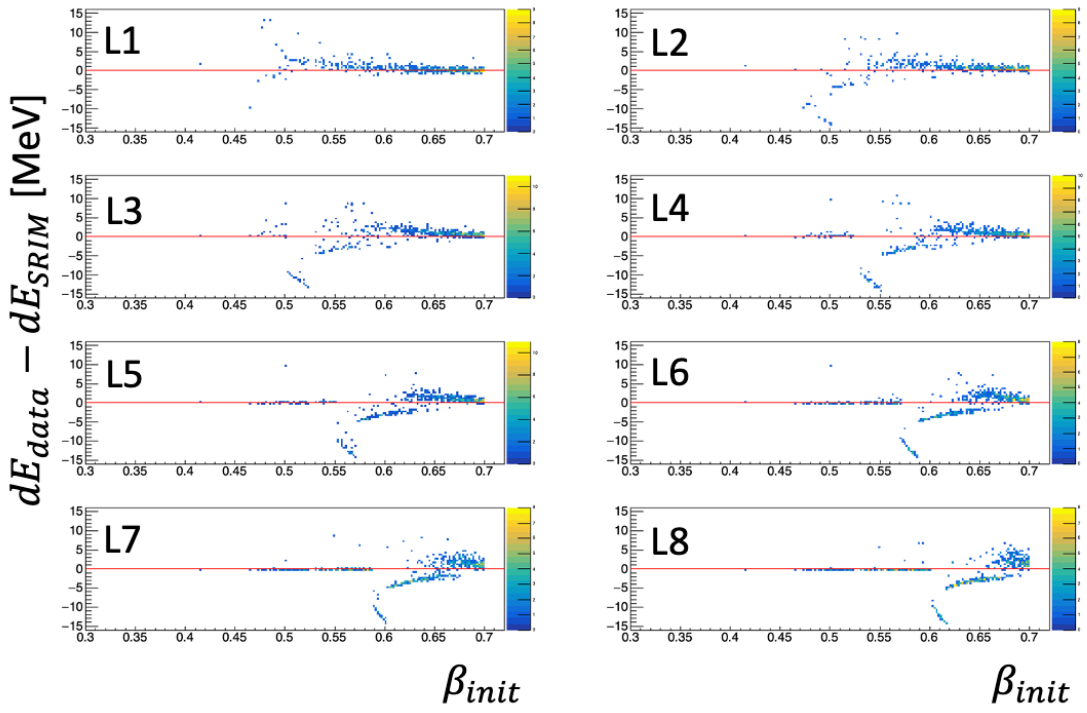

Figure 4.28: 2D distribution of dE difference from the SRIM ($\Delta dE = dE_{data} - dE_{SRIM}$) and the β obtained from TOF (β_{init}) for each layer (L1 – L8).

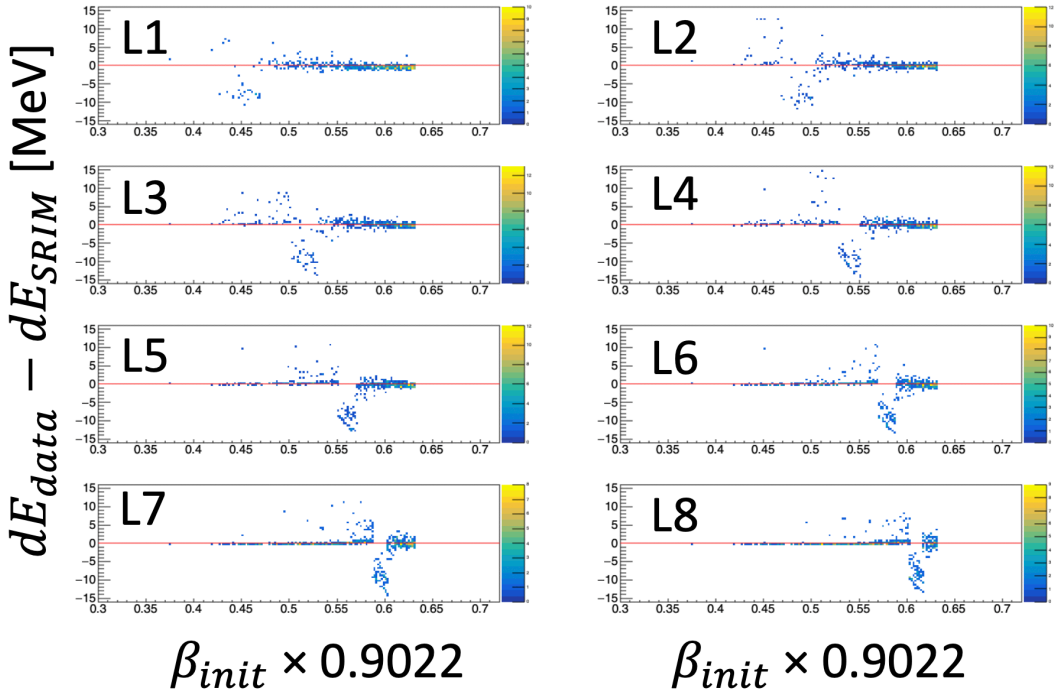

Figure 4.29: 2D distribution of dE difference from the SRIM ($\Delta dE = dE_{data} - dE_{SRIM}$) and the adjusted β_{init} ($0.9022 \times \beta_{init}$) for each layer (L1 – L8). The events with $\Delta dE > 0$ become less than those in Fig. 4.28.

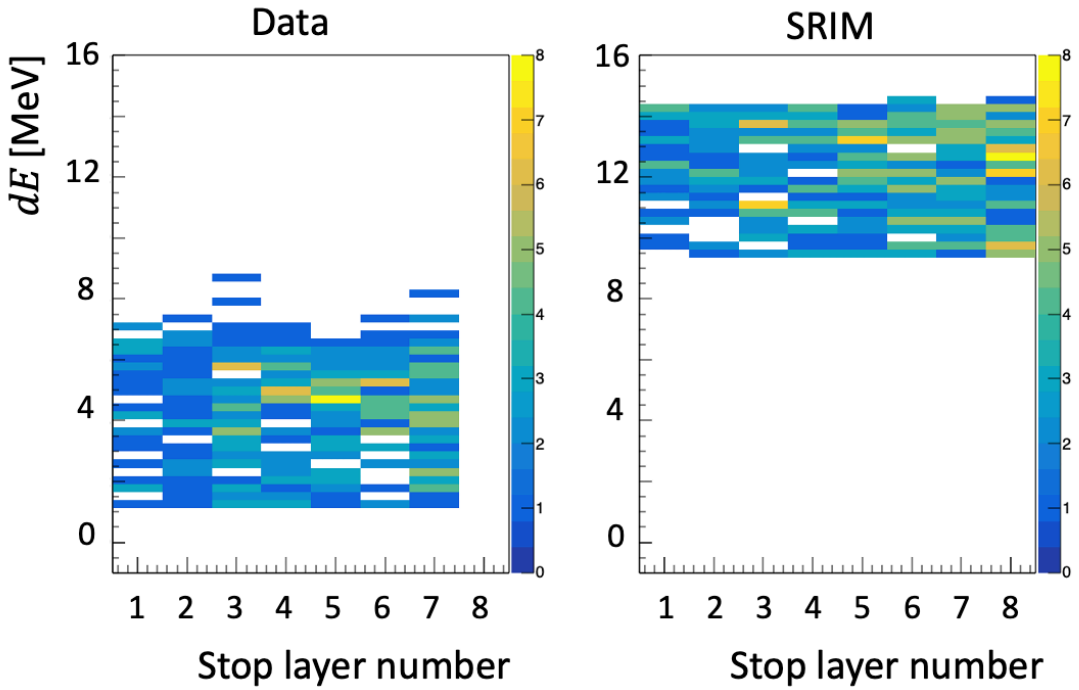

Figure 4.30: 2D distributions of stop layer and energy deposit in the layer for data (left) and the SRIM (right) after adjustment of the β_{init}. The energy deposit in the stop layer is about twice smaller as that in the SRIM.

Pion Absorption in Nuclei

The process of pion absorption in the plastic scintillator EJ200 (styrene, C_8H_8) should be considered for verifying the validity of the results.

First, I consider the absorption of π^- on a C nucleus in styrene. Absorption on a pn pair carrying the quantum number of the deuteron in the nucleus is a dominant mechanism for stopped negatively charged pions. In this reaction, the pn pair absorbs π^- and dominantly emits nn with large kinetic energies coming from the pion mass. The π^- absorption on pp pair or other clusters in the nucleus also occurs, which results in emission of p and/or n via $pp\pi^- \rightarrow pn$ or emission of other charged particles like deuteron (d), triton (t), ^{3}He, and ^{4}He [56]. The stopped π^- absorption on pp pairs is about one order of magnitude less probable than that on pn pairs [57, 58].

Figure 4.31 shows the yields of charged particles from the reaction via stopped π^- on various targets including ^{12}C [56]. From absorption of stopped π^- on ^{12}C, protons are dominantly produced. Deuterons and tritons are also less produced by

a few factors than protons. The energy distributions of these particles are shown in Fig. 4.32 [59]. The kinetic energy of the emitted protons, deuterons, and tritons is mainly distributed around $10 - 20$ MeV. At low momenta, the energy deposit per distance (dE/dx [MeV/cm]) becomes large. As mentioned in Sect. 4.4.5, the response to the energy is not linear due to the quenching effect of scintillation for a large dE/dx in the scintillator. The range of the proton with a 20 MeV kinetic energy is 4.5 mm, that is, $dE/dx = 44$ MeV/cm. The quenching effect factor is about 0.6 [55] at $dE/dx = 44$ MeV/cm, and the factor becomes lower for larger dE/dx. With the assumption that the proton loses all the energy of 20 MeV only in one layer, the energy deposit is observed as if $20 \times 0.6 = 12$ MeV energy was deposited in the pion stop layer without any correction to the quenching effect. When other heavy charged particles like d and t with the same atomic number as the proton have the same initial kinetic energy as that of the proton, their ranges are shorter than that of the proton. Therefore, emission of charged particles due to stopped π^- absorption does not give a large effect on the determination of the stop layer.

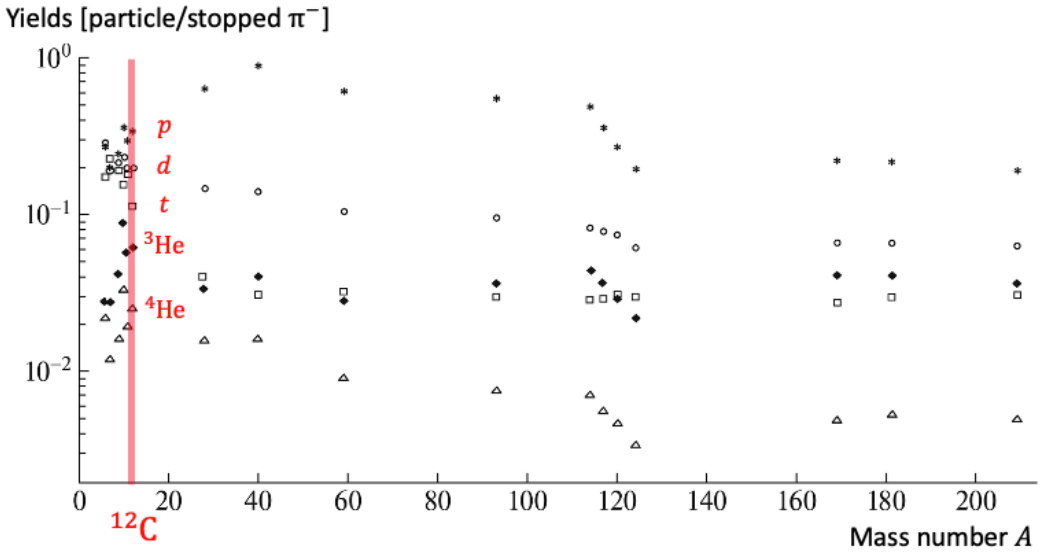

Figure 4.31: Experimental data of yields of charged particles from the reaction via stopped π^- on various targets with mass number A from 6 to 209 [56]. From absorption of stopped π^- on ^{12}C, protons are dominantly produced. Deuterons and tritons are also less produced by a few factors than protons. ^{3}He and ^{4}He are also emitted but in lower yields.

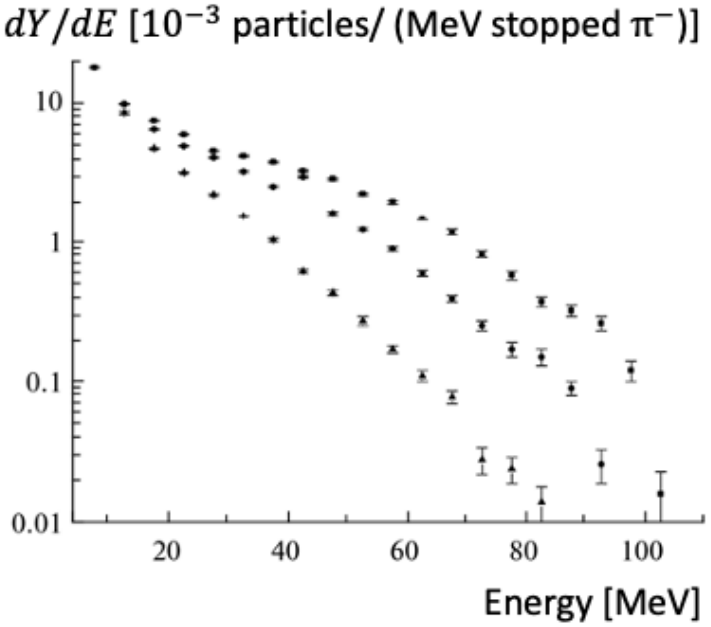

Figure 4.32: Experimental data of kinetic energy distributions for emitted particles of p, d, and t from π^- absorption on ^{12}C [59]. They are emitted dominantly with kinetic energies of $10 - 20\,\mathrm{MeV}$. The data points represent p, d, and t from top to bottom.

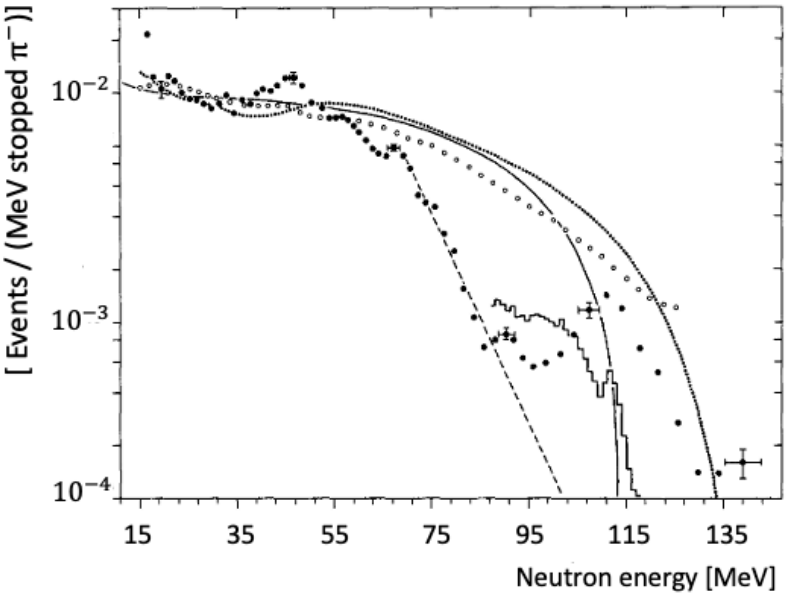

Figure 4.33: Experimental data of single neutron energy spectrum from 15 to 150 MeV obtained by the reaction of stopped π^- on ^{12}C. The data from Ref. [62] (open circle), Ref. [61] (dotted line), Ref. [63] (histogram), and Ref. [60] (full circle). The dashed line shows the kinematical limit for the two-body nucleon emission reaction. The peak at 111 MeV is derived from the neutron from the $^{12}\mathrm{C}(\pi^-, \mathrm{n})^{11}\mathrm{B}$ reaction. The 89 MeV peak is explained by the α cluster structure in ^{12}C nucleus, derived from the neutron from the $^{4}\mathrm{He}(\pi^-, \mathrm{n})^{3}\mathrm{H}$ reaction.

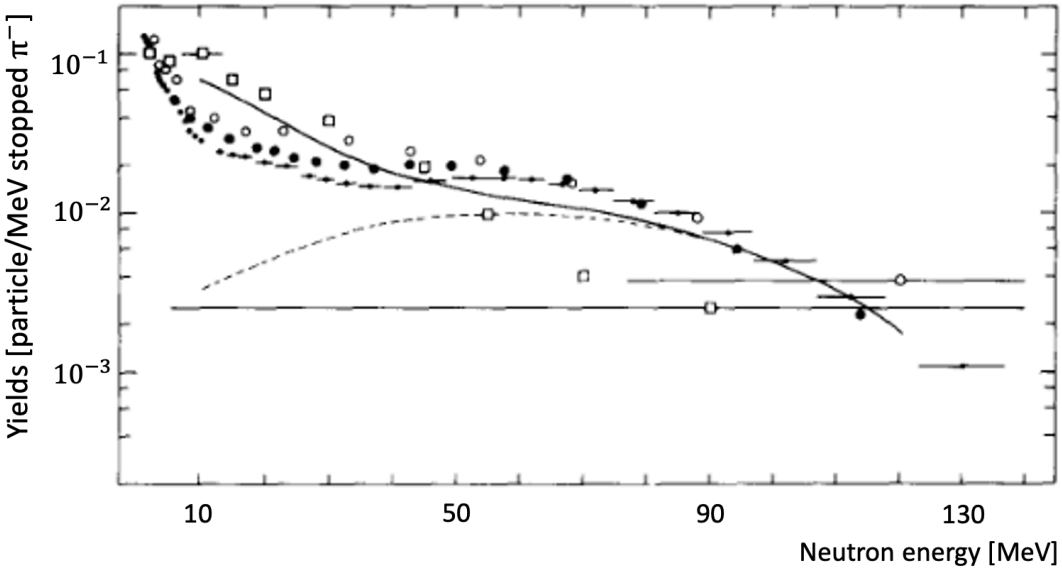

Figure 4.34: Experimental data of single neutron energy spectrum from 0 to 145 MeV obtained by the reaction of stopped π^- on ^{12}C. The data from Ref. [61] (dots), Ref. [64] (closed circle), Ref. [65] (open box), and Ref. [66] (open circle). Figure from Ref. [67].

In the absorptions of π^- on a pp pair and other clusters as well as that on a pn pair, one or multiple neutrons are emitted from the absorption. The energy of the emitted neutron from stopped π^- on ^{12}C was measured in the past [60, 61, 62, 63, 64], and the distribution is shown in Fig. 4.33 and Fig. 4.34. The kinetic energy of the emitted neutron by the reaction is dominantly around 10 MeV and less than that. The mean free path of a neutron with about 10 MeV in styrene is estimated to be 1 m using the reaction cross sections of a neutron with about 10 MeV on C (σ_{C}) and H (σ_{H}), which were measured to be 0.8 and 1.2 barns, respectively [68]. Although the neutrons with higher kinetic energies than 10 MeV are emitted with some probabilities, the reaction cross section with styrene tends to become lower in the higher energy regions. Therefore, detection by the prototype of the neutrons emitted by π^- absorption on C nucleus is negligible.

The second thing to be considered is that absorption on H in styrene also occurs with some probabilities. The probability is lower than that of absorption on C because of the smaller atomic number than carbon. π^- absorption on a bound proton undergoes $(\pi^- p)_{\text{at rest}} \rightarrow n\pi^0\,(60\%)$ or $n\gamma\,(40\%)$ [69]. These neutrons are not problematic because the reaction cross section is very low. Either the emitted π^0 or γ in the two processes do not matter. Since 2γ from decay of the π^0 in the former process and the γ in the latter process have a large energy ($\simeq$pion mass), they are unlikely to interact in the thin prototype range counter.

Considering all the processes discussed here, the results obtained in this experiment are understandable. If the π^- is absorbed in the plastic scintillator, emitted particles of both neutral (n and γ) and charged (p, d, t, and other heavy nuclei) ones do not affect determination of the pion stop layer because emitted charged particles stop in a short range ($\simeq$4 mm) with an energy deposit of the order of 10 MeV and the reaction probability of neutral particles is very low in the thin prototype.

I summarize the effects from the pion absorption on identification of the stop layer. If the pion stops in Nth layer and charged particles are emitted, the particles will stop in a short range, that is to say, the stop layer should be considered as $(\mathrm{N}-1)$, N, or $(\mathrm{N}+1)$th layers. This is consistent with low possibility of stop layer misidentification of less than 10%.

For further discussion, I need to study with more elaborated simulation codes and study the pion interaction in the range counter in detail by exposing a monochromatic π^- beam to the range counter and taking high-statistics data in near future.

4.5 Discussion

4.5.1 Separation of Pions by the Prototype

Hereafter, I discuss if the prototype can separate the pions from ${}^{4}_{\Lambda}\mathrm{H}$ and ${}^{3}_{\Lambda}\mathrm{H}$.

The upper part of Fig. 4.35 shows a correlation between incident energy and the range for pion stop events. Here, the incident energy means the kinetic energy which pions have just before entering the prototype and was obtained from the adjusted β discussed in the previous section. In this experiment, I did not prepare the position detector, and the flight path of the particles was determined only with the TOF counters. The range was obtained by assuming that the particles passed through the center of the segments of the TOF counters and stopped at the center of the stop layer in the prototype.

The prototype is thinner than the thickness required to stop the pion from ${}^{4}_{\Lambda}\mathrm{H}$ with the kinetic energy of 53 MeV, and then, based on the following discussion, I selected the lower energy regions than 53 MeV. The selected energy regions are 33 ± 0.75 MeV and 20 ± 0.75 MeV of the incident energy (I.E.) with their energy difference of 13 MeV equal to the kinetic energy difference (ΔK.E.) of the pions from ${}^{4}_{\Lambda}\mathrm{H}$ (53 MeV) and ${}^{3}_{\Lambda}\mathrm{H}$ (40 MeV). The higher kinetic energy the particles have, the easier it is to separate the particles with their ranges as described below. Thus, if the energies of 33 MeV and 20 MeV are separated with the range measured by the prototype, the range counter can separate the pions from ${}^{4}_{\Lambda}\mathrm{H}$ and ${}^{3}_{\Lambda}\mathrm{H}$. I plotted the range distributions for these two energy regions shown in the bottom part of Fig. 4.35.

From the above discussion, they are well separated with a confidence level of 2.2σ, corresponding to a very low possibility of less than 2% of misidentifying ${}^{4}_{\Lambda}\mathrm{H}$ and ${}^{3}_{\Lambda}\mathrm{H}$. Therefore, I conclude that, in the E63 experiment, ${}^{4}_{\Lambda}\mathrm{H}$ and ${}^{3}_{\Lambda}\mathrm{H}$ can be separated by measuring their weak decay pions using the range counter.

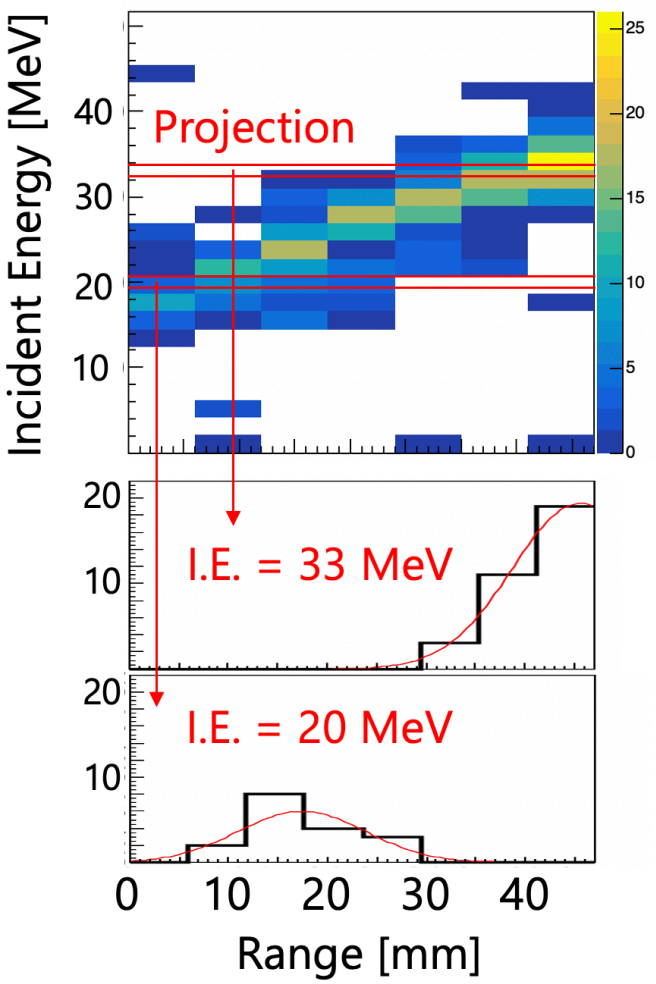

Figure 4.35: Top: Correlation between incident energy (I.E.) measured by T1-T2 TOF and the measured range for pion stop events. Bottom: measured range distributions for the incident energy ranges of 33 ± 0.75 MeV and 20 ± 0.75 MeV.

Energy Ambiguity from TOF Resolution

The ambiguity of the selected incident energy due to the resolution of TOF distributed from 105 to 225 ps (Table 4.3) is 1.0 MeV for 20 MeV of I.E. and 2.4 MeV for 33 MeV of I.E.

Table 4.4: The calculated relative range straggling ϵ (%) for protons in Be, C, Al, and Cu [52] and the kinetic energy of pions (KE (pion)) converted from the kinetic energy of protons (KE (proton)) with the assumption that pions have the same velocity with protons.

KE (proton) [MeV]	KE (pion) [MeV]	KE/mass	Be	C	Al	Cu
2	0.30	0.002	1.704	1.867	1.968	2.293
4	0.59	0.004	1.550	1.631	1.814	2.030
6	0.89	0.006	1.469	1.526	1.720	1.875
8	1.19	0.008	1.419	1.466	1.649	1.779
10	1.48	0.010	1.382	1.424	1.597	1.749
20	2.96	0.021	1.286	1.315	1.450	1.609
40	5.93	0.042	1.206	1.230	1.330	1.468
60	8.89	0.064	1.165	1.183	1.271	1.390
80	11.86	0.085	1.135	1.152	1.231	1.339
100	14.82	0.106	1.109	1.178	1.271	1.431
200	29.64	0.213	1.041	1.054	1.112	1.190
250	37.05	0.266	1.017	1.029	1.084	1.155
300	44.46	0.319	0.997	1.009	1.060	1.127
350	51.87	0.373	0.980	0.991	1.040	1.104
400	59.28	0.426	0.966	0.976	1.023	1.085

Range Straggling

The range straggling is expected to be smaller as a relative value in higher energy regions. Table 4.4 shows relative range straggling ϵ for protons in Be, C, Al, and Cu [52], where ϵ is defined by R (range) and σ_{strag} (range straggling) as $\epsilon = (\sigma_{\mathrm{strag}}/R \times 100\,[\%])$. It suggests that ϵ becomes small with high kinetic energy or in matter with a small atomic number. The ϵ value in plastic is expected to be less than that in carbon in the table. I estimated the relative range straggling for pions from values in Table 4.4 using a scaling law as a function of the velocity, β, because the Range/Mass and the range straggling depend only on β. The values of proton kinetic energy in Table 4.4 are converted to values for the pions with the same β as protons. The relative range straggling in carbon is very small, about 0.991% for pions with a kinetic energy of 51.87 MeV. Therefore, the range straggling in the prototype is estimated to be 0.5 mm or smaller. The peak width (rms) of the range distributions at the bottom part of Fig. 4.35 are both larger than 0.5 mm, and this is considered to come mainly from the resolution of time of flight of about 10%. Since the range peak width is mainly determined by the limited time resolution, the results show that the pions from ${}^{3}_{\Lambda}\mathrm{H}$ and ${}^{4}_{\Lambda}\mathrm{H}$ can be separated more safely using the range counter.

4.5.2 Energy Resolution

In this section, I investigate if the range counter meets the requirement; the kinetic energy resolution (σ_{KE}) should be less than 3.0 MeV in order to identify the hypernuclei of ${}^{4}_{\Lambda}\mathrm{H}$ and ${}^{3}_{\Lambda}\mathrm{H}$ as explained in Sect. 3.2. Figure 4.36 shows a relation between the kinetic energy of pions and its σ_{KE}. The correlation in Fig. 4.35 was projected onto the axis of the kinetic energy for each layer, and each projected distribution was fitted with a Gaussian function. Data points and their errors in Fig. 4.36 were obtained using the mean value, the standard deviation (σ_{KE}), and the error of the standard deviation as a result of the fitting. The error bars for small kinetic energies are large because their statistics are relatively poor. The σ_{KE} required for the range counter system is less than 3 MeV, and in this energy region, the σ_{KE} is below 3 MeV except for one point. The energy resolution due to the $5-10\%$ time resolution of the TOF counter is expected to be $1-2$ MeV for the kinetic energy region of $10-35$ MeV in Fig. 4.36. Since the energy resolution is mainly determined by the limited time resolution, the results show that the σ_{KE} for the pions from ${}^{3}_{\Lambda}\mathrm{H}$ and ${}^{4}_{\Lambda}\mathrm{H}$ with fixed kinetic energy is much better. Furthermore, this figure also shows that the σ_{KE} does not depend on the kinetic energy, and therefore, the σ_{KE} is expected to be less than 3 MeV even at the kinetic energy of pions emitted from ${}^{4}_{\Lambda}\mathrm{H}$ (53 MeV).

In conclusion, from the above discussion, I can say that the range counter satisfies the requirement for the kinetic energy resolution and can identify ${}^{4}_{\Lambda}\mathrm{H}$ and ${}^{3}_{\Lambda}\mathrm{H}$.

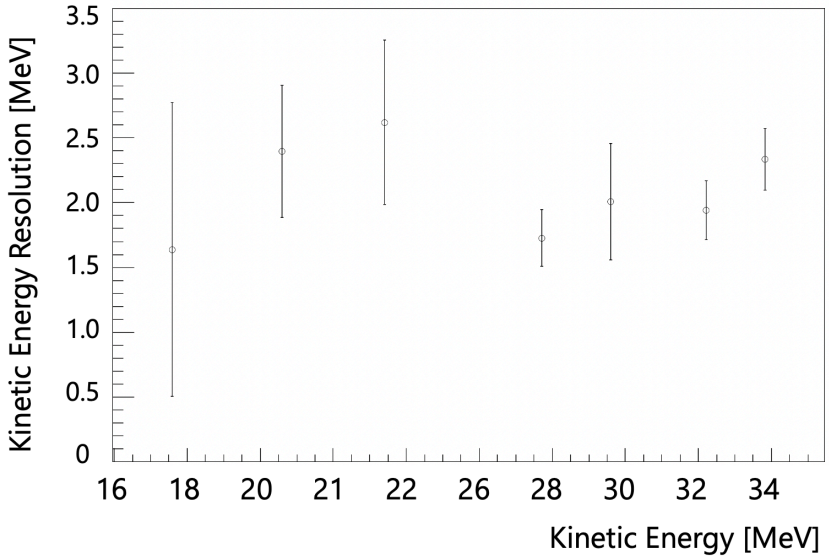

Figure 4.36: Relation between the kinetic energy of pions and its resolution. Data points and their errors were obtained as follows. The correlation in Fig. 4.35 was projected onto the axis of the kinetic energy for each layer, and each projected distribution was fitted with a Gaussian function. The data points and their errors come from the mean values, the standard deviations, and the errors of the standard deviation as a result of the fitting.

Chapter 5

Fabrication and Evaluation of Range Counter and Position Detector

I found that the prototype satisfies the requirement for the kinetic energy resolution and it can identify ${}^{4}_{\Lambda}\mathrm{H}$ and ${}^{3}_{\Lambda}\mathrm{H}$. Thus, I fabricated a whole set of the range counter and the position detector for the E63 experiment.

satisfies the requirement for the kinetic energy resolution and can identify ${}^{4}_{\Lambda}\mathrm{H}$ and ${}^{3}_{\Lambda}\mathrm{H}$.

5.1 Fabrication of Range Counter and Position Detector

5.1.1 Updates in Fabrication of the Range Counter

In this section, I explain the fabrication of a range counter and a position detector for the E63 experiment. There is no major update in the basic fabrication method of the range counter from the prototype fabrication (Sect. 4.2), but I made a few minor updates. I changed the tape for masking the plastic scintillator surface from the optical cement, which enables us to keep the scintillator surface much clearer than the prototype (Fig. 5.7). In addition, I polished the other end of the fiber that is not in contact with the MPPC, although I did not polish it when fabricating the prototype. These changes should contribute to increase in the number of photons. I also changed the hole size of the aluminum frame from 1.1 mm to 1.2 mm for the 1.0 mm diameter wavelength-shifting fibers (Fig. 5.8) in order to make it much

easier to pass the fibers through the holes to avoid damaging the fibers.

MPPC Readout Board for the Range Counter System

As described in Sect. 4.2, the readout board for the prototype was previously made of a two-layer circuit board, but it was changed to a six-layer board because I could not observe a single photon peak in ADC's of many channels with the previous board due to a significant high noise level. The noise made it difficult to adjust the gain for each channel and to confirm the number of photons observed in each SiPM. For noise reduction, the board was redesigned. The circuit and the board design is shown in Fig. 5.1 and Fig. 5.2. There are some updates from the previous board. First, I changed the number of layers from two to six. In the new design, layer 1, L1, is used for mounting components and HV lines, and L3 and L5 are used for mounting signal lines of the odd- and even-numbered channels, respectively. The increase of the number of layers contributed to securing a wider area between adjacent signal lines that can be covered with the ground for noise reduction. Second, the width of the signal lines was widened. The wider the signal width is, the less noise it picks up. In addition, the wider width between the signal lines helped to pin more vias to the ground than the previous board. The isolated ground acts as an antenna without vias, and the pinned vias will make the ground more stable.

MPPC readout boards for the position detector were newly designed. The circuits and the board design of PD-Y and PD-Z are shown in Fig. 5.3, Fig. 5.4 and Fig. 5.5, Fig. 5.6, respectively. The number of layers of the boards is four for the same reason as the board of the range counter. The L1 is used for mounting components and HV lines, and L4 is used for mounting signal lines and SiPMs.

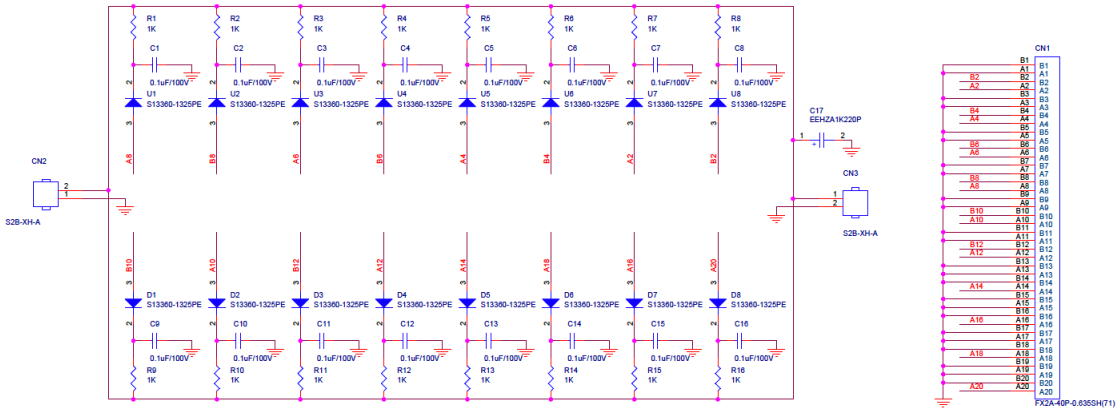

Figure 5.1:
Circuit of the MPPC readout board for the range counter. This circuit is made of 16 channels of MPPC. Each channel is composed of MPPC (S13360-1325PE), capacitor ($0.1\,\mu$F), and resistor ($1\,\mathrm{k}\Omega$).

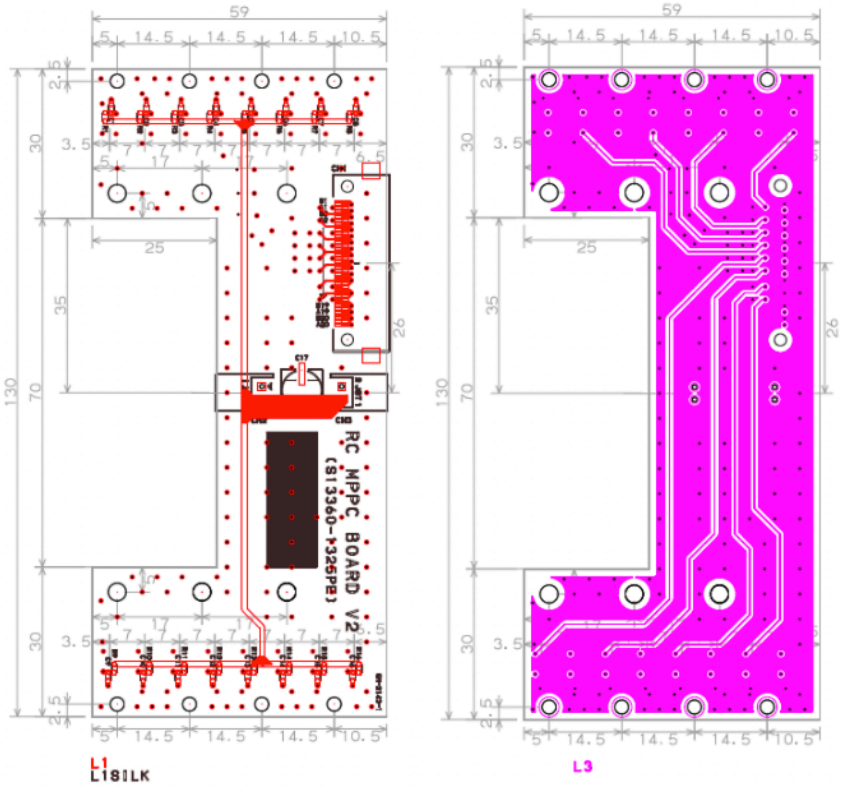

Figure 5.2: Board design of the MPPC readout board for the range counter. Left: L1 (front side) used for mounting components of cable connectors, capacitors, and resistors and for mounting HV lines. The red line represents the HV line. Right: L3 is used for mounting the signal lines of odd-numbered channels. The colored area represents the ground.

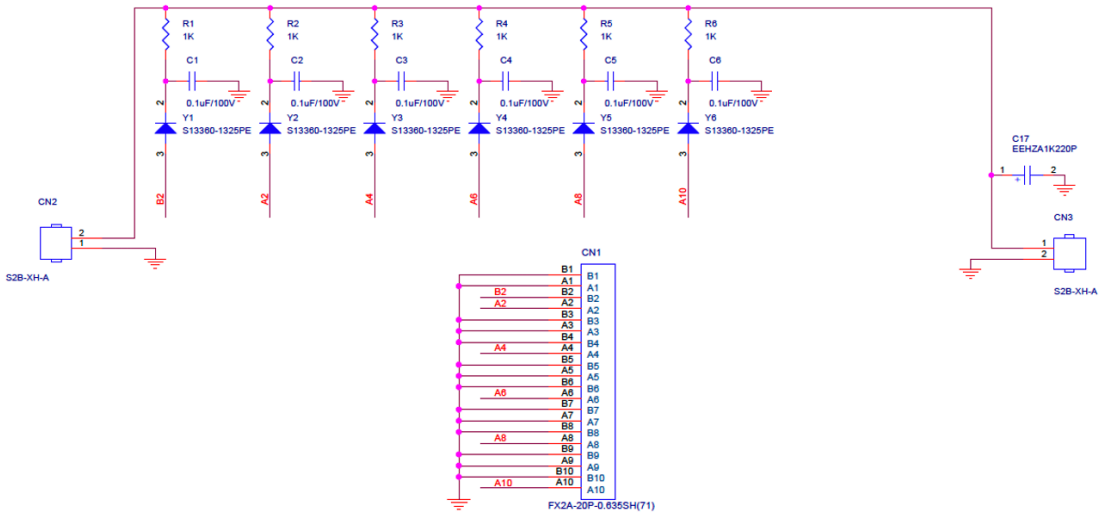

Figure 5.3:
Circuit of the MPPC readout board for the PD-Y. This circuit is made of 6 channels of MPPC. Each channel is composed of MPPC (S13360-1325PE), capacitor (0.1 μF), and resistor (1 kΩ).

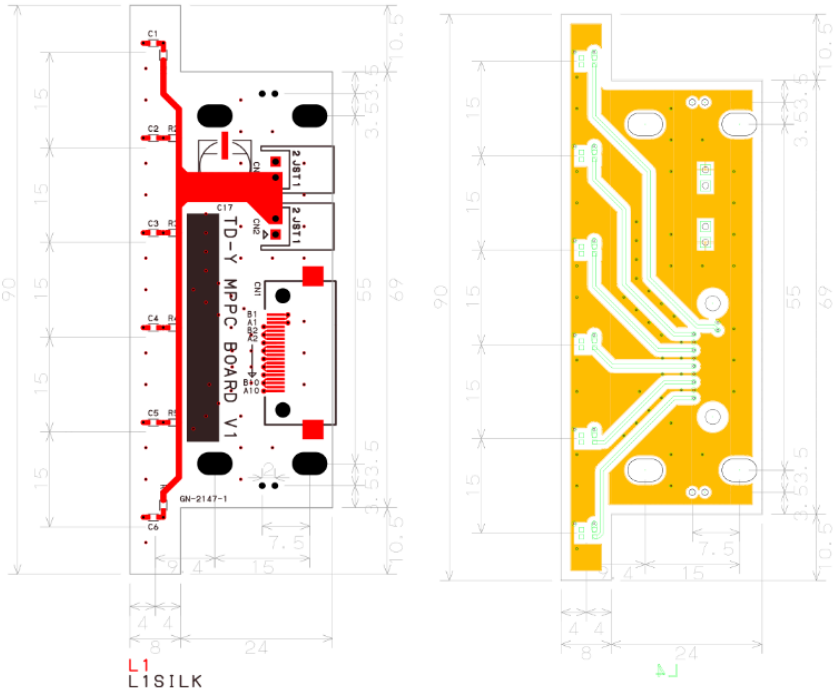

Figure 5.4:
Board design of the MPPC readout board for the PD-Y. Left: L1 (front side) used for mounting components of cable connectors, capacitors, and resistors and for mounting HV lines. The red line represents the HV line. Right: L4 used for mounting SiPMs and the signal lines. The colored area represents the ground.

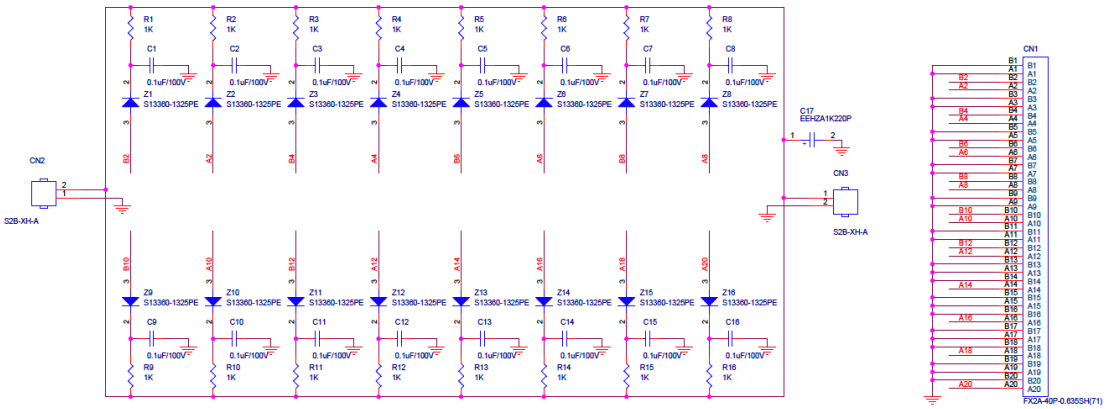

Figure 5.5:
Circuit of the MPPC readout board for the PD-Z. This circuit is made of 16 channels of MPPC. Each channel is composed of MPPC (S13360-1325PE), capacitor (0.1 μF), and resistor (1 kΩ).

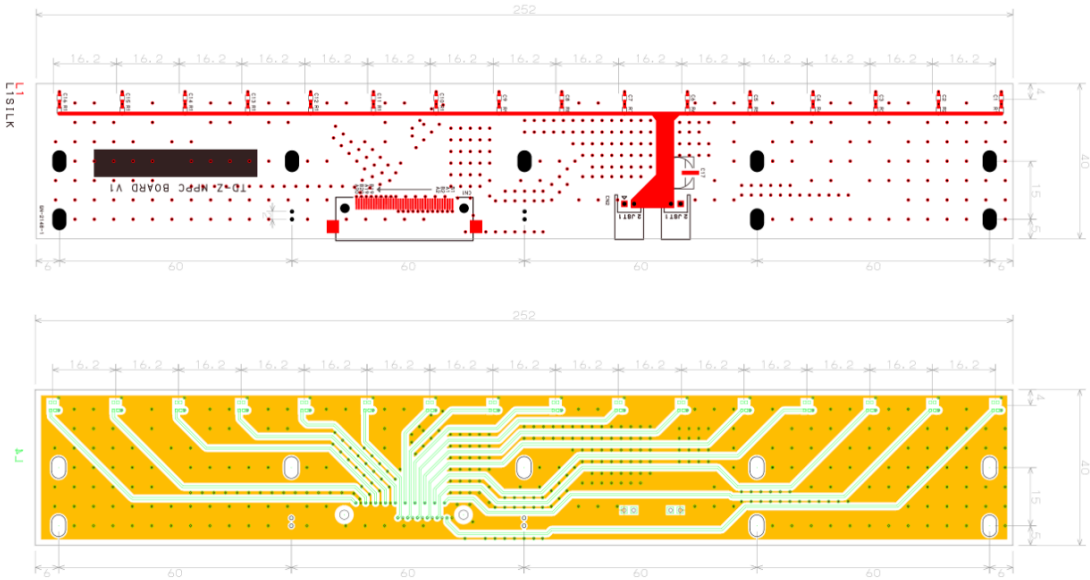

Figure 5.6:
Board design of the MPPC readout board for the PD-Z. Top: L1 (front side) used for mounting components of cable connectors, capacitors, and resistors and for mounting HV lines. The red line represents the HV line. Bottom: L4 used for mounting SiPMs and the signal lines. The colored area represents the ground.

5.1.2 Test of Photon Yield of the Position Detector

I made a test with one segment of PD-Y and measured the number of photons counted by a directly attached MPPC (S13360-13225PE, the same type as used in the RC) and the hit position dependence of the number of photons with a ^{90}Sr beta-ray source, as shown in Fig. 5.9. The gap between the scintillator and the MPPC was filled with an optical grease (EJ-550, Optical Grade Silicone Grease). As a result, more than about 10 photons are obtained at any source position, of which photon yield is sufficient for our purpose. The number of photons from the pion to be detected by the detector is expected to be more than the photon yield from the ^{90}Sr source because the pion with a momentum of 100 MeV/c lose about 1.2 MeV in 3 mm-thick plastic, and this is higher than the energy deposit (1 MeV) of the beta ray with the most probable kinetic energy from the ^{90}Sr source. I also found the number of photons for the beta decay to be six in the case of air gap, being less than the case using the optical grease.

In the fabrication of the position detector, I wrapped plastic scintillator segments with Teflon sheet and fixed them with the frame as shown in Fig. 5.10. The gap between MPPC and the edge of the scintillator is filled with optical sheet, Nitto CS9865UA 15 N/20mm Optically Clear Adhesive Tape.

Fig. 5.11 shows the whole setup of the range counter and the position detector without MPPC readout boards or flat cables and with them.

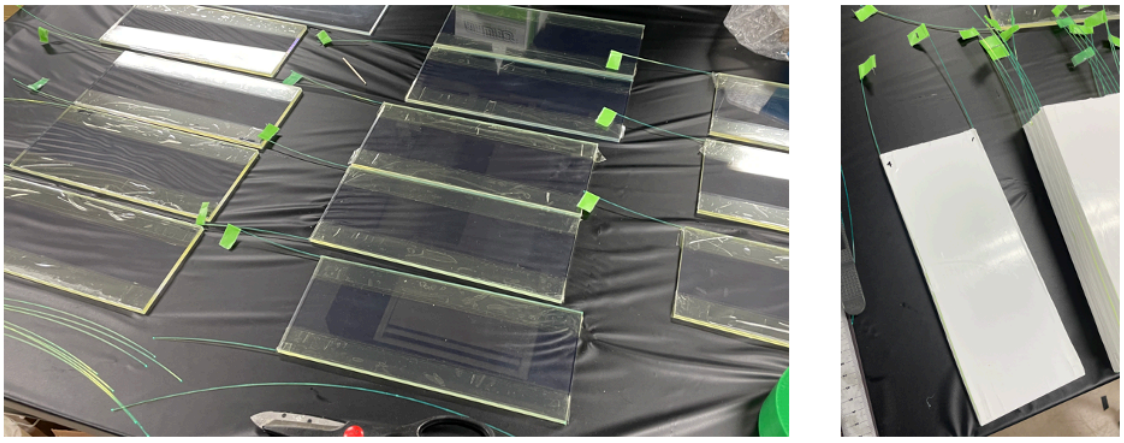

Figure 5.7: Fabrication 1. Mass production of embedding the fibers (left) and wrapping scintillator slabs with Teflon sheet (right).

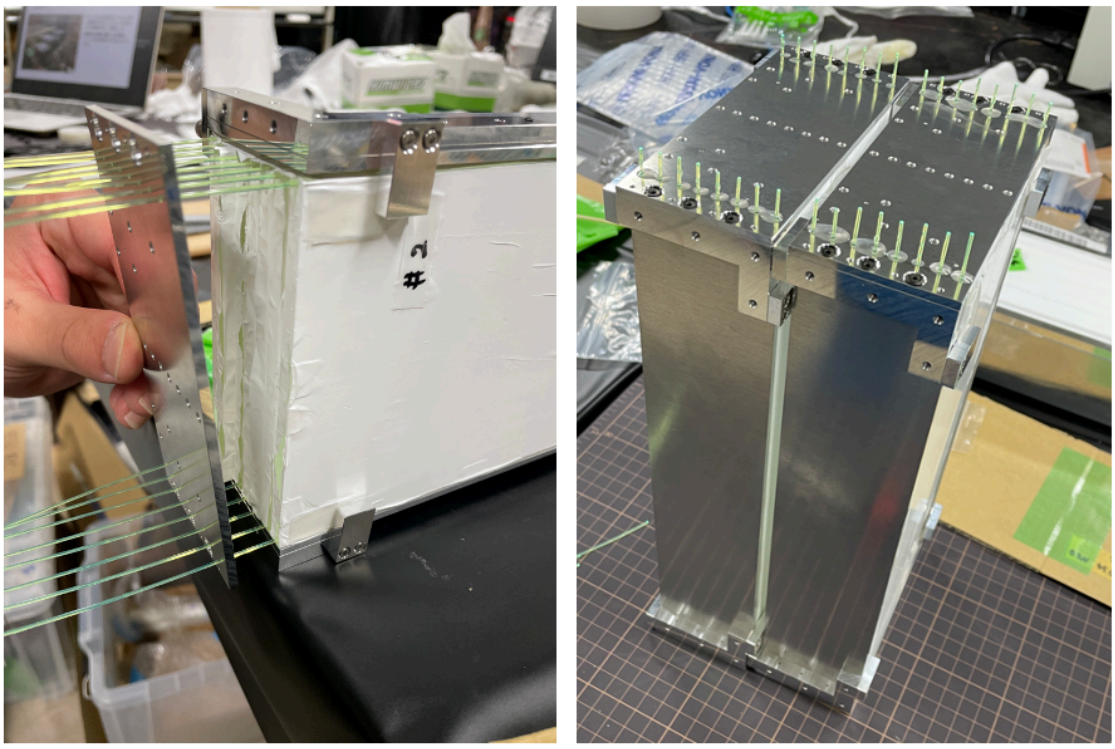

Figure 5.8: Fabrication 2. Process of fixing the plastic scintillator slabs with the frame.

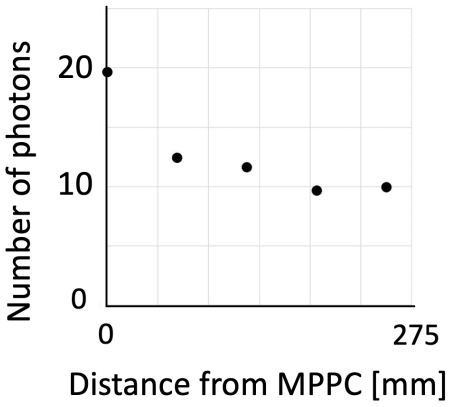

Figure 5.9: Hit position dependence of the number of photons in TD-Y measured with a ^{90}Sr beta source.

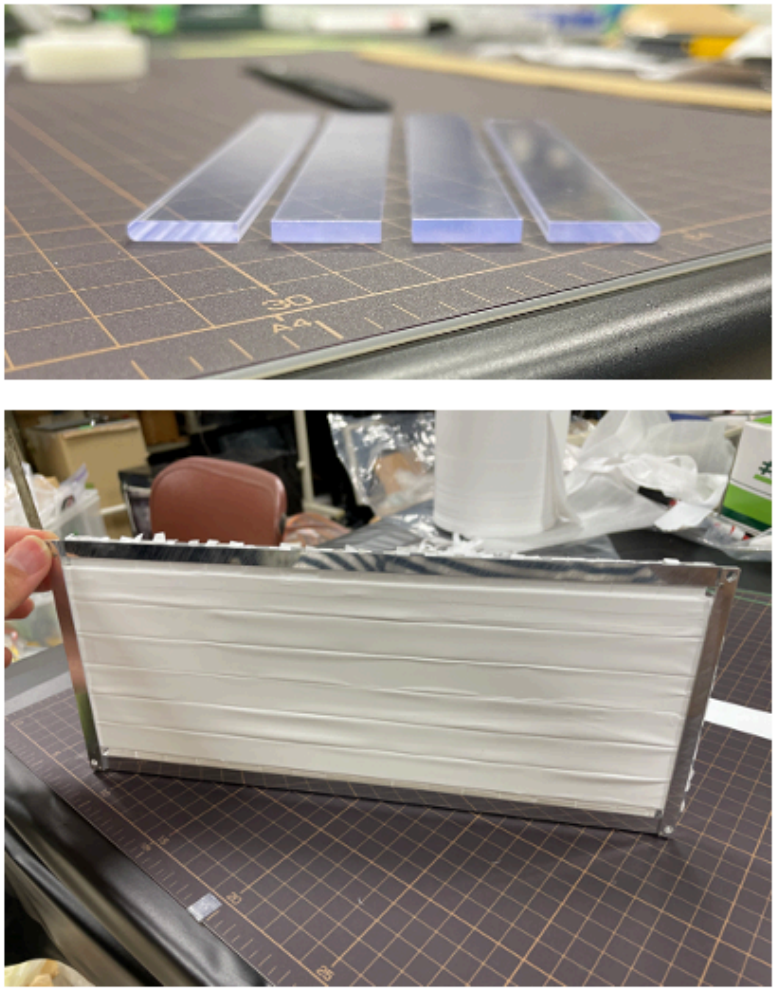

Figure 5.10: Plastic scintillator slabs for the position detector (top) and fabrication of the position detector (bottom).

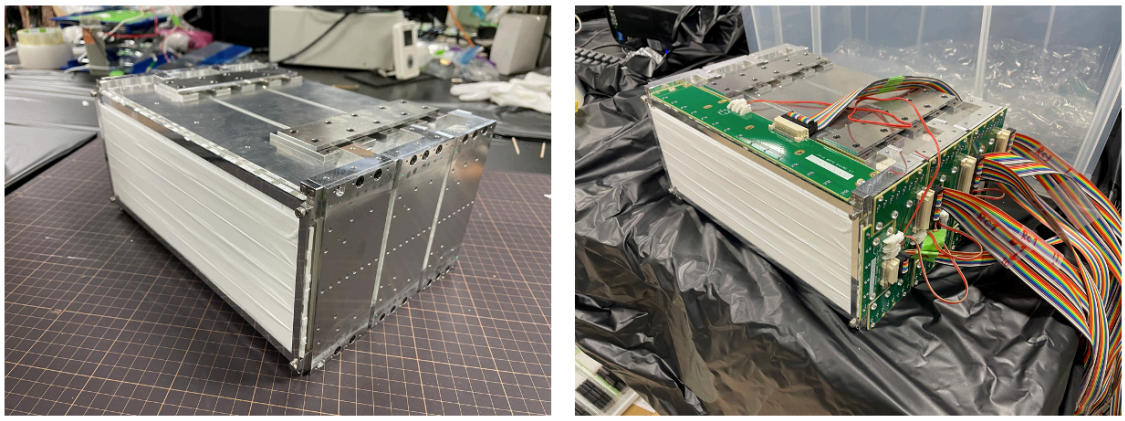

Figure 5.11: Whole setup of the range counter and the position detector without MPPC readout boards or flat cables (left) and with them (right).

5.2 Evaluation with Cosmic Rays

I conducted a simple experiment to test the range counter and the position detector with cosmic rays. The data-acquisition circuit is given in Fig. 5.12. We took data with a cosmic-ray trigger using a trigger counter. The GPIO distributes a signal for a trigger and HOLD to each VME-EASIROC board via the J0 bus on the VME crate. The common stop was distributed by another line directly to each VME-EASIROC board.

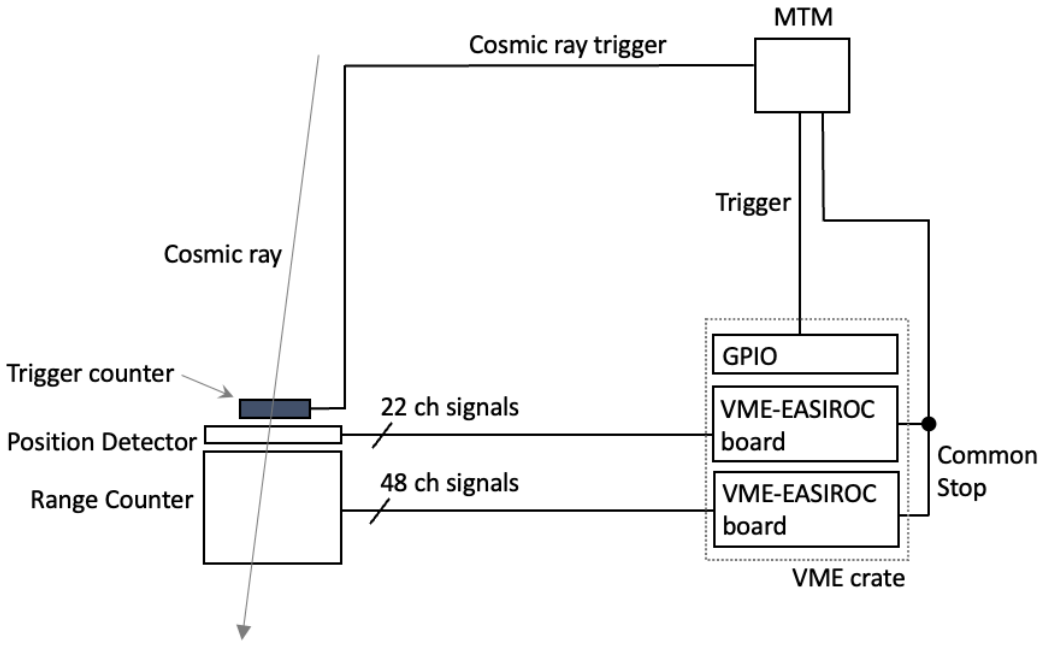

Figure 5.12: Data acquisition circuit in the test experiment for the range counter and the position detector. The data was taken with the cosmic ray trigger (L1 trigger). The GPIO distributes a signal for a trigger and HOLD to each VME-EASIROC board via the J0 bus on the VME crate. The common stop was distributed by another line directly to each VME-EASIROC board.

5.2.1 Photon Number in the PD Scintillator Slabs and its Hit Position Dependence

Figure 5.13 and 5.14 show the hit position dependence of the number of photons for the PD-Y and PD-Z segments, respectively. These figures were obtained by averaging the photon counts for those events in which cosmic rays penetrated all the layers of the range counter. By using the PD-Z hit information in Fig. 5.13 and the PD-Y hit information in Fig. 5.14, dependence of the photon count on the distance from the MPPC was investigated. There exists no hit position dependence in the number of photons in either PD-Y or PD-Z segments. Typically, we obtained about 20 photons in a segment of PD-Y and about 25 photons in PD-Z.

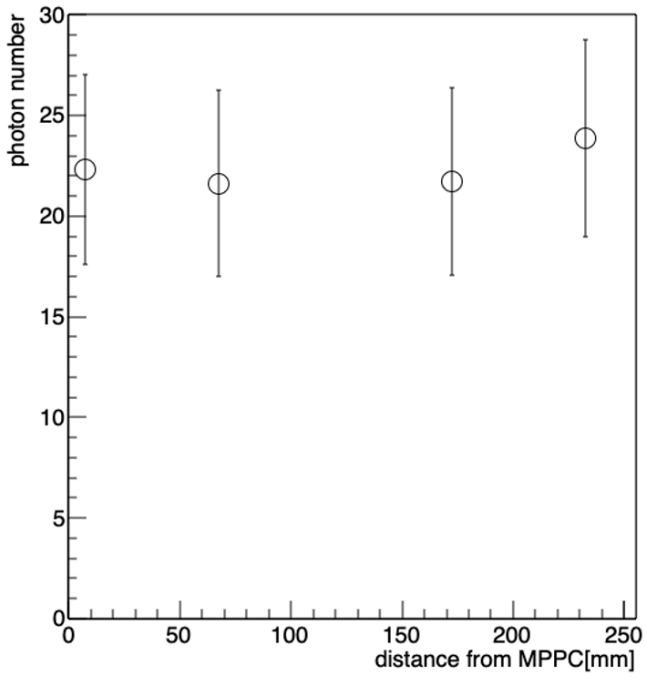

Figure 5.13: Hit position dependence in the photon number of the PD-Y obtained by averaging the photon counts for events where cosmic rays penetrated all the layers of the range counter. The position was selected by using the PD-Z hit information.

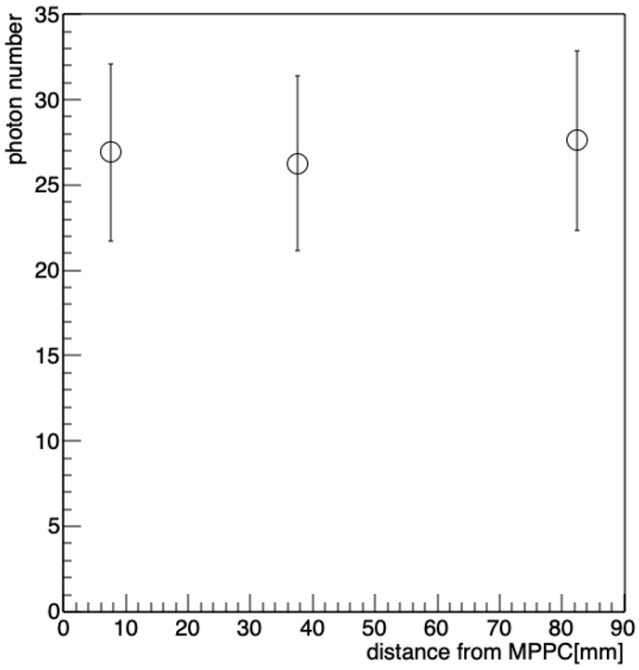

Figure 5.14: The hit position dependence in the photon number of the PD-Z obtained by averaging the photon counts for events where cosmic rays penetrated all the layers of the range counter. The position was selected by using the PD-Y hit information.

5.2.2 Number of Photons of the RC and its Hit Position Dependence

Using a setup shown in Figure 5.15, I examined the number of photons from a RC scintillator slab, detected by the two MPPCs from the two WLSFs located far from or close to cosmic-ray hit points A, B, and C on the first layer of the range counter. Figure 5.16 shows the hit position dependence of the number of photons in the first layer of the range counter. The hit positions were selected by the PD hit information to be close to one of the two fibers. The blue (red) data points represent the photon counts from the MPPC in contact with the fiber close to (far from) the hit positions. No dependence on the distance from the MPPC is found in both fibers far from and close to the hit positions. It is also found that the number of photons differs by about 10 photons between the fiber close to the hit positions and the fiber far from the hit positions. Typically, we obtained about 40 photons a fiber wherever MIPs hit. The number of photons for MIP was much more than about 15 photons of the prototype. This is because the surface of the scintillator was much clearer and I polished the side of the fiber not in contact with the MPPC. These changes contribute to the increase of the photons reflected in the scintillator

and the fibers without being emitted outward.

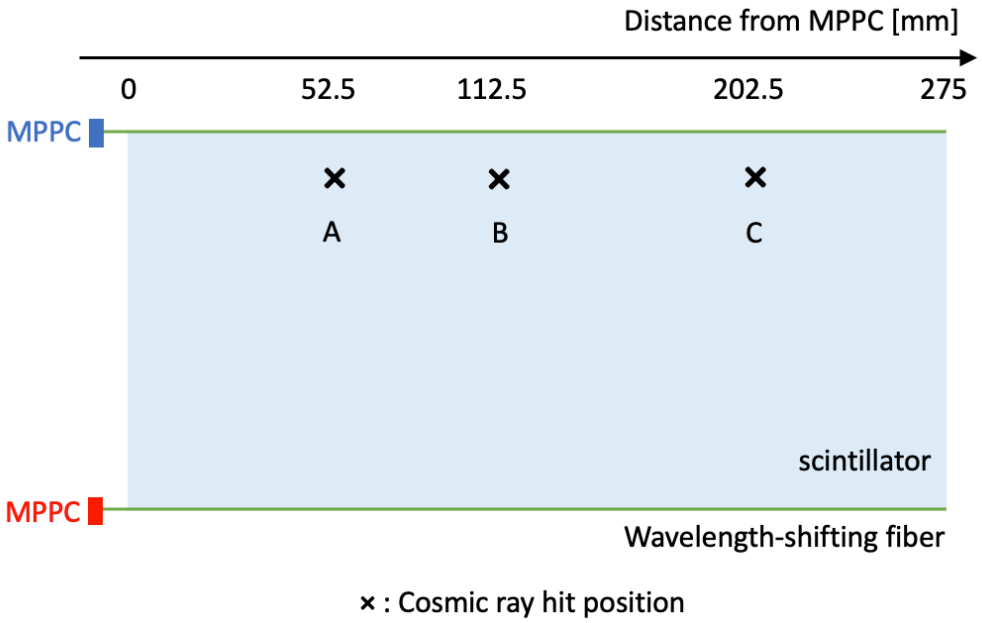

Figure 5.15: Hits positions (A, B and C) of cosmic rays on the first layer of the range counter used to study the number of photons. The number of photons detected by two MPPCs connected to the two fibers far from or close to the particle hit points was examined. The hit positions were selected by the PD hit information to be close to the fiber on one side.

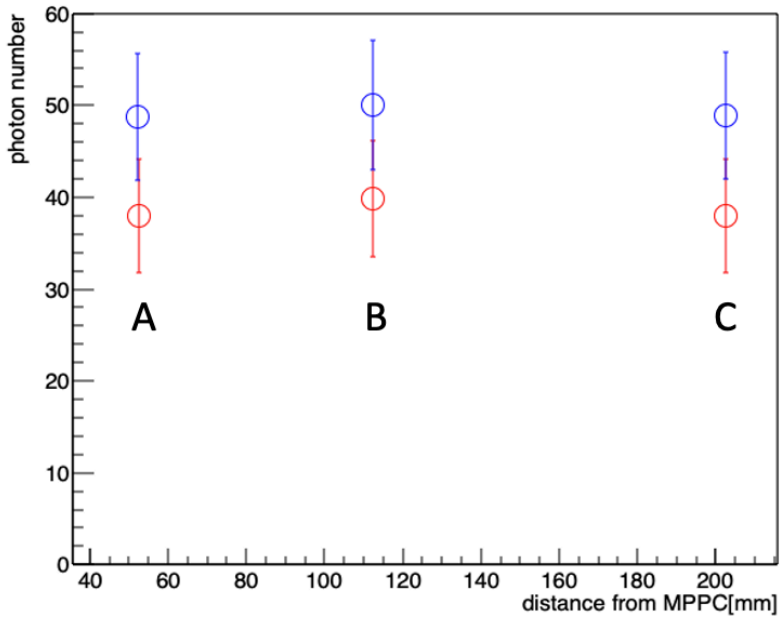

Figure 5.16: Hit position dependence of the number of photons in the first layer of the range counter. The hit positions were selected by the PD hit information to be close to one of the two fibers. The blue or red data points represent the photon counts at the MPPC in contact with the fibers close to or far from the hit positions. Points A, B, and C are shown in Fig. 5.15. No dependence on the distance from the MPPC exists in both fibers of far from and close to the hitting positions. It is found that the number of photons differs by about 10 photons between the fiber close to the hit positions and the fiber far from the hit positions.

5.2.3 Detection Efficiency of the Range Counter and the Position Detector

The efficiency of the range counter and the position detector are obtained as follows. As for the detection efficiency concerning a given layer of the range counter, it is defined as the probability of having a hit on the layer of interest when there is a hit on PD-Y and PD-Z and a hit on all the other layers of the range counter. In this case, a detection efficiency of 95% or higher was achieved for all layers. With respect to the detection efficiency of the position detectors Y and Z, the efficiency of a segment of PD-Y (Z) is defined as the probability that, when we have hits on all the layers of RC and a segment of the PD-Z (Y), we have a hit also on the segment of PD-Y (Z). The efficiency is also found to be higher than 95% for all the

segments of both PD-Y and PD-Z.

Chapter 6

Conclusion

We developed a range counter system for identification of nuclides for a gamma-ray spectroscopy experiment of secondary hypernuclei at the J-PARC K1.1 beam line (E63 experiment). We plan to measure the gamma-rays from the lightest hypernuclei of ${}^{3}_{\Lambda}\mathrm{H}$ and ${}^{4}_{\Lambda}\mathrm{H}$ by a Ge detector array (Hyperball-J) in the E63 experiment. The ${}^{4}_{\Lambda}\mathrm{H}$ and ${}^{3}_{\Lambda}\mathrm{H}$ cannot be directly produced from the (K^-, π^-) and (π^+, K^+) reactions, and therefore, the ${}^{7}\mathrm{Li}$ (K^-, π^-) reaction was adopted for the production of ${}^{4}_{\Lambda}\mathrm{H}$ and ${}^{3}_{\Lambda}\mathrm{H}$ as secondary hypernuclei. In order to identify from which hypernuclei the gamma-rays measured by Hyperball-J are emitted, we introduce a triple coincidence method between the reaction, gamma-ray, and weak decay. We measure the pion from hypernuclear weak decay with the range counter. The range counter system is required to separate two monochromatic pions from ${}^{4}_{\Lambda}\mathrm{H}$ and ${}^{3}_{\Lambda}\mathrm{H}$ (53 MeV and 40 MeV, respectively) in the range spectrum with a confidence level of 3σ.

I designed the range counter as multi-layered plastic scintillation counters. Based on previous studies by a Monte Carlo simulation and fabrication of a prototype layer, the range counter system has been determined to have 24 layers of a 6 mm-thick plastic counter, whose readout method employs wavelength-shifting fibers and SiPMs. In front of the range counter, plastic scintillator hodoscopes are installed as a position detector (PD-Y and PD-Z) for measuring the incident angle of the pions.

I fabricated a prototype range counter with a thickness of one-third of the whole detector for the E63 experiment and conducted a test experiment for the prototype at J-PARC using beam pions and scattered protons. The time of flight of the particles was measured using two plastic hodoscopes located just before the prototype. I selected slow pion events with the information of the time of flight and, as a result, I found that about 300 pions stopped in the prototype. I also found that, from the distribution of the measured range and the kinetic energy from the time of flight, the prototype can separate pions from ${}^{4}_{\Lambda}\mathrm{H}$ and ${}^{3}_{\Lambda}\mathrm{H}$ sufficiently well.

Then, I fabricated a whole set of the range counter of 24 layers and the position detector, and then conducted a simple experiment to test them with cosmic rays. Typically, I obtained about 20 photons in a segment of PD-Y and about 25 photons in PD-Z for a minimum ionizing particle (MIP). In addition, we typically obtained about 40 photons for a MIP by one SiPM in a layer of the range counter. The number of photons satisfies our purpose. The efficiency of the range counter and the position detector achieved more than 95% for all the layers of the range counter and all the segments of the position detector.

Based on the results of the experiment with the prototype and of the evaluation of the whole set of the range counter and the position detector, it is concluded that the range counter system developed in this study can identify the weak decay pions in the E63 experiment.

Bibliography

[1] H. Hotchi *et al.*, Phys. Rev. C **64**, 044302 (2001)

[2] K. Tanida *et al.*, Phys. Rev. Lett. **86**, 1982 (2001)

[3] K. Miwa *et al.*, Phys. Rev. Lett. **128**, 072501 (2022)

[4] T. Nanamura *et al.*, Prog. Theor. Exp. Phys., **2022**, 093D01 (2022)

[5] K. Miwa *et al.*, the proposal of the E86 experiment, *Measurement of the differential cross section and spin observables of the* Λp *scattering with a polarized* Λ *beam*

[6] T. O. Yamamoto *et al.*, Phys. Rev. Lett. **115**, 222501 (2015)

[7] R. A. Brandenburg, G. S. Chulick, Y. E. Kim, D. J. Klepacki, R. Machleidt, A. Picklesimer, and R. M. Thaler, Phys. Rev. C **37**, 781 (1988)

[8] J. L. Friar, B. F. Gibson, and G. L. Payne, Phys. Rev. C **35**, 1502 (1987)

[9] Y. Wu, S. Ishikawa, and T. Sasakawa, Phys. Rev. Lett. **64**, 1875 (1990)

[10] R. A. Brandenburg, S. A. Coon, and P. U. Sauer, Nucl. Phys. A **294**, 305 (1978)

[11] J. L. Friar, B. F. Gibson, and G. L. Payne, Phys. Rev. C **42**, 1211 (1990)

[12] G.A. Miller, A.K. Opper, and E.J. Stephenson, Ann. Rev. Nucl. Part. Sci. **56**, 253 (2006)

[13] R. Machleidt and H. Müther, Phys. Rev. C **63**, 034005 (2001)

[14] A. Esser, S. Nagao *et al.*, Phys. Rev. Lett. **114**, 232501 (2015)

[15] F. Schulz *et al.*, Nucl. Phys. A **954**, 149 (2016)

[16] M. Jurič *et al.*, Nucl. Phys. B **52**, 1 (1973)

[17] T. Shao for the STAR Collaboration, EPJ Web Conf. **271**, 08010 (2022)

[18] M. Bedjidian *et al.*, Phys. Lett. B **83**, 252 (1979)

[19] M. Bedjidian *et al.*, Phys. Lett. B **62**, 467 (1976)

[20] A. Kawachi, Docter thesis, University of Tokyo, 1997

[21] A. R. Bodmer and Q. N. Usmani, Phys. Rev. C **31**, 1400 (1985)

[22] R. H. Dalitz, F. Von Hippel, Phys. Lett. **10**, 153 (1964)

[23] S. A. Coon, H. K. Han, J. Carlson, B. F. Gibson, arXiv:nucl-th/9903034

[24] A. Nogga, H. Kamada, and Walter Glöckle, Phys. Rev. Lett. **88**, (2002)

[25] D. Gazda and A. Gal, Phys. Rev. Lett., **116**, 12, (2016)

[26] C. Rappold, *et al.* (HypHI Collaboration), Nucl. Phys. A **913**, 170 (2013)

[27] H. Garcilazo and A. Valcarce, Phys. Rev. C **89**, 057001 (2014)

[28] E. Hiyama, S. Ohnishi, B. F. Gibson, and Th. A. Rijken, Phys. Rev. C **89**, 061302(R) (2014)

[29] A. Gal, H. Garcilazo, Phys. Lett. B **736**, 93 (2014)

[30] K.N. Suzuki, T. Gogami *et al.*, Prog. Theor. Phys. Suppl., **2022**, 1 (2022)

[31] K. Itabashi, Doctor thesis, Study of Lambda quasi-free production in the ^{3}H(e, e$'$K$^+$)X reaction, Tohoku University (2022)

[32] R. J. Prem, P. H. Steinberg, Phys. Rev. **136** (1964)

[33] G. Keyes *et al.*, Phys. Rev. Lett. **20**, 819 (1968)

[34] R. E. Phillips, J. Schneps, Phys. Rev. **180**, 1307 (1969)

[35] G. Keyes *et al.*, Nucl. Phys. B **67**, 269 (1973)

[36] B. I. Abelev, *et al.* (STAR Collaboration), Science **328**, 58 (2010)

[37] C. Rappold, *et al.* (HypHI Collaboration), Phys. Lett. B **728**, 20 (2014)

[38] J. Adam, *et al.* (ALICE Collaboration), Phys. Lett. B **754**, 360 (2016)

[39] L. Adamczyk, *et al.* (STAR Collaboration), Phys. Rev. C **97**, 054909 (2018)

[40] J. Adam, *et al.* (STAR Collaboration), Nature Physics **16**, 409 (2020)

[41] M. May *et al.*, Phys. Rev. Lett. **51**, 2085 (1983)

[42] K. Agari *et al.*, Prog. Theor. Exp. Phys. **2012**, 02B009 (2012)

[43] T.O. Yamamoto, Doctoral thesis, Charge symmetry breaking in ΛN interaction studied via the γ-ray spectroscopy of ${}^{4}_{\Lambda}$He, Tohoku Universtiy (2015)

[44] Y. Igarashi *et al.*, IEEE Trans. Nucl. Sci. **57**, 618 (2010)

[45] H. Tamura *et al.*, the proposal of the J-PARC E63 experiment, *Gamma-Ray Spectroscopy of Light* Λ *Hypernuclei* II

[46] Y. Ishikawa, master's thesis, Detectors to identify nuclides for a hypernuclear γ-ray spectroscopy experiment, Tohoku University (2017)

[47] Hamamatsu, MPPC technical note. https://www.hamamatsu.com/content/dam/hamamatsu-photonics/sites/documents/99_SALES_LIBRARY/ssd/s13360_series_kapd1052j.pdf

[48] S. Callier, C.D. Taille, G.M. Chassard, L. Raux, Physics Procedia **37**, 1569 (2012)

[49] T. Shiozaki, master's thesis, Development of a MPPC multi-channel readout system for the Σp scattering experiment, Tohoku University (2013)

[50] Manual of Plastic Scintillation Fibers - Kuraray. http://kurarayps f.jp/pdf/all.pdf

[51] A. T. M. Aerts *et al.*, Phys. Rev. D **28**, 450 (1983)

[52] R. M. Sternheimer, Phys. Rev. **117**, 485 (1960)

[53] J. F. Ziegler, J. Biersack, U. Littmark, "The Stopping and Range of Ions in Matter", Pergamon Press (1985)

[54] J. F. Ziegler, M. D. Ziegler, J. P. Biersack, Nucl. Instrum. Methods, B **268**, 1818 (2010)

[55] T. Pöschl *et al.*, Nucl. Instrum. Methods, A **988**, 164865 (2021)

[56] Y. B. Gurov, V. S. Karpukhin, S. V. Lapushkin, *et al.*, Phys. Atom. Nuclei **82**, 351 (2019)

[57] D. Gotta *et al.*, Phys. Lett. B **112**, 129 (1982)

[58] V. S. Buttsev *et al.*, Sov. J. Part. Nucl. **11**, 358 (1980)

[59] Y. B. Gurov, L. Y. Lapushkin, S. V. Lapushkin, *et al.*, Bull. Russ. Acad. Sci. Phys. **80**, 215 (2016)

[60] C. Cernigoi *et al.*, Nucl. Phys. A **411**, 382 (1983)

[61] R. Hartmann *et al.*, Nucl. Phys. A **308**, 345 (1978)

[62] U. Klein *et al.*, Nucl. Phys., A **329**, 339 (1979)

[63] B. Bassalleck *et al.*, Nucl. Phys., A **319**, 397 (1979)

[64] R. Madey *et al.*, Phys. Rev., C **25**, 3050 (1982)

[65] H. L. Anderson *et al.*, Phys. Rev. **133**, B392 (1964)

[66] P. M. Hattersley *et al.*, Nucl. Phys. **67**, 309 (1965)

[67] H. Machner, Nucl. Phys., A **395**, 457 (1983)

[68] A. Bratenahl, J. M. Peterson, and J. P. Stoering, Phys. Rev. **110**, 927 (1958)

[69] D. Horváth *et al.*, Phys. Rev. A **41**, 5834 (1990)

謝辞

本論文・研究は本当に多くの方々のお力添えのもと完成させることができました。心から感謝いたします。誠にありがとうございます。

指導教員の田村裕和教授には何から何まで本当にお世話になりました。深く感謝しています。

学部 2 年の特殊相対論の授業を受けたときから、田村教授の楽しそうに物理を教えてくださる姿が印象的で、大学院の授業でも、研究室のゼミや研究会などにおいても田村教授の話を聞くと自ずとわくわくとしてきて、それが研究を進める活力となっていました。本研究テーマも、田村教授のお話に惹き込まれ、気づくと私が進めていました。私がハイパー核や原子核、ハドロンの研究の面白さを知り、さらにもっとこの分野を極めるために研究を続けたいと思うようになったのはひとえに田村教授のおかげです。また、研究室に配属されてからの日々が非常に充実していたのは、田村教授が私に多くの経験や研究、勉強の機会を与えてくださり、さらにご自身のお仕事が数え切れないほどあるにも関わらず、私が居室に伺うと快く熱心に長時間にわたって議論やお話してくださったおかげだと思います。忙しい日々でしたがその忙しさを遥かに上回るほど楽しく、何にも変え難い充実した修士課程での研究生活となりました。まだまだ足りていないところばかりの私ですが、田村教授を目標にしてより一層精進してまいります。博士課程でも引き続きご指導、ご鞭撻の程よろしくお願いいたします。

三輪浩司准教授にも大変お世話になりました。実験に行き詰まり相談しに行くといつもいとも簡単に原因を突き止め、解決してくださるので毎回感動していました。また、私の研究に対して、いつも冷静に重要な指摘をしてくださるのが非常にありがたかったです。感謝しております。また、学部 3 年のときの三輪准教授の原子核物理の授業を聞いたことがきっかけで、素粒子と原子核の物理を深く勉強、研究してみたいと思うようになりました。これからもご指導、よろしくお願いいたします。

早川修平助教にも丁寧に指導していただきました。早川助教の説明や資料は非常にまとまっていて分かりやすく、私の理解をいつも深めてくれました。ありがとうございます。早川助教のいつも明るく場を和ますと同時に、常に冷静かつ的確な判断や発言をされるところもすごいと思っています。早川氏のように活躍できるように私も頑張ります。これからもご指導、よろしくお願いいたします。

ELS グループの、東京大学の中村哲教授、永尾翔助教、東北大学の金田雅司助教にもこれまでたくさんご指導いただき、お世話になりました。隣のグループから、新しい視点で鋭いご指摘を頂けて大変助かりました。ありがとうございます。

東北大学高度教養教育 · 学生支援機構の小池武志准教授にもお世話になりました。理数応援プロジェクトでカリフォルニアへ留学中に、どの研究室に入ろうか決めかねていた私に色々お話しをしてくださりました。留学中に UC Berkeley に車で連れていってくださったのは良い思い出です。留学後、研究室見学や田村教授との面談を手配してくださり、また、理研仁科センターの国際スクールや KEK のサマーチャレンジを紹介してくださったことが、この研究室で研究を始めるきっかけとなりました。ありがとうございました。また居室に遊びにいきます。

技術職員の梅津裕生氏なくしては、飛程検出器と位置検出器の設計・製作は完遂できていません。たくさんの助言とご協力をありがとうございました。研究室秘書の高橋あゆみ氏と佐々木幸恵氏にいつも陰ながら研究活動を支えていただいたことで、研究に専念できました。ありがとうございました。

本研究は東北大学宇宙創成国際共同大学院プログラム (GP-PU) に参加して行われたものであり、GP-PU からの経済的援助なくしてはこれまでの研究生活は成り立っていません。感謝しております。GP-PU 秘書の三和レーン比呂子氏にも大変お世話になりました。事務室に伺った際には、自身の海外経験をもとに親切丁寧に色々と教えてくださったり、美味しい差し入れをくださったりと、いつも気にかけてくださりありがとうございます。

KEK の高橋俊行教授、鵜養美冬研究機構講師、本多良太郎准教授や、JAEA の谷田聖研究主幹、山本剛史研究員、市川裕大研究員、藤田真奈美研究員、Shin Hyung Kim 研究員にもお世話になりました。鵜養講師や山本研

究員には、日々の研究における議論や J-PARC での実験準備にて大変お世話になりました。豊富な経験と知識に基づく助言や協力が非常に心強かったです。また、東海にて楽しく健康的に出張生活を送ることできたのも、お二人が研究以外の面でも面倒を見てくださったおかげです。ご多忙の中いつも気にかけてくださり、ありがとうございます。本多准教授には基板作成やデータ収集についてたくさん指導していただきました。また、いつの日だったか東海ドミトリにて夜遅くまでお話しした時の、物理への熱い想いを語る本多氏の姿を今でも時折思い出し、ひとり感化されております。ありがとうございます。藤田研究員には、試作機のテスト実験の準備やデータ解析にて修士課程に入ったばかりで何もわからない私に懇切丁寧に指導してくださいました。藤田氏なくしてはテスト実験を完遂できていません。その後も、度々議論に付き合ってくださりたくさん助言をくださいました。ありがとうございました。市川研究員も修士課程にて飛程検出器を開発されていたこともあり、これまでたくさん助言と励ましをいただきました。ありがとうございます。市川氏のようにいつまでも物理学への情熱を持って研究していきたいと思っています。

E42 実験グループの、spokesperson である高麗大の Jung Keun Ahn 教授を始め、S.H. Kim 研究員、市川研究員、早川助教には、E42 実験の準備やビームタイム等、怒涛の忙しさの中にも関わらず、本研究に快くご協力いただきありがとうございました。あの時に低運動量パイ中間子ビームのデータを取ることができていなかったら本論文の 4 章を書くことはできていませんでした。皆様のおかげで非常に有意義な議論 · 考察をすることができました。また、実験の楽しさを知ることができたのもこの実験期間でした。感謝しております。

京都大学の永江知文教授、後神利志助教、原田健志氏、江端健悟氏、高橋秀治氏や東京工業大学の藤岡宏之准教授、内田誠助教、根岸亮輔氏、小堀匠氏には実験準備やミーティングにてお世話になりました。ありがとうございました。特に原田氏には大変お世話になりました。原田氏の何事も丁寧に一から自分で原理や理由を理解していく姿勢に非常に刺激を受けていました。私はまだその姿勢を徹底できていないので見習っていきます。また、私の質問に対していつも分かりやすく答えてくださったり、一緒に考えてくださったりと、本当にありがとうございます。引き続き実験遂行のために頑張っていきましょう。

研究室の先輩である、石川勇二氏、Tatyana Rogers 氏、秋山タケル氏、奥山和樹氏、梶川俊介氏、坂尾珠和氏、鎌田健人氏、北岡智真氏、中村雄紀氏、水野柾哉氏にも大変お世話になりました。石川氏は、私が研究室に入った頃から本研究について一緒に議論をしてくださり大変助かりました。また、D 論執筆の忙しいときにも関わらず私の相談に乗ってくださったり、深夜に車を出して一緒に夜食を買いに行ってくださったりとお世話になりました。東海出張中に修論執筆を頑張れたのは石川氏のおかげです。ありがとうございます。Rogers 氏には、私が研究室に入って間もない時に連日作業を手伝ってもらい、実験や飛程検出器について教えていただのを今でもよく覚えています。I appreciate very much for your advise and kindness. 梶川氏には廊下やセミナー室ですれ違ったときに、いつも研究に関する話や他愛もない話に付き合っていただきました。お話することで気分を切り替えることができたので感謝しています。坂尾氏に仙台や出張先でお会いした際には、いつも色々と相談にのっていただき、その度に激励の言葉をくださり感謝しています。坂尾氏のいつも淡々と研究に打ち込む姿勢を見習って頑張ります。水野氏は、勉強会や飲み会などの急な誘いにいつも快く乗ってくださり感謝しています。これからもよろしくお願いします。鎌田氏には特にお世話になりました。東海出張中は、鎌田氏のおかげで不自由なく生活することができました。チェコとドイツへの出張の際に出張先での研究と生活が充実していたのは鎌田氏のおかげです。また、いつも研究に関する話や他愛もない話に長時間にわたって付き合ってくださり、非常に楽しかったです。ありがとうございます。これからも実験遂行のために共に頑張っていきましょう。

同輩の木野量子氏、橘昂我氏、永野慎太郎氏、森野泰斗氏にも大変お世話になりました。何かと同期で集まる機会が多く、恵まれていたと思います。特に木野氏には、本研究の飛程検出器の製作の際にはご多忙の中、長時間にわたり製作を手伝っていただきました。日々の研究生活においても関わることが多く、熱心に研究に打ち込む姿勢に良い刺激をもらっていました。感謝しています。出張中に鎌田氏と 3 人でヨーロッパ観光をしたのも良い思い出です。博士課程に進学しても共に切磋琢磨して研究していきましょう。

後輩の石毛達大氏、大橋和真氏、成済秀氏、宮田楓氏、渡辺大護氏、今本亮氏、河野理夏子氏、齋藤隆太氏にもお世話になりました。真面目に研究に取り組む後輩たちから教えてもらうことがたくさんありました。そして、みなさまのおかげで楽しい研究生活となりました。ありがとうございます。これからも頑張りましょう。成氏には検出器制作を手伝ってもらい、日頃、居室でたくさん議論に付き合ってもらいました。感謝しています。

この他にもここには書ききれないほどたくさんの知人、友人、親戚の皆様のご理解とご支援のもと充実した研究生活を送ることができました。ありがとうございます。

最後に、いつも私を一番に理解し、応援してくれる家族に深く感謝の意を表したいと思います。小さい時か

らずっと私のことを、時に優しく時に厳しく、見守り、導いてくれたからこそ今の私があります。今でものびのびと自由にやる私の意思を尊重し、いつも鼓舞激励してくれて、本当にありがとうございます。

ありがたいことに、人との縁に恵まれていた修士課程でした。お世話になったみなさまへの感謝の気持ちを忘れずに、一人前の研究者に早くなれるよう、博士課程に進んでも弛むことなくより一層精進努力していく所存です。

2023 年 2 月
大浦 文也